EDIBLE OPTICAL MICROCAVITIES AND MICROLASERS

Abdur Rehman Anwar

Doctoral Dissertation
Jožef Stefan International Postgraduate School
Ljubljana, Slovenia

Supervisor: Assoc. Prof. Dr. Matjaž Humar, Jožef Stefan Institute, Faculty of Mathematics and Physics, University of Ljubljana, and CENN Nanocenter, Ljubljana, Slovenia

Evaluation Board:
Assoc. Prof. Dr. Miha Škarabot, Chair, Jožef Stefan Institute, Ljubljana, Slovenia
Assoc. Prof. Dr. Anton Gradišek, Member, Jožef Stefan Institute, Ljubljana, Slovenia
Assoc. Prof. Dr. Yu-Cheng Chen, Member, School of Electrical & Electronic Engineering, Nanyang Technological University, Singapore

MEDNARODNA PODIPLOMSKA ŠOLA JOŽEFA STEFANA
JOŽEF STEFAN INTERNATIONAL POSTGRADUATE SCHOOL



Abdur Rehman Anwar

EDIBLE OPTICAL MICROCAVITIES AND MICROLASERS

Doctoral Dissertation

UŽITNE OPTIČNE MIKROVOTLINE IN MIKROLASERJI

Doktorska disertacija

Supervisor: Assoc. Prof. Dr. Matjaž Humar

Ljubljana, Slovenia, July 2026

Acknowledgments

First and foremost, I would like to express my deepest gratitude to my supervisor, Dr. Matjaž Humar, for his continuous guidance and support throughout my PhD journey. His insightful ideas, stimulating discussions, and constructive criticism have been invaluable to the successful completion of this work.

I am sincerely grateful to all my colleagues in the Humar Lab for creating a supportive and collaborative research environment. In particular, I would like to thank Dr. Maruša Mur for guiding me through the initial experimental work and introducing me to edible gain materials. My gratitude also goes to Ana Krišelj for her assistance in preparing solutions and supporting matrices, which were essential for designing edible microcavities and conducting sensing experiments.

I was fortunate to share an office with Dr. Aljaž Kačič, whose helpful discussions and assistance—especially with administrative matters and visa-related procedures—made my journey significantly smoother. I also thank Dr. Slavko Kralj (Jožef Stefan Institute, Slovenia) for preparing samples and for valuable discussions regarding microspheres, and Rok Štanc (Institute of Biophysics, University of Ljubljana, Slovenia) for his guidance during the initial microfluidics experiments. I am grateful to Dr. Aleksander Matavž (Jožef Stefan Institute, Slovenia) for ellipsometry measurements and to Assoc. Prof. Miha Škarabot (Jožef Stefan Institute, Slovenia) for AFM characterization of the samples.

My sincere appreciation extends to the Bikiaris Lab at Aristotle University of Thessaloniki (AUTH), Greece, for hosting me and supporting the identification and preparation of samples for sensing experiments. I am deeply grateful to Prof. Graham A. Turnbull at the University of St Andrews, Scotland, for hosting me in his laboratory and for his mentorship in developing distributed feedback lasers, as well as training in advanced characterization techniques and cleanroom work.

I gratefully acknowledge the financial support provided by the European Union's Horizon 2020 research and innovation program under the Marie Skłodowska-Curie grant agreement No. 956265, and by the ERC Proof of Concept (EdibleLasers), PR-13174.

This journey was not without personal challenges. During the second year of my PhD, I experienced the sudden loss of my elder brother. Completing this work would not have been possible without the strength and encouragement I received from my loved ones.

Finally, I would like to express my heartfelt gratitude to my parents, Muhammad Anwar and Jamila Kousar, for their unconditional love, prayers, and lifelong support. My deepest appreciation goes to my wife, Dr. Laiba Suhail, whose unwavering encouragement and patience sustained me throughout this journey. I also extend my love to my extended family, whose affection and support have always meant a great deal to me. At the same time, I am grateful to welcome our baby, Rosheen Abdur Rehman, who became a beautiful part of this PhD journey.

Abstract

Biolasers based on biological and biocompatible materials have emerged as powerful tools for biomedical applications such as cell barcoding, tracking, and biosensing. Despite these advances, the realization of lasers fabricated entirely from edible substances has remained largely unexplored. Developing such microlasers could enable optical tagging and sensing directly within consumable products, thereby overcoming the limitations of conventional barcodes and sensors, which are restricted to external packaging and vulnerable to removal or tampering.

In this thesis, edible photonic microcavities are investigated as integrated platforms for barcoding and sensing, operating above and below the lasing threshold. A systematic investigation of consumable materials identifies naturally derived fluorophores, including chlorophyll-A and vitamin B_2, as a suitable gain medium for the realization of edible lasers. These gain media are incorporated into edible resonators to design fully edible lasers in various configurations. Edible microlasers based on whispering-gallery-mode (WGM) and Fabry-Pérot (FP) cavity configurations are demonstrated. WGM microlasers are demonstrated using doped liquid droplets of controlled sizes produced via microfluidic chips. In addition, WGM microcavities operating below the lasing threshold are produced using solid monodisperse silica microspheres coated with chlorophyll and silica via a modified Stöber method. FP cavities are formed by confining the gain media between the mirrors based on edible silver leaf. These microcavities exhibit ultra-narrow emission linewidths, enabling high multiplexing capacity and sensitivity to surrounding changes such as refractive index. When embedded directly into food products, they function as optical barcodes capable of encoding tens of bits of data, such as manufacturer information and expiration dates, while inherent fabrication variations provide physical unclonable functions (PUFs) for anti-counterfeiting. The strong environmental responsiveness of the WGM modes enables sensing of key parameters relevant to food quality and safety, including sugar concentration, pH, bacterial growth, and exposure to high temperatures.

However, practical limitations of liquid droplet-based microlasers operating above the lasing threshold–such as the requirement for pulsed excitation, liquid droplet instability, and limited fabrication scalability–make solid microcavities operating under continuous wave (CW) excitation more suitable from a practical perspective. These solid microcavities offer improved mechanical stability, as well as low-cost and scalable fabrication. Importantly, the microlasers and microcavities developed in this study are entirely safe for consumption, do not alter the appearance or taste of food, and are environmentally friendly.

In summary, this work establishes a comprehensive framework for fully edible photonic barcodes and sensors. The developed concepts extend beyond food and apply to pharmaceuticals, cosmetics, agriculture, and other high-value consumable products, enabling new strategies for secure authentication, traceability, and freshness monitoring directly within the product itself.

Povzetek

Biolaserji, ki temeljijo na bioloških in biokompatibilnih materialih, so se uveljavili kot pomembna orodja v biomedicinskih aplikacijah, kot so unikatno celično označevanje, sledenje in biosenzorika. Kljub tem napredkom pa možnost izdelave laserjev izključno iz užitnih snovi ostaja neraziskana. Razvoj tovrstnih mikrolaserjev bi omogočil optično označevanje in zaznavanje neposredno znotraj potrošniških izdelkov, s čimer bi odpravili probleme običajnih črtnih kod in senzorjev, ki so omejeni na zunanji zaščitni ovoj izdelka ter posledično ranljivi za njihovo odstranitev, poseganje ali spreminjanje.

V tej disertaciji smo raziskovali resonatorje iz užitnih snovi, ki delujejo nad in pod pragom laserskega delovanja, kot integrirano platformo za označevanje in zaznavanje. Sistematična študija materialov je pokazala, da so naravno pridobljeni fluorofori, vključno s klorofilom-A in vitaminom B_2, primerni kot ojačevalni medij za realizacijo užitnih laserjev. Ti ojačevalni mediji so vključeni v resonatorje iz užitnih snovi za zasnovo popolnoma užitnih laserjev v različnih konfiguracijah. Predstavljeni so užitni mikrolaserji, ki temeljijo na t.i. "whispering-gallery-mode" (WGM) in Fabry-Pérot (FP) resonatorskih konfiguracijah. WGM mikrolaserji so bili izdelani z uporabo dopiranih tekočih kapljic nadzorovanih velikosti, proizvedenih z mikrofluidnimi čipi. Po drugi strani so bili WGM resonatorji, ki delujejo pod pragom laserskega delovanja, izdelani z uporabo trdnih monodisperznih silicijevih mikrosfer, prevlečenih s klorofilom in silicijevim dioksidom skladno s Stöberjevo metodo. FP resonatorji so bili oblikovani z vstavitvijo ojačevalnega medija med zrcali iz užitne srebrne folije. Ti mikroresonatorji izkazujejo izjemno ozke vrhove v izsevanem spektru, kar omogoča visoko zmogljivost združevanja več signalov in občutljivost na spremembe v okolici. Ko so vgrajeni neposredno v živilske izdelke, delujejo kot optične črtne kode, sposobne shranjevanja več deset bitov podatkov, kot so informacije o proizvajalcu in roku uporabe, medtem ko inherentne variacije v izdelavi zagotavljajo fizikalno neponovljive funkcije (PUF – physical unclonable functions) za preprečevanje ponarejanja. Močna odzivnost WGM načinov na spremembe v okolju omogoča zaznavanje ključnih parametrov, pomembnih za kakovost in varnost hrane, vključno s koncentracijo sladkorja, pH vrednostjo, rastjo bakterij in izpostavljenostjo visokim temperaturam.

Vendar pa praktične omejitve mikrolaserjev iz tekočih kapljic, ki delujejo nad pragom laserskega delovanja – kot so potreba po pulznem vzbujanju, nestabilnost tekočih kapljic in omejena prilagodljivost izdelave – kažejo, da so trdni mikroresonatorji, ki delujejo v načinu zveznega vzbujanja, primernejši z vidika praktične uporabe. Ti trdni mikroresonatorji zagotavljajo izboljšano mehansko stabilnost ter nizkocenovno in razširljivo izdelavo. Pomembno je, da so mikrolaserji in mikroresonatorji, razviti v tej študiji, popolnoma varni za uživanje, ne spreminjajo videza ali okusa hrane ter so okolju prijazni. Če povzamemo, to delo vzpostavlja celovito zasnovo za popolnoma užitno optično označevanje in zaznavanje. Razviti koncepti presegajo področje hrane in tržnih izdelkov in se lahko uporabljajo tudi v farmacevtski industriji, kozmetiki, kmetijstvu in drugih potrošnih izdelkih z visoko vrednostjo, kar omogoča nove strategije za varno avtentikacijo, sledljivost in spremljanje svežine neposredno znotraj izdelka samega.

Contents

List of Figures **xv**

List of Tables **xxiii**

Abbreviations **xxv**

1 Introduction **1**
1.1 Background and Motivation . . . 1
1.2 Optical Microbarcodes . . . 2
1.2.1 Graphical barcodes . . . 3
1.2.2 Spectral barcodes . . . 3
1.2.3 Microcavity- and microlaser-based barcodes . . . 4
1.3 Biolasers . . . 4
1.4 State of the Art Applications of Microcavity-Based Barcodes . . . 6
1.4.1 Cell tagging and tracking . . . 6
1.4.1.1 In vitro demonstrations . . . 7
1.4.1.2 In tissues and in vivo . . . 9
1.4.2 Product labeling and anti-counterfeiting . . . 9
1.5 Recent Advances in Edible or Food-Compatible Tags . . . 12
1.5.1 Edible barcodes and tags (non-microcavity-based) . . . 13
1.5.2 Previous work on edible or partially edible lasers . . . 14
1.6 Goal of the Thesis . . . 16

2 Theoretical Background **19**
2.1 Optical Microcavities . . . 19
2.1.1 Quality factor . . . 20
2.1.2 Purcell effect . . . 21
2.2 Whispering-Gallery Modes . . . 21
2.2.1 Geometric approximation . . . 22
2.2.2 Exact electromagnetic solution . . . 22
2.3 Whispering-Gallery Mode Sensing Mechanisms . . . 23
2.3.1 Mode shifting . . . 24
2.4 Fabry-Pérot Cavity . . . 24
2.5 Excitation of Optical Cavities . . . 25
2.6 Properties and Characteristics of Lasers . . . 26
2.6.1 Light-matter interaction . . . 26
2.6.2 Population inversion and optical gain . . . 27
2.7 Principles of Optical Barcoding Based on Microcavities . . . 28
2.7.1 Encoding using single- and multi-mode emission . . . 28
2.7.2 Random versus predefined WGM barcodes . . . 30
2.7.3 Multiplexing . . . 30

2.8 Multimodal Application of Microcavities: Barcoding and Sensing 31

3 Materials and Methods 33
3.1 Components of Edible Lasers 33
3.1.1 Edible gain media 33
3.1.1.1 Chlorophyll extraction from spinach leaves 34
3.1.2 Edible optical cavity 35
3.2 Fabrication of Microcavities and Their Applications 36
3.2.1 Whispering-gallery modes (WGMs) 36
3.2.1.1 Oil-in-water emulsion 36
3.2.1.2 Spraying on hydrophobic/superhydrophobic surfaces 36
3.2.1.3 Microfluidics 37
3.2.1.4 Mass scale production of WGM microcavities 38
3.2.2 WGMs for sensing 39
3.2.2.1 pH sensing based on WGM microcavities 39
3.2.2.2 Sugar sensing based on WGM microcavities 39
3.2.3 Edible FP cavity 40
3.2.3.1 Edible sealant 40
3.2.4 FP cavity for sensing 40
3.2.4.1 FP cavity as a pH sensor 40
3.2.4.2 FP cavity as a microorganism sensor 41
3.3 Optical Setup 41
3.3.1 Setup for barcode readout 42
3.3.2 Line scaning 42
3.4 Analysis of Emission Signal 42
3.4.1 WGMs 42
3.4.2 FP cavities 43

4 Experimental Results and Discussion 45
4.1 Whispering-Gallery Modes Microcavities 45
4.1.1 Chlorophyll-doped sunflower oil droplets dispersed in water 45
4.1.2 Extracted chlorophyll-doped sunflower oil droplets in water 46
4.1.3 Extracted chlorophyll-doped sunflower oil droplets inside agar matrix 46
4.1.4 Riboflavin-doped water droplets 47
4.1.5 Edible bubble laser 49
4.1.6 Edible WGM solid microspheres 49
4.2 Demonstration of Edible Microcavities-Based Barcodes 50
4.2.1 Edible microlasers barcodes produced via microfluidics 51
4.2.1.1 Demonstration of edible barcodes in liquid consumables . . 52
4.2.2 Edible barcodes based on WGM solid microspheres 53
4.2.2.1 Barcodes for high-refractive-index media 55
4.2.2.2 Barcodes for solid consumables 55
4.3 Edible Physical Unclonable Functions (PUFs) 56
4.3.1 Edible PUFs based on droplet microlasers 56
4.3.2 Demonstration of edible PUFs based on solid microspheres 57
4.4 Edible WGM Sensors 59
4.4.1 Demonstration of sugar sensing based on WGM microlaser 59
4.4.2 Temperature indicator 59
4.4.3 Demonstration of edible sensors based on WGM microspheres 61
4.4.3.1 Sugar sensing 61
4.4.3.2 pH sensing 61

4.5 Edible FP Cavity 63
4.6 Demonstration of Edible Sensors Based on FP Cavity 64
4.6.1 pH sensing 64
4.6.2 Detection of microorganism growth 65

5 Conclusions **67**

References **69**

Bibliography **79**

Biography **81**

List of Figures

Figure 1.1: Schematic overview of different types of microbarcodes and their encoding mechanisms. Microbarcodes include non-optical identifiers (RFID, isotopes, and DNA) as well as optical encoding schemes based on graphical patterns, spectral responses (fluorescence, Raman scattering, reflection, and microcavity resonances), and additional physical parameters such as polarization, lifetime, or angular momentum. 2

Figure 1.2: a) Illustration of the single-cell laser where a live eGFP-expressing 293ETN cell is positioned inside an optical resonator composed of two highly reflective distributed Bragg reflectors. b) Schematic illustration of lasing emission from live E. coli bacterial cells expressing the Venus fluorescent protein. The bacteria are suspended and freely mobile within glycerol–water microdroplets on a superhydrophobic surface. c) Schematic illustration of the oil injection into the cytoplasm of a cell, alongside a confocal fluorescence image showing a polyphenyl ether droplet doped with Nile red dye (red) and the cell nucleus (blue). d) Schematic illustration of a mature subcutaneous adipocyte containing a lipid droplet, and confocal image of an adipocyte in which a large lipid droplet (orange) occupies most of the cell volume, with the nucleus shown in blue. e) Schematic illustration of the intracellular WGM laser formed by a polystyrene microsphere, internalized by natural endocytosis. Confocal laser scanning microscopy images show a macrophage with cytoplasm (red), nucleus (blue), and the internalized microsphere resonator (green). Maximum intensity projection (top) and cross-section along the dashed line (bottom). Image credits: a) Reproduced with permission from ref [53]. Copyright 2013, Springer Nature. b) Reproduced with permission from ref [54]. Copyright 2014, The Royal Society of Chemistry. c,d) Reproduced with permission from ref [39]. Copyright 2015, Springer Nature. e) Reproduced with permission from ref [40]. Copyright 2015, American Chemical Society. 5

Figure 1.3: a) Spectra of microbead lasers internalized in cells at different time intervals demonstrate their stability and, therefore, long-term cell tracking. b) Demonstration of a microfluidics setup used to read spectra from microcavities inside cells. Hundreds of cells flowed from one side to the other and back. This setup demonstrates the tracking of free-floating cells. c) Optical transmission images of the tumor spheroid at three different times (left) and the spatial distribution of microdisk lasers inside the spheroid tumor (right). d) Confocal images of cells containing microdisk lasers (red) passing through holes in a membrane. Image credits: a) Reproduced with permission from ref [40]. Copyright (2015) American Chemical Society. b) Reproduced with permission from ref [60]. Copyright (2017) The Royal Society of Chemistry. c) Reproduced with permission from ref [38]. Copyright (2019) Springer Nature. d) Reproduced with permission from ref [61]. Copyright (2018) The Author(s). 7

Figure 1.4: a) Demonstration of a microdisk cavity stamped onto a drug package for anticounterfeiting applications, along with its spectrum. b) WGM spherical lasers with different ratios of acceptor to donor, which result in different lasing at the same pump fluence. c) Coding by utilizing the four possible lasing states (as shown in panel b), which must be read at the right pumping power to yield the correct information. d) A label containing droplet microcavities embedded in a polymeric matrix and attached to clothing. e) Representation of an array of droplets as a photonic barcode and their spectra. f) A thin, undulating membrane (yellow patch) that acts as a DFB laser is attached to the banknote for anticounterfeiting. The lasing remains stable even when the banknote is bent. Image credits: a) Reproduced with permission from ref [75]. Copyright (2017) Wiley-VCH Verlag GmbH & Co. KGaA, Weinheim. b,c) Reproduced with permission from ref [76]. Copyright (2020) The Author(s). d,e) Reproduced with permission from ref [77]. Copyright (2021) American Chemical Society. f) Reproduced with permission from ref [78]. Copyright (2018) The Author(s). 10

Figure 1.5: PUF-based optical labels for authentication and sensing. a) Generation of binary keys from a fluorescence microscope image of an ErB-doped CS particle embedded in gelatin. b) Fluorescence images of silk fibroin matrices genetically encoded with different fluorescent proteins under distinct excitation and emission, used for the extraction of digitized PUF keys. c) Schematic illustration of a silk-based PUF label doped with microdiamonds, showing workflow from optical emission collection to digital key generation. d) Application of optical labels for anti-counterfeiting and humidity sensing, including a photograph of an apple with a printed QR code, a magnified view of the printed QR pattern, and a printed QR code on a plastic container. Image credits: a) Reproduced from Ref. [83]. Copyright (2023) The Authors. Published by American Chemical Society, licensed under CC BY 4.0. b) Reproduced from Ref. [84]. Copyright (2022) The Authors. Published by American Chemical Society, licensed under CC BY 4.0. c) Reproduced with permission from Ref. [85]. Copyright (2021) Wiley-VCH GmbH. d) Reproduced from Ref. [86] with permission from Springer Nature. . 12

Figure 1.6: a) Schematic of a biological DFB laser based on riboflavin-doped gelatin, together with atomic force microscopy height profile profiles comparing different grating corrugation depths. b) Scanning electron microscopy (SEM) image of the side view of the photoresist grating designed by laser-interference-lithography (LIL) and diffraction colors under bending of the freestanding DFB laser. c) Illustration of vitamin-based microdroplets trapped in a polymer microwell and fluorescence image of a microsphere embedded within the microwell above lasing threshold (scale bar: 10 µm) d) Schematic of a chlorophyll laser based on an optofluidic ring resonator (OFRR). The right side shows the OFRR cross-section and the WGM circulating along the resonator (D = 80 µm; d= 2 µm). e) Optical image of a dye-doped goose egg-white microsphere; inset shows the microsphere under pulsed laser excitation. f) Emission spectra of curcumin- and modified-curcumin-based microspheres of different sizes; inset shows optical images of the corresponding microcavities. Image credits: a) Reproduced from Ref. [101] with permission from The Royal Society of Chemistry. b) Reproduced from Ref. [102] with permission from The Royal Society of Chemistry. c) Reproduced with permission from Ref. [57]. Copyright (2013) Wiley-VCH Verlag GmbH & Co. KGaA, Weinheim. d) Reproduced from Ref. [103] with permission from The Royal Society of Chemistry. e) Reproduced with permission from Ref. [105]. Copyright (2020) IOP Publishing Ltd. f) Reproduced with permission from Ref. [106]. Copyright (2016) Wiley-VCH Verlag GmbH & Co. KGaA, Weinheim. 15

Figure 1.7: Conceptual overview of completely edible microlasers, from materials to applications. Edible components can serve as gain media (e.g., chlorophyll or riboflavin), optical cavities (e.g., oil-based droplets or solid microspheres), and other essential elements such as surfactants, silver leaf, and supporting matrices (e.g., gelatin or agarose). These materials enable different microlaser and microcavity configurations, including WGM and FP. The resulting emission can be exploited for optical barcoding and sensing in food and other consumable products. 17

Figure 2.1: Schematics of different types of microcavities a) Whispering-gallery-mode (WGM), b) Fabry–Pérot (FP), c) Distributed-feedback (DFB), and d) Random laser. 20

Figure 2.2: Comparison of emission properties. a) Spontaneous fluorescence emission. b) Emission from a microcavity or microlaser. The main differences include the emission spectrum width, output nonlinearity, polarization, and the presence of spatial modes. 29

Figure 2.3: Schematic illustration of single- and multi-mode laser emission represented as barcodes. a) Single-mode emission from a DFB laser, tunable via the grating periodicity. b) Emission from a random laser showing irregular spectral modes. c) Multi-mode emission from FP cavities with different cavity lengths, exhibiting distinct FSR. d) Multi-mode emission from WGM microcavities of different sizes, also showing characteristic FSR spacing. 30

Figure 2.4: Principles of multiplexing. a) A single barcode can consist of multiple microcavities, greatly increasing the number of possible unique barcodes. b) Barcoding principle in which any number of unique states can be selected to create a single barcode. Unlike (a), where the barcode is defined by a fixed number of microcavities, here the barcode is encoded by the presence ("1") or absence ("0") of each state. 31

Figure 3.1: Stepwise extraction of chlorophyll from spinach: a) deveining, b) grinding, c) phase separation, and d) solvent evaporation to obtain the chlorophyll extract (photo credit: Ana Krišelj). 35

Figure 3.2: a) Chlorophyll-doped oil droplets inside water under the illumination of a blue pulsed laser. b) Riboflavin-doped water-glycerol solution was sprayed onto a spinach leaf, and the fluorescence of the resulting droplets was imaged. 37

Figure 3.3: a) Schematic of the experimental setup for the generation of monodisperse droplets. b) Photograph of the setup taken during the experiment. 38

Figure 4.1: a) Bright-field image of polydispersed chlorophyll-doped oil droplets with a size range 20 µm to 120 µm. b) Emission spectrum (at pulse energy of 5.2 µJ) from a single chlorophyll-doped oil droplet with a diameter of approximately 100 µm shown in the inset. c) The output power of a droplet laser (same as in b) shows a typical threshold behavior as the input pulse energy is increased. d) Laser emission spectrum from a bixin-doped oil droplet under the excitation of a pulsed laser at 450 nm. 45

Figure 4.2: Laser emission spectra from droplets dispersed in water, upon illuminating with a blue pulsed laser, a) from an extracted chlorophyll droplet, and b) an olive oil droplet. 47

Figure 4.3: a) Extracted chlorophyll droplets inside agar matrix positioned under the microscope and illuminated with green CW laser, and the image of the droplets was recorded. b) WGM modes emission under the illumination of a green CW laser. c) Laser emission spectrum from a single droplet under the illumination of a green pulsed laser; the droplet is shown in the inset. 47

Figure 4.4: a) Illustration of an edible WGM laser as a dye-doped droplet on a superhydrophobic surface. b) Image of riboflavin-doped water-glycerol solution sprayed onto a CYTOP-coated glass substrate. c) Laser emission spectrum from a single droplet shown in the inset. 48

Figure 4.5: a) Riboflavin-doped water-glycerol solution was sprayed onto a spinach leaf, and the fluorescence of the resulting droplets was imaged. b) The spinach leaf was positioned on the microscope and excited by a blue pulsed laser to achieve lasing. c) Laser emission spectrum (at pulse energy of 4 µj) from a single droplet shown in the inset. d) Output of a droplet laser (same as in c) on a leaf as the pump energy is increased shows typical threshold behavior. 48

Figure 4.6: a) Bubble formed from a blended mixture with a size of approximately 1.5 mm, under the illumination of blue pulsed laser, and b) resulting emission spectrum. 49

Figure 4.7: a) Schematics of the chlorophyll-coated silica microspheres and image of chlorophyll-coated silica microspheres with a mean size of 52.10 µm, one of them is under the excitation of CW laser (highlighted with a red cross). b) Emission spectrum from a single chlorophyll-coated silica microsphere (diameter of 53.06 ± 0.06 µm) immersed in water. The corresponding microsphere is shown in the inset. c) Comparison of the emission spectra of chlorophyll-coated silica microspheres of three different sizes (41.42 µm, 53.06 µm, and 66.90 µm). The colored arrows indicate the free spectral range for each microsphere, which decreases with increasing microsphere size. 50

Figure 4.8: a) Microscopic view of the generation of monodisperse droplets. b) Bright-field image of monodisperse chlorophyll-doped oil droplets. c) A typical size distribution of droplets within one sample. 51

Figure 4.9: a) Fluorescence image of monodisperse chlorophyll-doped oil droplets (mean diameter 39.49 ± 0.15 µm) and a lasing spectrum of a single droplet. b) Fluorescence image of monodisperse chlorophyll-doped oil droplets (mean diameter 94.85 ± 0.22 µm) and a lasing spectrum of a single droplet. 52

Figure 4.10: a) Size distribution of chlorophyll-doped oil droplets of 14 different diameters produced by a droplet generator chip. b) Distribution of droplet sizes detected in the jar after the date of "Stop Food Waste Day" was encoded by adding selected droplet sizes into the sample. All sizes were reliably detected. c) Schematics of the experimental setup for reading the barcodes, which includes an optical fiber for excitation and collection of the emission signals. d) Reading of an edible barcode based on chlorophyll-doped oil droplets in a jar of compote. The food product is scanned by a nanosecond pulsed laser at 440 nm. Droplet sizes are calculated from the acquired spectra, and the corresponding barcode is reconstructed. 54

Figure 4.11: a) Size distribution of chlorophyll-coated silica microspheres from three samples of distinct sizes, obtained by analyzing the emission spectrum of 60 individual microspheres per sample. b) Size distribution of a single sample of chlorophyll-coated silica microspheres dispersed in water at 0 and 15% sugar concentration, showing that the size distribution is independent of sugar concentration. 55

Figure 4.12: a) Illustration of an optical fiber integrated with focusing optics designed to illuminate microspheres and collect their emission in a real-time application. b) Agarose matrix containing chlorophyll-coated silica microspheres inside a honey bottle (agarose patch attached to the inner wall of an empty glass jar, which was subsequently filled with honey), illuminated by a CW laser, and c) emission spectrum collected from agarose matrix. d) Agarose matrix containing chlorophyll-coated silica microspheres attached to an apple surface, illuminated by a green CW laser. e) Emission spectra of chlorophyll-coated silica microspheres inside the agarose matrix at 0 and 6 months, under the excitation of CW laser, note that the agarose film was fully dried before the six-month measurement. 56

Figure 4.13: a) Size distribution of chlorophyll-coated silica microspheres within the agarose matrix, measured at 0 and 6 months, by illuminating individual microspheres with a laser. b) Schematics of an agarose patch containing chlorophyll-coated silica microspheres as PUFs, with line scanning used to illuminate the microspheres. c, d) Integrated emission spectra from line scans of agarose patches (200 µm × 500 µm) containing chlorophyll-coated silica microspheres c) Spectra from four different patches, each with 4–5 microspheres, d) Spectra from repeated scans of a single patch with five microspheres, with each spectrum representing one scan. . . . 58

Figure 4.14: The refractive index was measured for different concentrations of glucose in water. The red line represents the refractive index determined from the lasing spectrum of the droplets, while the blue line corresponds to measurements obtained using a conventional refractometer. 60

Figure 4.15: a) Schematic diagram of the temperature indicator before and after exposure to a high temperature, and bright-field images of the temperature sensor based on a chlorophyll-doped butter bead at low and high temperatures. b) Emission spectra from a temperature sensor at room temperature and after it has been exposed to a high temperature (35 °C). c) Emission spectra from a chlorophyll-doped butter microsphere at various temperatures upon the excitation with a blue pulsed laser. 60

Figure 4.16: a) Comparison of refractive index measurements: a) of sugar solutions at different concentrations, and b) across various media using edible microcavities by directly dispersing chlorophyll-coated silica microspheres inside the solutions and measuring with a refractometer. c) Schematic of a wine bottle containing chlorophyll-coated silica microspheres, which can serve as a barcode. d) Emission spectra of chlorophyll-coated silica microspheres dispersed in two different sugar solution concentrations. . 62

Figure 4.17: a) Schematic of chlorophyll-coated silica microspheres embedded within a chitosan hydrogel matrix at pH 7 and pH 3. As the pH decreases, the chitosan swells progressively, taking up more water and thereby reducing its refractive index. b) Chitosan film immersed in various pH solutions, with its weight measured at different time intervals, and the swelling behavior was significantly pH-dependent. c) Comparison of refractive indices measured using edible microcavities and a refractometer. A chitosan film embedded with chlorophyll-coated silica microspheres was immersed in solutions of known pH, and the refractive indices obtained from both methods showed good agreement. d) Emission spectra of chlorophyll-coated silica microspheres embedded within a chitosan film were measured while immersed in solutions of different pH. 63

Figure 4.18: a) Schematics of an edible FP cavity laser. The cavity is filled with chlorophyll-doped oil and illuminated by a pulsed laser. The excitation/emission light enters/exits at the position where the silver leaf is only present on one side of the cavity. b) Side view of an edible FP cavity laser. c) Laser emission spectrum (at pulse energy of 6.5 µJ) from an edible FP cavity shown in the inset. d) Output of a FP cavity laser (same as in c) as the pump energy is increased, shows typical threshold behavior. 64

Figure 4.19: a) Schematic diagram of the edible FP cavity-based pH sensor at two different pH values. The chitosan layer swells as the pH is reduced, changing the emission of the laser. b) Emission spectra from an FP cavity pumped with a nanosecond pulsed laser at 440 nm at two different pH values. c) The change of FSR with respect to the pH change. d) An edible FP-laser pH sensor inside a milk bottle measures the pH of milk. e) Change of the milk's pH over two days when left at room temperature, measured by a FP laser and a pH meter on two different samples. Lowering of the pH indicates milk spoilage. 65

Figure 4.20: a) Schematic diagram of the microlaser-based microorganism sensor before and after the growth of microorganisms, and images of the microorganism sensor before (day 0) and after (day 5) the growth of bacteria (view from top). b) Emission spectra from the microorganism sensor before (day 0) and after the growth of bacteria (day 5). 66

List of Tables

Table 3.1: List of the edible dyes that we investigated as gain media for different laser configurations. 34

Table 3.2: List of the edible materials that we investigated as optical cavities for different laser configurations. Not all evaluated materials are discussed further in this thesis, as only a subset was selected for the demonstrations presented. 36

Table 4.1: Average diameters and diameter standard deviations of the chlorophyll-doped oil droplets produced by the droplet generator chip (based on the emission spectra of individual droplets), which were used for barcoding. For each sample, 50 droplets were analyzed. 53

Abbreviations

CS	...	corn starch
CV	...	coefficient of variation
CW laser	...	continuous wave laser
CYTOP	...	cyclic transparent optical polymer
DFB	...	distributed feedback
ErB	...	erythrosine B
FP	...	Fabry–Pérot
FSR	...	free spectral range
FWHM	...	full width at half maximum
GFP	...	green fluorescent protein
ICG	...	indocyanine green
PUFs	...	physically unclonable functions
Q-factor	...	quality factor
QR	...	quick response (code)
QY	...	quantum yield
RFID	...	radio-frequency identification
SD	...	standard deviation
SERS	...	surface-enhanced Raman scattering
TE	...	transverse electric
TM	...	transverse magnetic
TEOS	...	tetraethoxysilane
Tween20	...	polyoxyethylene (20) sorbitan monolaurate
WGM	...	whispering gallery mode

Chapter 1

Introduction

1.1 Background and Motivation

Ensuring the authenticity, quality, and safety of food and pharmaceutical products has become a critical global challenge. Counterfeiting, adulteration, and the distribution of substandard products pose serious risks to public health and result in significant economic losses worldwide. At the same time, food waste remains a major concern, with large quantities of consumable products discarded each year based on predetermined expiration dates or "best before" dates, even when they may still be safe for consumption. Globally, nearly one-third of all food produced is lost or wasted, contributing to economic loss, environmental impact, and increased food insecurity [1].

To address these challenges, a wide range of anti-counterfeiting, authentication, and freshness-monitoring technologies have been developed and implemented across the food and pharmaceutical sectors. Conventionally laboratory-based analytical techniques—such as isotope and elemental fingerprinting, mass spectrometry, DNA barcoding, and chromatography analysis—are widely considered as the gold standard for product verification [2], [3]. These methods offer high sensitivity and chemical specificity, enabling reliable detection of adulteration or counterfeit products. However, they require expensive instrumentation, trained personnel, and a laboratory environment [4]. Consequently, they are time-consuming and impractical for continuous, distributed, or large-scale monitoring across complex supply chains.

In most commercial supply chains, product authentication is primarily achieved through external packaging-based approaches. These include printed barcodes and QR codes, holographic labels, security seals, invisible inks, watermarks, and radio-frequency identification (RFID) tags [5]. Such technologies are relatively inexpensive, easy to implement, and compatible with existing packaging. Nevertheless, they suffer from inherent limitations. External labels can be removed, duplicated, or replaced, providing only limited protection against counterfeiting. Moreover, these solutions are ineffective for unpackaged, bulk, or processed products, and they do not provide direct information about the internal quality or freshness of the product itself.

In parallel, significant research efforts have focused on the development of freshness sensors and intelligent or smart packaging technologies [6], [7]. These systems typically monitor parameters such as pH, humidity, temperature, gas composition (such as oxygen or carbon dioxide), and microbial activity using colorimetric, fluorescent, or electrochemical indicators. While such sensors can provide valuable information about storage conditions and product degradation, many suffer from limited sensitivity, poor long-term stability, or a primarily qualitative rather than quantitative readout. Importantly, most of these sensors are integrated into external packaging rather than into the consumable product

itself, contributing to packaging waste and limiting full edibility or biodegradability.

These limitations have motivated growing interest in alternative approaches that enable direct, intrinsic tagging and sensing within consumable products themselves. Embedding authentication tags and sensors directly into food or pharmaceutical products could significantly enhance security against tampering, improve traceability, and reduce reliance on external packaging. Ideally, such embedded tags should be fully edible, non-toxic, and capable of providing real-time information about product authenticity and freshness, without compromising safety or altering taste, appearance, or other properties. Furthermore, they should enable high-capacity encoding and non-contact readout. In this context, optical barcodes based on micro- and nanoscale photonic structures offer a particularly promising approach [8].

1.2 Optical Microbarcodes

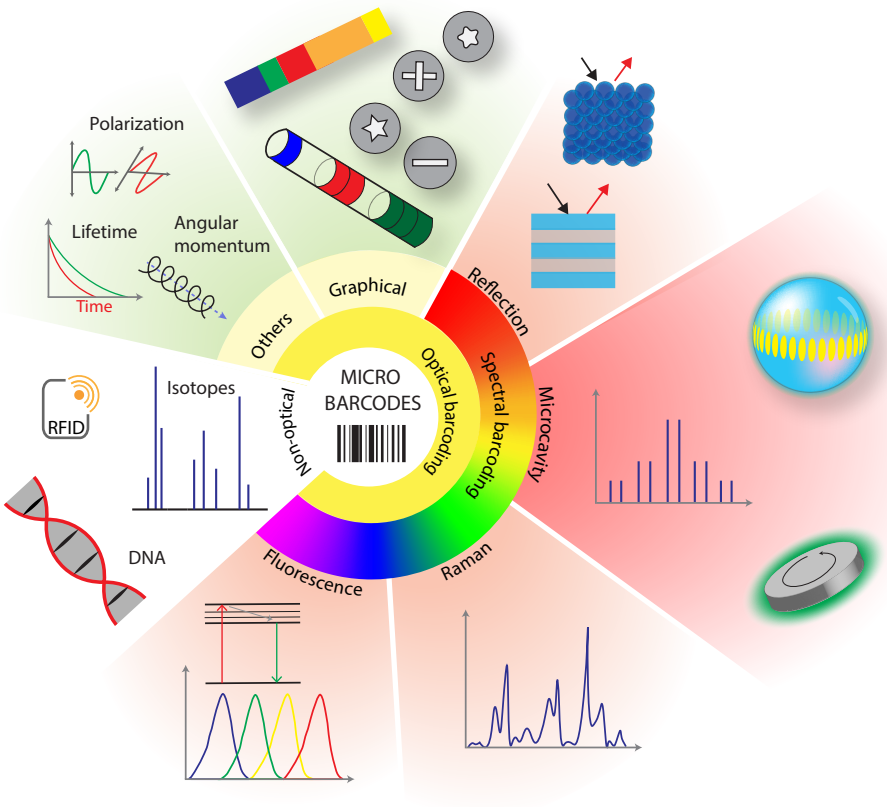


Figure 1.1: Schematic overview of different types of microbarcodes and their encoding mechanisms. Microbarcodes include non-optical identifiers (RFID, isotopes, and DNA) as well as optical encoding schemes based on graphical patterns, spectral responses (fluorescence, Raman scattering, reflection, and microcavity resonances), and additional physical parameters such as polarization, lifetime, or angular momentum.

Optical microbarcodes provide a versatile platform for product labeling, authentication, and sensing, while enabling high encoding capacity, non-contact readout, and convenient integration with miniaturized systems. Unlike conventional macroscopic barcodes or la-

bels, which are restricted to external packaging, optical microbarcodes can be embedded directly at the micro- or nanoscale within products themselves. This intrinsic integration substantially enhances protection against tampering, label removal, or replacement. As a result, optical microbarcodes have found broad applications in anti-counterfeiting and product authentication, multiplexed bioassays, cell tracking, and environmental sensing, where compactness and high multiplexing capacity are critical.

Depending on the encoding strategy, optical microbarcodes can be broadly categorized into three classes: graphical, spectral, and additional physical encoding schemes, including polarization, lifetime, and angular momentum, as shown in Figure 1.1 [9], [10]. Each category offers distinct advantages and limitations in terms of encoding capacity, readout complexity, and suitability for specific applications, which are discussed in detail below.

1.2.1 Graphical barcodes

Graphical microbarcodes use visual or spatial patterns, such as linear sequences or two-dimensional shapes, to encode information, similar to conventional macroscopic barcodes and QR codes. Examples include metal nanowire-based striped tags [11], multicolor barcodes encoded within a single upconversion crystal [12], polymer microparticle-based barcodes [13], and spatially selective photo-bleached microcarriers [14]. These barcodes can be read using standard imaging equipment, such as optical microscopes and cameras, making them relatively straightforward to implement. However, graphical barcodes face several inherent limitations. Successful readout requires proper orientation of the barcode within the focal plane and a clear optical path, which can be challenging in scattering or opaque media. In addition, the minimum size of graphical barcodes is ultimately limited by the optical resolution of the imaging system. Although sub-micrometer graphical barcodes have been demonstrated, their readout typically requires super-resolution microscopy techniques, which significantly limits scalability and practical implementation [15].

1.2.2 Spectral barcodes

Spectral barcodes encode information in the optical spectrum rather than spatial patterns, making them inherently independent of barcode orientation and enabling rapid and high-throughput readout. Fluorescence-based encoding is the most widely used spectral approach, owing to its ease of readout and the tunability of emission spectra through the choice of fluorophores. Examples include fluorescent dye-doped micro- and nanoparticles [16], [17], fluorescent nanorods [18], DNA-based fluorescence nanobarcodes [19], and genetically encoded fluorescent barcodes for cellular multiplexing [20]. Among fluorescent materials, organic dyes are widely used due to their widespread availability, while quantum dots and fluorescent proteins are commonly employed in biological applications because of their improved photostability and biocompatibility [21], [22].

Despite their widespread use, fluorescent barcodes suffer from photobleaching and relatively broad emission spectra, which limit their long-term stability and restrict encoding capacity. As an alternative to fluorescence, Raman scattering can also be exploited for spectral barcodes [23]. Raman-barcodes offer several advantages, including good photostability, high multiplexing potential, and their signals can be spectrally separated from fluorescence backgrounds. However, spontaneous Raman signals are inherently weak and can overlap with background signals from other molecules in complex samples [23]. These challenges can be addressed by using novel Raman dyes with a large Raman shift, which minimize spectral overlap and increase barcoding capacity [24], [25], [26]. In addition, surface-enhanced Raman scattering (SERS) is frequently used to amplify Raman signals by several orders of magnitude [27], [28], [29], [30], [31]. Nevertheless, Raman-based bar-

coding remains less common than fluorescence-based approaches, mainly due to signal detection challenges.

Beyond emission-based methods, reflection spectra can also be exploited for optical barcoding. Photonic crystal structures generate structural color through Bragg reflection, with the reflected wavelength determined by the periodicity and refractive index of the material. Such photonic crystal barcodes have found applications in sensing, anti-counterfeiting, and multiplexed bioassays [32], [33]. Similarly, interference effects in dielectric microstructures, including spherical microresonators, can produce unique reflection spectra suitable for encoding [34].

1.2.3 Microcavity- and microlaser-based barcodes

Within the broader category of spectral encoding, barcodes based on microcavities and microlasers represent a powerful and rapidly growing subclass, which supports optical resonances with ultra-narrow linewidths, enabling exceptionally high multiplexing capacity within a limited spectral range [8], [35], [36]. As a result, millions of spectrally distinct and uniquely distinguishable barcodes can be generated from small variations in cavity geometry, size, or refractive index [8], [37], [38].

Microcavity and microlaser-based barcodes have been widely explored for applications in multiplexed biosensing, cell labeling and tracking, anti-counterfeiting, and product authentication [37], [38], [39], [40], [41]. Beyond labeling or tagging, microcavities inherently function as highly sensitive optical sensors: changes in the local environment–such as refractive index, molecular binding, or chemical composition–lead to measurable spectral shifts in resonance wavelength, linewidth, or lasing threshold [42], [43], [44], [45], [46].

To date, most demonstrations of microcavity-based barcodes have been carried out in biomedical contexts, where biocompatible microresonators are integrated into cells, tissues, or biological media. These studies provide important insights into how microcavity lasers behave in complex, aqueous, and scattering environments. In the following section, these developments are discussed in the context of biolasers, highlighting key findings from biological lasers and how these concepts can be translated into edible and food-compatible microlasers.

1.3 Biolasers

Biolasers are optical lasers in which biological or biocompatible materials serve as the gain medium, the resonant cavity, or both. Structurally, they are similar to conventional lasers, consisting of an optical cavity, a gain medium, and an external pump source. They are distinguished by the use of naturally derived, biocompatible, or biodegradable components, which enable laser operation within or in close proximity to living cells and tissues. When introduced into biological systems through implantation, injection, or cellular uptake, biolasers can function as localized optical probes that provide information about their surrounding environment, enabling the monitoring of molecular-, cellular-, and tissue-level processes with exceptional sensitivity [47], [48], [49], [50], [51], [52].

In biolasers, the gain medium can consist of biological entities themselves, such as cells, tissues, or viruses, or biologically derived fluorophores embedded within a cavity. Because the lasing output is highly sensitive to the optical properties of the gain medium and its local environment, subtle biological change—such as variations in refractive index, molecular concentration, or biochemical activity—can lead to measurable shifts in lasing threshold, intensity, or emission wavelength.

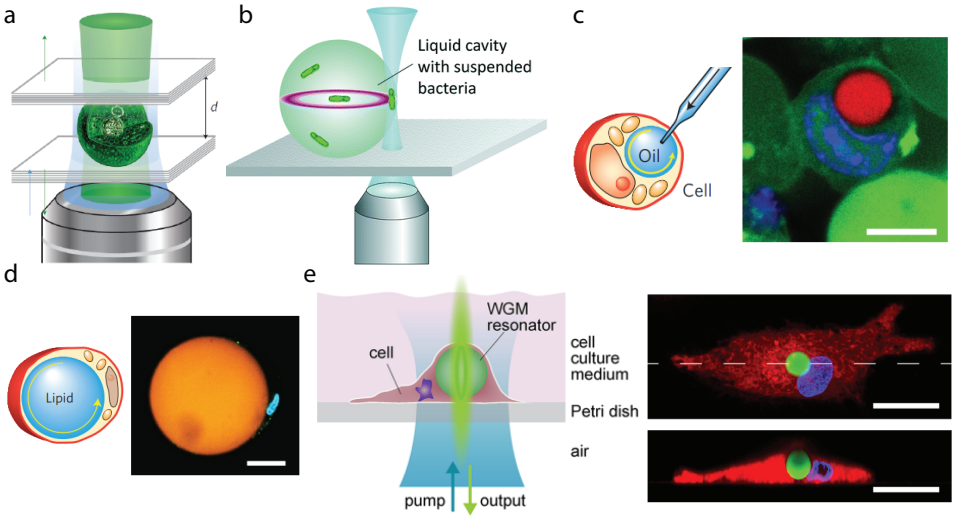


Figure 1.2: a) Illustration of the single-cell laser where a live eGFP-expressing 293ETN cell is positioned inside an optical resonator composed of two highly reflective distributed Bragg reflectors. b) Schematic illustration of lasing emission from live E. coli bacterial cells expressing the Venus fluorescent protein. The bacteria are suspended and freely mobile within glycerol–water microdroplets on a superhydrophobic surface. c) Schematic illustration of the oil injection into the cytoplasm of a cell, alongside a confocal fluorescence image showing a polyphenyl ether droplet doped with Nile red dye (red) and the cell nucleus (blue). d) Schematic illustration of a mature subcutaneous adipocyte containing a lipid droplet, and confocal image of an adipocyte in which a large lipid droplet (orange) occupies most of the cell volume, with the nucleus shown in blue. e) Schematic illustration of the intracellular WGM laser formed by a polystyrene microsphere, internalized by natural endocytosis. Confocal laser scanning microscopy images show a macrophage with cytoplasm (red), nucleus (blue), and the internalized microsphere resonator (green). Maximum intensity projection (top) and cross-section along the dashed line (bottom). Image credits: a) Reproduced with permission from ref [53]. Copyright 2013, Springer Nature. b) Reproduced with permission from ref [54]. Copyright 2014, The Royal Society of Chemistry. c,d) Reproduced with permission from ref [39]. Copyright 2015, Springer Nature. e) Reproduced with permission from ref [40]. Copyright 2015, American Chemical Society.

Importantly, previous work on biolasers has provided several key insights that are directly relevant to the development of edible microlasers. First, these studies have demonstrated that stable lasing can be achieved in soft, aqueous, and structurally complex environments, which are comparable in many ways with food products. Second, they have shown that microcavities can function reliably in complex media while maintaining narrow spectral features. Third, they have established that lasing spectra are highly sensitive to local refractive index changes, forming the basis for sensing and barcoding–principles that are central to this thesis.

Consequently, the selection of gain materials in biolasers requires a careful balance between optical performance and biocompatibility. Fluorescent proteins such as GFP (green fluorescent protein), mCherry (monomeric Cherry), and ICG (indocyanine green) are among the most commonly used gain materials due to their high quantum yield, photostability, and compatibility with living systems [54], [55], [56]. Naturally occurring fluorophores, including riboflavin and luciferin, have also been employed as gain media in

biolasers [57], [58].

Biolasers can be broadly classified according to the position of the optical resonator relative to the biological system: extracellular and intracellular configurations. In extracellular biolasers, resonators are located outside the cell, while biological material acts as or contains the gain medium. They are most commonly demonstrated using FP cavities, in which fluorophore-stained or fluorescent protein expressing cells are placed between two reflective mirrors (Figure 1.2a). Similar approaches have been demonstrated using fluorescent bacteria embedded in microdroplet cavities or biofilms (Figure 1.2b).

Intracellular biolasers are realized when the entire resonator is internalized by the cell. WGM cavities are particularly well suited for this purpose due to their compact size, high quality factor (Q factor), and low lasing threshold. Early demonstrations employed dye-doped oil droplets as soft intracellular resonators (Figure 1.2c), as well as naturally occurring lipid droplets in adipocytes stained with lipophilic dyes (Figure 1.2d). Solid microresonators, such as polymer microspheres and microbeads internalized via endocytosis, have also been widely used (Figure 1.2e). The resulting lasing spectra are highly sensitive to cavity size and refractive index, enabling unique optical identification and sensing at the single-cell level.

Beyond single cells, biolaser concepts have been extended to viruses and tissues, including virus-based lasers that exploit the highly ordered structure of viral capsids, as well as tissue lasers based on either random lasing or implanted WGM resonators [59].

Overall, research on biolasers has established the fundamental physical and optical principles that underpin microcavity-based lasers in complex environments. Their spectral stability, narrow linewidths, and sensitivity to local refractive index variations provide the foundation for optical barcoding, sensing, and tagging strategies, which are discussed in the following section.

1.4 State of the Art Applications of Microcavity-Based Barcodes

1.4.1 Cell tagging and tracking

Building on the optical properties discussed in the previous sections–such as narrow linewidth emission, refractive-index sensitivity, and spectral encoding–optical microcavities and microlasers have been widely explored as tools for cellular barcoding and tracking. Unlike conventional fluorescent labels, which primarily serve as imaging markers, microcavity-based microlasers act as physically embedded optical identifiers whose lasing spectra provide unique signatures. This capability has enabled intracellular tagging and long-term tracking of cells both in vitro and in vivo.

Cells can internalize microcavities via endocytosis, allowing the generation of spectrally distinct barcodes. Compared to traditional fluorescent probes, microcavity-based barcodes offer several key advantages: (i) much narrower emission linewidths, enabling higher encoding capacity; (ii) spectral stability over time, and (iii) the ability to encode information not only in emission wavelength but also in cavity-specific properties such as free spectral range (FSR), mode structure, and lasing threshold. These characteristics are directly linked to the fundamental lasing behavior discussed in the previous section and are also highly relevant to the development of edible microlaser-based barcodes.

In the context of this thesis, the primary relevance of cell tagging is not biological tracking itself, but what these studies reveal about microlaser performance in complex, dynamic, and scattering environments. The spectral stability, multiplexing capability, and readout strategies developed for cell barcoding are directly applicable to edible microlasers

embedded in food.

1.4.1.1 In vitro demonstrations

The first fully intracellular laser was demonstrated in 2015, where 10 µm to 20 µm diameter polymer microbeads were internalized by various cell types, including HeLa, NIH 3T3, and HEK 293 cells [39], [40]. The cells remained viable for several weeks, and the lasing spectra of individual cells could be recorded over time, enabling unambiguous identification and tracking of single cells (Figure 1.3a). Although prolonged exposure to pump pulses above the lasing threshold could damage cells, it was demonstrated that a single excitation pulse above threshold was sufficient to decode the spectral barcode, thereby minimizing phototoxic effects.

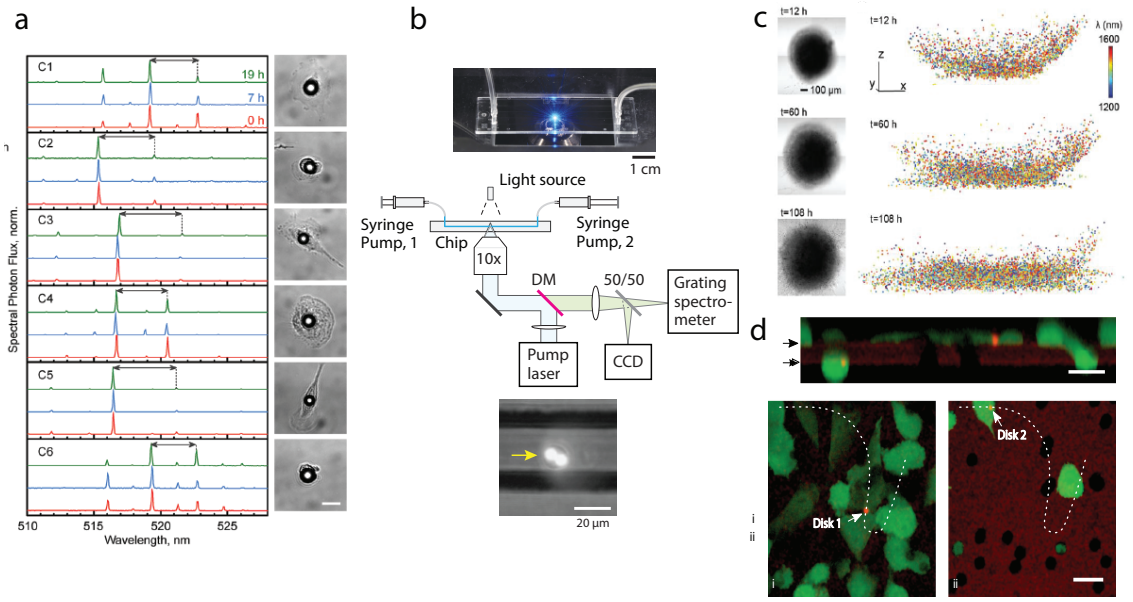


Figure 1.3: a) Spectra of microbead lasers internalized in cells at different time intervals demonstrate their stability and, therefore, long-term cell tracking. b) Demonstration of a microfluidics setup used to read spectra from microcavities inside cells. Hundreds of cells flowed from one side to the other and back. This setup demonstrates the tracking of free-floating cells. c) Optical transmission images of the tumor spheroid at three different times (left) and the spatial distribution of microdisk lasers inside the spheroid tumor (right). d) Confocal images of cells containing microdisk lasers (red) passing through holes in a membrane. Image credits: a) Reproduced with permission from ref [40]. Copyright (2015) American Chemical Society. b) Reproduced with permission from ref [60]. Copyright (2017) The Royal Society of Chemistry. c) Reproduced with permission from ref [38]. Copyright (2019) Springer Nature. d) Reproduced with permission from ref [61]. Copyright (2018) The Author(s).

Barcoding using fluorescent microspheres was shown to be feasible in both the spontaneous emission and lasing regimes [39], [40], [49]. Moreover, cells naturally internalize multiple microspheres, this approach enables combinatorial barcoding of large cell populations [39], [40], [49], [60], [62]. In one representative example, near-infrared intracellular WGM microlaser probes with narrow emission (approximately 2 nm) were fabricated from organic materials and coated with a silica shell [62]. By varying the microsphere diam-

eter from 3 µm to 5 µm, 150 uniquely distinguishable barcodes could be produced. Cells internalized up to five microcavities, and the barcoding was achieved using both the FSR of each microcavity and the number of microcavities per cell. By extending the diameter range to 3 µm to 10 µm while still allowing up to five microcavities per cell, the number of unique barcodes could, in principle, reach 10^{12}. This highlights the exceptional encoding capacity of microcavity-based lasers—a concept that is directly transferable to other barcoding platforms, including potential applications in food and consumable products.

Tracking becomes more challenging for free-floating cells, which move significantly faster than adherent cells (such as substrate-attached or tissue-embedded cells). Using polymer WGM microcavities, spectral tracking of hundreds of cells in a microfluidic channel was demonstrated [60] (Figure 1.3b). After reversing the flow, the same cells were successfully identified based on their spectral signatures, with 128 uniquely barcoded cells traced back to the original sample. This illustrates the robustness of laser-based barcodes in dynamic environments.

Early studies employed relatively large polystyrene beads (up to 20 µm), raising concerns about potential effects on cell behavior. Although cell viability was largely unaffected [63], [64], [65], [66], [67], [68], this motivated the development of smaller microcavities. Quantum-dot-based microbead lasers (∼4 µm) showed only ∼0.3 nm wavelength variation over three hours, attributed to local refractive-index changes inside the cell, while maintaining cell viability [69].

Further miniaturization led to 2 µm diameter semiconductor microdisk lasers (InAlGaAs or InGaAsP) coated with silica [38]. Coated disks exhibited minimal wavelength drift (0.4 nm over 30 hours), compared to 11 nm for uncoated disks. Time-lapse imaging was demonstrated to monitor the migration and proliferation of cells containing laser particles for several days.

Large-scale tracking was also demonstrated in a 3D tumor spheroid model using microdisk-tagged 4T1 breast-cancer cells (Figure 1.3c). A single-cell spheroid contains ∼70,000 microdisks. Automated 3D scans tracked the 75–80% percent of the particles over 24 hours, decreasing to ∼ 1% after 125 hours since the cell spheroid increases in size and thus the signal cannot be received from beyond the optical detection depth. Importantly, this limitation is not only relevant to biology: it indicates that laser barcodes can be detected through a finite thickness of scattering material—a point directly relevant to food or packaging environments.

AlGaInP multi-quantum-well nanodisk lasers were introduced as a less toxic, visible-emitting alternative to arsenide-based emitters [61]. Their visible emission simplifies detection using standard cameras and spectrometers, whereas infrared emission offers better spectral separation from common biological stains. These nanodisks exhibited extremely high spectral stability (wavelength drift < 50 pm) and low lasing thresholds (500-fold below typical two-photon microscopy excitation). Cells could internalize multiple nanodisks without disrupting cellular function, enabling a theoretical tagging capacity of 10^9 unique barcodes, assuming six disks per cell. Moreover, individual tagged cells could be tracked while migrating through pores as small as 5 µm (Figure 1.3d), illustrating the potential of laser barcodes for studying cell invasion.

Flow cytometry has also benefited from microcavity barcodes. Conventional cytometry is limited by the number of available fluorescence channels and cannot easily track individual cells over multiple time points. A multi-pass flow cytometry system using microdisk laser barcodes addressed this limitation [70], enabling repeated measurements of the same cells before and after drug treatments. Additionally, cell sorting in microfluidics based on intracellular microcavity spectra was demonstrated at kilohertz rates [71], highlighting the practical utility of laser barcodes for high-throughput applications.

1.4.1.2 In tissues and in vivo

While in vitro demonstrations established the feasibility of microcavity-based cellular barcodes, their practical utility ultimately depends on whether these barcodes can be reliably detected and distinguished in scattering biological tissues. This is also directly relevant beyond biomedical applications: if microlaser barcodes can be reliably read through optically turbid media such as skin or tissue, they are likely to be readable through other complex scattering environments, including heterogeneous food matrices, liquids, or packaging materials.

Long-term tracking of large numbers of cells in vivo remains challenging because tissue scattering broadens and attenuates optical signals. Nevertheless, microcavity lasers are particularly attractive for this purpose due to their narrow emission linewidths and high spectral contrast, which allow their signatures to be distinguished from background fluorescence and diffuse scattering. As an initial proof of concept, microdisk-tagged cells stained with a fluorescent dye were injected into a mouse tail vein [38]. After 15 minutes, the lung tissue was removed for ex vivo imaging. The injected cells were successfully identified, and their lasing signals were detected. This experiment demonstrates that microlasers can survive transport through complex media and remain spectrally readable—an important consideration for edible microlasers as barcodes and sensors.

To move toward true in vivo detection, quantum-dot-based single-mode WGM microbead lasers were injected subcutaneously into the abdomen of live anesthetized mice [69]. Lasing could be detected at a depth of approximately 90 µm beneath the skin surface. This provides a practical benchmark for how deeply microlaser barcodes can be read through scattering materials, which is directly translatable to detection through thick or opaque foods and packaging.

More advanced approaches have combined barcoding with functional sensing. Polymer WGM microcavities coated with pH- or temperature-responsive polymers enabled simultaneous spectral barcoding, 3D localization, and environmental sensing deep inside tissue [72]. The distinct lasing spectra of individual microcavities allowed a diffuse optical signal to be computationally decomposed into contributions from multiple resonators, facilitating their localization even in highly scattering environments. This concept—recovering individual barcodes from a mixed, scattered signal—is highly relevant for edible microlasers, where multiple resonators may be embedded in the same food product.

Furthermore, CdS-based nanowire lasers coated with multilayer collagen were used for in vivo tracking of macrophages [73], [74]. Cells carrying these nanowires were followed for up to 28 days after subretinal injection. Due to their high refractive index, the nanowires also served as strong optical coherence tomography (OCT) contrast agents, enabling 3D localization to depths of approximately 700 µm. This study highlights that microlaser barcodes can be combined with complementary imaging modalities to enhance spatial tracking in thick and scattering media.

Overall, these studies show that microcavity-based barcodes can be detected, distinguished, and localized in scattering tissues at depths ranging from tens to hundreds of micrometers. Beyond their biomedical significance, these findings provide a valuable reference framework for the development of edible microlasers: they indicate the likely detection limits and readout strategies that can be expected in optically complex, heterogeneous environments such as food products or packaging.

1.4.2 Product labeling and anti-counterfeiting

The use of microcavity-based barcodes for product labeling and anti-counterfeiting has attracted increasing attention due to the growing need for secure, reliable, and difficult-

to-replicate authentication methods. Unlike conventional printed barcodes or RFID tags, optical microcavity-based barcodes offer intrinsic physical complexity, spectral uniqueness, and environmental sensitivity, making them attractive as advanced security labels. These features allow them to function either as PUFs, which are extremely difficult to replicate, or as condition-dependent barcodes that reveal information only under specific optical readout conditions.

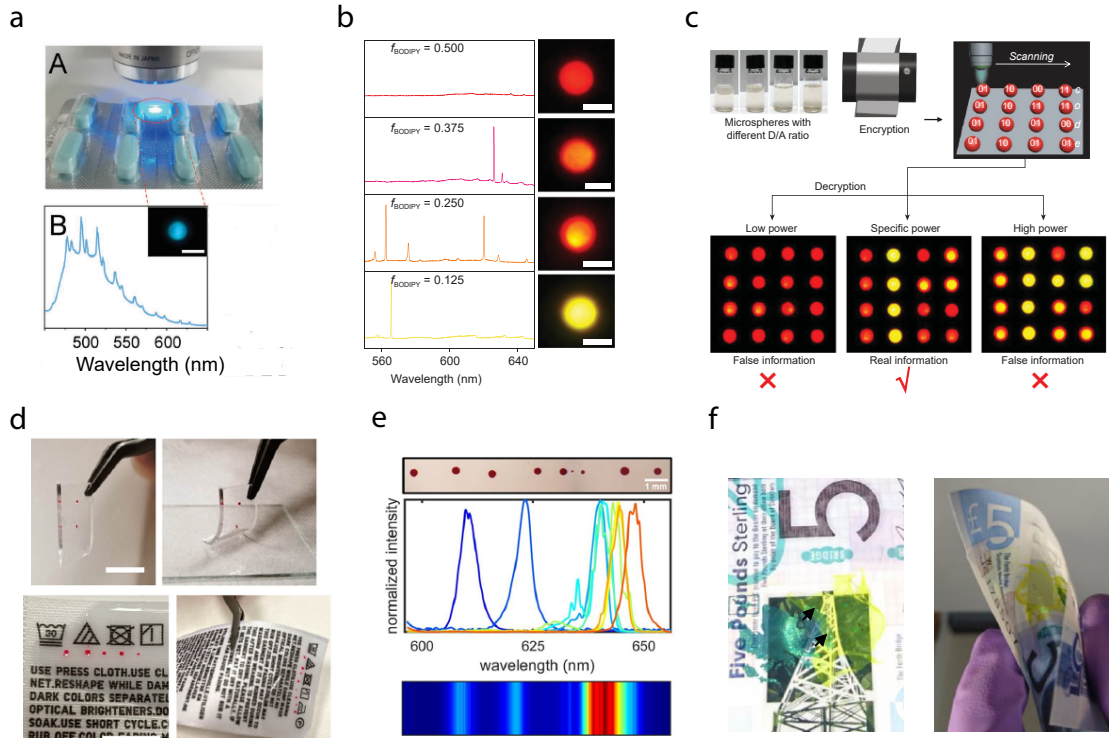


Figure 1.4: a) Demonstration of a microdisk cavity stamped onto a drug package for anticounterfeiting applications, along with its spectrum. b) WGM spherical lasers with different ratios of acceptor to donor, which result in different lasing at the same pump fluence. c) Coding by utilizing the four possible lasing states (as shown in panel b), which must be read at the right pumping power to yield the correct information. d) A label containing droplet microcavities embedded in a polymeric matrix and attached to clothing. e) Representation of an array of droplets as a photonic barcode and their spectra. f) A thin, undulating membrane (yellow patch) that acts as a DFB laser is attached to the banknote for anticounterfeiting. The lasing remains stable even when the banknote is bent. Image credits: a) Reproduced with permission from ref [75]. Copyright (2017) Wiley-VCH Verlag GmbH & Co. KGaA, Weinheim. b,c) Reproduced with permission from ref [76]. Copyright (2020) The Author(s). d,e) Reproduced with permission from ref [77]. Copyright (2021) American Chemical Society. f) Reproduced with permission from ref [78]. Copyright (2018) The Author(s).

In general, microcavity-based photonic barcodes can enhance security in two main ways. First, the barcode itself can be made structurally and spectrally complex, such that even if the design is known, exact replication is practically impossible due to fabrication variability at the micro- and nanoscale. Second, the correct information can be encoded such that it is only revealed under predefined excitation conditions, such as a specific wavelength, fluence, polarization, or temperature. Both strategies have been demonstrated using microlasers, and they form the foundation of many state-of-the-art photonic labeling schemes.

One of the earliest demonstrations of microcavity-based anti-counterfeiting used dye-doped organic microdisks stamped directly onto drug packaging (Figure 1.4a) [75]. These microdisks incorporated a dye that changed its emission color under UV illumination, meaning that the correct spectral signature could only be obtained under UV excitation. A similar concept was implemented using photo-switchable diarylethene-based microcavities, which formed two-dimensional luminescent patterns with reversible emission states under alternating UV and visible light [79]. These approaches illustrate the advantage of stimulus-responsive microlasers, where dynamic control over emission provides tunable security features. However, such approaches typically rely on synthetic dyes and polymer matrices, which are not compatible with direct integration into consumable products—an important limitation addressed in this thesis.

More advanced encoding strategies have exploited multi-state lasing behavior. In one example, microspheres containing a donor–acceptor dye pair exhibited four distinct emission states depending on the pump fluence: no lasing, single-wavelength lasing at a longer wavelength, dual-wavelength lasing, or single-wavelength lasing at a shorter wavelength [76]. By varying the donor–acceptor ratio, these states could be engineered either within a single cavity under different excitation conditions or across multiple cavities under a fixed excitation fluence (Figure 1.4b). Arranging such microlasers into two-dimensional arrays enabled high-density information encoding (Figure 1.4c). The key advantage of this approach is its multidimensional security: correct decoding requires both the right material composition and the correct excitation conditions. A related strategy employed thermo-responsive cholesteric liquid-crystal microlasers, where information was encoded in wavelength, circular polarization, and temperature dependence [80].

A more flexible platform was demonstrated using liquid droplet microcavities embedded in a PDMS matrix to form a "smart photonic label" that could be attached to substrates such as paper or fabric (Figure 1.4d) [77]. The dye-doped droplets with diameters in the range of 100 µm to 1000 µm supported WGM lasing, while the addition of TiO_2 microparticles (as a scattering medium) enabled random lasing. The lasing properties could be tuned by controlling droplet size and scatterer concentration. By arranging droplets into patterns, complex photonic barcodes could be generated (Figure 1.4e). The coexistence of WGM and random lasing increased security by introducing two distinct lasing mechanisms. However, the use of PDMS and non-edible dyes restricts direct application to food-related products.

Other emerging approaches include 2D perovskite microlasers, where geometry-dependent lasing thresholds and wavelengths were used for secure encoding [81], and random lasers based on carbon-dot fibers [82]. Additionally, free-standing membrane DFB lasers have been proposed for banknote authentication [78]. These thin films can contain multiple diffraction gratings, each acting as an independent laser source. When transferred onto a hard surface, the emission spectrum serves as a complex barcode (Figure 1.4f). Importantly, such labels have demonstrated excellent mechanical robustness, maintaining spectral stability for over 200 days and under repeated bending or twisting of the banknote [78]. Nevertheless, these approaches rely on semiconductor or polymer-based materials that are unsuitable for direct incorporation into edible or biodegradable products.

Overall, existing photonic labeling strategies demonstrate the powerful capabilities of microlasers for anti-counterfeiting, including high spectral density, tunable emission states, and robustness under mechanical deformation. However, most reported systems rely on synthetic, non-biodegradable, or potentially toxic materials, limiting their use in applications involving direct contact with food or ingestible products.

These limitations motivate the work presented in this thesis. By developing microlasers based on edible and food-compatible materials, this work aims to combine the security

advantages of microcavity-based photonic barcodes with biocompatibility, environmental sustainability, and practical applicability to product labeling in the food and packaging industries.

1.5 Recent Advances in Edible or Food-Compatible Tags

The development of edible and food-compatible tagging approaches has attracted increasing interest in recent years, as these approaches could enhance food authentication, traceability, and freshness monitoring without relying on non-edible packaging. Integrating tags and sensors directly into consumable products offers clear advantages, including enhanced resistance to tampering and improved consumer safety.

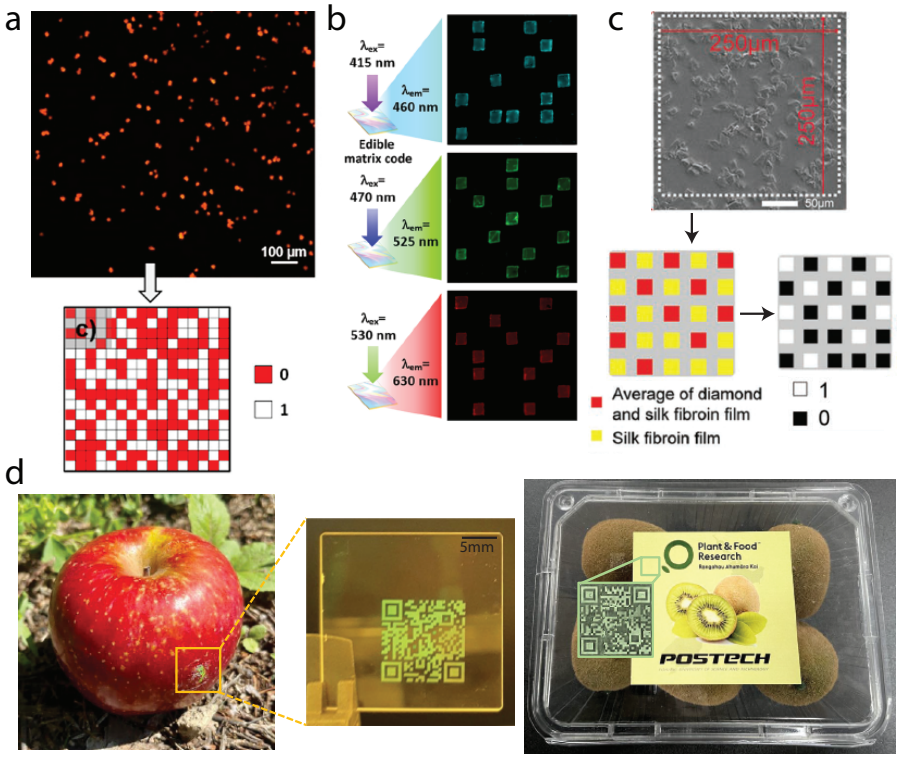


Figure 1.5: PUF-based optical labels for authentication and sensing. a) Generation of binary keys from a fluorescence microscope image of an ErB-doped CS particle embedded in gelatin. b) Fluorescence images of silk fibroin matrices genetically encoded with different fluorescent proteins under distinct excitation and emission, used for the extraction of digitized PUF keys. c) Schematic illustration of a silk-based PUF label doped with microdiamonds, showing workflow from optical emission collection to digital key generation. d) Application of optical labels for anti-counterfeiting and humidity sensing, including a photograph of an apple with a printed QR code, a magnified view of the printed QR pattern, and a printed QR code on a plastic container. Image credits: a) Reproduced from Ref. [83]. Copyright (2023) The Authors. Published by American Chemical Society, licensed under CC BY 4.0. b) Reproduced from Ref. [84]. Copyright (2022) The Authors. Published by American Chemical Society, licensed under CC BY 4.0. c) Reproduced with permission from Ref. [85]. Copyright (2021) Wiley-VCH GmbH. d) Reproduced from Ref. [86] with permission from Springer Nature.

1.5.1 Edible barcodes and tags (non-microcavity-based)

A wide range of food-compatible and biocompatible labeling strategies have been proposed for authentication and traceability that do not rely on optical microcavities or lasers. One prominent class of approaches is based on PUFs, in which random material variations generate unique and difficult-to-replicate optical signatures. For example, food-grade corn starch (CS) microparticles doped with the food colorant erythrosine B (ErB) have been developed as edible PUFs by exploiting the intrinsic randomness of particle positions when dispersed within gelatin film, together with the fluorescence of the colorant, producing stochastic fluorescence patterns suitable for authentication [83]. When examined under fluorescence microscopy, each ErB-doped CS particle distribution embedded in gelatin exhibits a distinct pattern of bright fluorescent spots, with no two patterns being identical, enabling unique encoding for authentication purposes (Figure 1.5a). The resulting fluorescence images can be further processed and converted into binary keys for identification.

Similarly, silk fibroin matrices genetically encoded with fluorescent proteins have been explored as edible optical tags for authentication and traceability [84], [87]. In this approach, silkworms are genetically modified to produce silk fibroin fused with distinct fluorescent proteins, such as cyan, green, and red fluorescent proteins, resulting in silk material with color-specific emission under optical excitation (see Figure 1.5b). The regenerated silk solutions are subsequently patterned into matrix codes on thin silk film substrates, typically arranged in two-dimensional grids where each fluorescent square contributes to a multidimensional optical tag. When excited at appropriate wavelengths, the patterned film exhibits bright fluorescence that can be captured using a smartphone camera and decoded to extract a digital authentication key.

Raman-based tagging approaches have also been reported as another class of edible or biocompatible authentication tags. For example, flexible and biocompatible PUF labels have been introduced by randomly embedding microdiamonds into silk fibroin films, where the characteristic Raman scattering signatures of the diamonds serve as the optical response for authentication (Figure 1.5c) [85]. In this approach, silk fibroin provides a biocompatible substrate, while the randomly distributed microdiamonds act as stable, Raman-active scatterers whose spatial and spectroscopic variations generate unique optical fingerprints. Upon Raman excitation, each label yields a distinct spectroscopic map that can be encoded with high capacity and strong resistance to counterfeiting.

In addition, functional edible inks and coatings have been developed for food labeling and sensing. For example, water-soluble nanocomposite inks have been shown to function simultaneously as food labels and humidity indicators, enabling visual monitoring of storage conditions and environmental exposure [86]. In this approach, colorimetric pigment nanoparticles are dispersed within biodegradable, food-safe polymer matrices that can be printed or coated directly onto food surfaces or packaging (see Figure 1.5d). The resulting inks exhibit reversible color changes in response to ambient humidity, providing qualitative information related to food quality and storage history. Since both the pigment and the polymer matrix are composed of food-safe materials, these inks are suitable for direct contact with consumables without introducing toxic components or requiring removal before consumption.

Beyond traceability, substantial efforts have also been made to develop smart and intelligent food packaging technologies capable of real-time freshness monitoring. These packaging-integrated sensors typically monitor parameters such as pH, humidity, temperature, oxygen, carbon dioxide concentration, and microbial activity [88], [89]. Most reported approaches rely on colorimetric or electrochemical sensing mechanisms due to their straightforward readout. However, such approaches often suffer from limited sensitivity, poor long-term stability, and restricted quantitative precision. Furthermore, many of these

sensors remain attached to external packaging rather than being integrated directly into the food, contributing to packaging waste and limiting full edibility or biodegradability [90], [91], [92], [93].

In parallel, edible and biodegradable sensors have been explored extensively in the biomedical context. These include silk-based transient electronics [94], [95], edible thermistors for oral temperature monitoring [96], wireless biodegradable temperature sensors [97], glucose sensors for sweat analysis [98], sensors for other physiological parameters [99], and defrosting indicators for frozen foods [100]. Despite these advances, the direct translation of such approaches to food authentication, in-situ freshness monitoring, and labeling remains limited, and many are not explicitly designed to meet food-safety or ingestion requirements.

These limitations highlight the need for alternative optical tagging strategies that can simultaneously achieve high-capacity encoding, environmental sensitivity, and full edibility, motivating the exploration of photonic microcavities and edible lasers as next-generation solutions for secure food labeling and sensing.

1.5.2 Previous work on edible or partially edible lasers

Despite the significant development of microcavity-based lasers, only a limited number of studies have investigated microcavities fabricated from food-compatible materials. Most reported microcavity-based lasers rely on inorganic dielectrics, synthetic polymers, or semiconductor materials. As a result, the translation of microcavity laser technologies toward edible or ingestible materials has remained largely unexplored.

Only a small number of partially or fully edible laser approaches have been reported to date. For example, a single-mode biological DFB laser based on riboflavin-doped gelatin was demonstrated (see Figure 1.6a) [101]. This work showed that a vitamin-based dye can support stimulated emission and coherent lasing, highlighting the potential of edible fluorophores for photonic applications. However, the DFB gratings and substrate materials were non-edible, and the devices were not intended for direct contact with food or for applications such as tagging or sensing. In a related study, a freestanding single-mode DFB laser composed of riboflavin-doped silk fibroin isolated by a thin silver layer was demonstrated (Figure 1.6b) [102]. While this demonstration represented progress toward biologically derived lasers, the presence of a metallic isolation layer restricts its suitability for integration into food or consumable products.

Chlorophyll has also been explored as a naturally derived optical gain medium in microcavity lasers. In one approach, chlorophyll-containing microdroplets were generated and optically trapped on a superhydrophobic substrate, enabling lasing from spherical WGM microresonators (see Figure 1.6c) [57]. This work provided an important proof of principle for chlorophyll-based lasers; however, the reliance on trapped droplets and specialized substrates makes this configuration unsuitable for practical implementation as barcodes or sensors in consumable products. Subsequently, optofluidic WGM lasers based on chlorophyll were demonstrated using ultra-high-Q microcavities, as shown in Figure 1.6d [103]. By integrating chlorophyll into optofluidic resonator platforms, this study enabled a detailed investigation of chlorophyll lasing dynamics, including dual-band lasing behavior and concentration-dependent gain characteristics.

In addition, a fully edible random laser based on marine-derived materials has been reported [104]. While this work demonstrated the feasibility of coherent emission from entirely edible constituents, the inherently multimodal and spectrally broad emission of random lasers limits their suitability for applications requiring precise spectral encoding or high multiplexing capacity.

Protein-based microcavity lasers have also been investigated as biocompatible microlasers. For example, WGM microlasers fabricated from egg white doped with rhodamine B exploited the natural optical transparency and ability of egg white to form smooth microresonator geometries (see Figure 1.6e) [105].

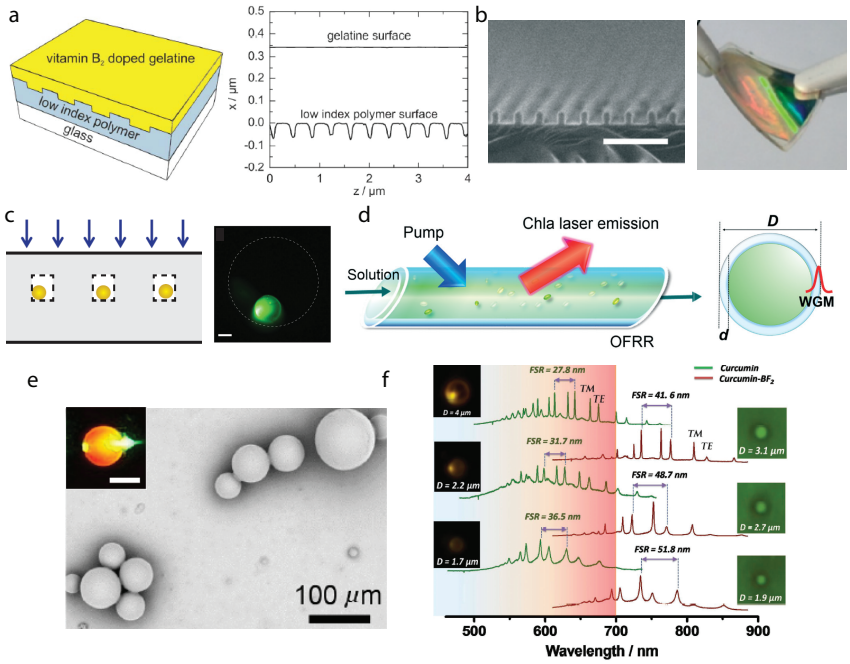


Figure 1.6: a) Schematic of a biological DFB laser based on riboflavin-doped gelatin, together with atomic force microscopy height profile profiles comparing different grating corrugation depths. b) Scanning electron microscopy (SEM) image of the side view of the photoresist grating designed by laser-interference-lithography (LIL) and diffraction colors under bending of the freestanding DFB laser. c) Illustration of vitamin-based microdroplets trapped in a polymer microwell and fluorescence image of a microsphere embedded within the microwell above lasing threshold (scale bar: 10 µm) d) Schematic of a chlorophyll laser based on an optofluidic ring resonator (OFRR). The right side shows the OFRR cross-section and the WGM circulating along the resonator (D = 80 µm; d= 2 µm). e) Optical image of a dye-doped goose egg-white microsphere; inset shows the microsphere under pulsed laser excitation. f) Emission spectra of curcumin- and modified-curcumin-based microspheres of different sizes; inset shows optical images of the corresponding microcavities. Image credits: a) Reproduced from Ref. [101] with permission from The Royal Society of Chemistry. b) Reproduced from Ref. [102] with permission from The Royal Society of Chemistry. c) Reproduced with permission from Ref. [57]. Copyright (2013) Wiley-VCH Verlag GmbH & Co. KGaA, Weinheim. d) Reproduced from Ref. [103] with permission from The Royal Society of Chemistry. e) Reproduced with permission from Ref. [105]. Copyright (2020) IOP Publishing Ltd. f) Reproduced with permission from Ref. [106]. Copyright (2016) Wiley-VCH Verlag GmbH & Co. KGaA, Weinheim.

Similarly, bovine serum albumin (BSA) has been used to form WGM microcavities capable of lasing [107]. In both cases, however, the gain media employed were not edible, and the microlasers were developed primarily as proof-of-concept biological resonators rather than for food-compatible or ingestible applications.

Beyond microlasers, curcumin-based microspheres have been demonstrated to support

WGM resonances in the visible and near-infrared range, as shown in Figure 1.6f [106]. Although this work highlighted the potential of naturally derived materials for photonic microcavities, the use of toxic solvents during fabrication limits their practical relevance for edible systems.

Overall, existing demonstrations of fully or partially edible microcavity lasers remain limited in scope and application. Most studies focus on fundamental lasing behavior or material feasibility rather than addressing applications such as food tagging, authentication, or sensing. Moreover, challenges related to scalability, integration, and practical readout strategies have generally not been addressed, leaving a clear gap that motivates the work presented in this thesis.

1.6 Goal of the Thesis

The primary objective of this PhD work is to develop fully edible photonic microcavities–operating both below and above the lasing threshold–that can function as optical barcodes, physical unclonable functions (PUFs), and sensors for food and pharmaceutical products, as conceptually illustrated in Figure 1.7. The specific goals of the thesis are as follows:

- To identify, characterize, and optimize edible gain materials, cavity materials, and supporting matrices, and to demonstrate, for the first time, completely edible microlasers based on both WGM and FP-cavity configurations
- To develop edible optical barcodes by embedding or dispersing edible microcavities directly within real food products, and to evaluate their long-term optical stability, including the ability to encode practical information such as expiration dates.
- To develop edible photonic sensors based on the environmental sensitivity of WGM resonators and responsive cavity materials, enabling detection of key parameters such as refractive index (e.g., sugar concentration), pH, temperature, and microbial growth.
- To address key practical limitations of microlasers–including the need for pulsed excitation (which is bulky and expensive), instability of liquid droplet cavities, and restricted applicability in high-refractive-index environments–by developing edible solid WGM microspheres that can be excited using CW lasers.
- To explore scalable and low-cost fabrication strategies for mass production of edible optical barcodes and sensors suitable for real-world applications.

Through this work, we establish a comprehensive framework for fully edible photonic barcodes and sensors, enabling new strategies for product authentication and freshness monitoring not only for food products, but also in pharmaceuticals, cosmetics, agriculture, and other high-value consumable products.

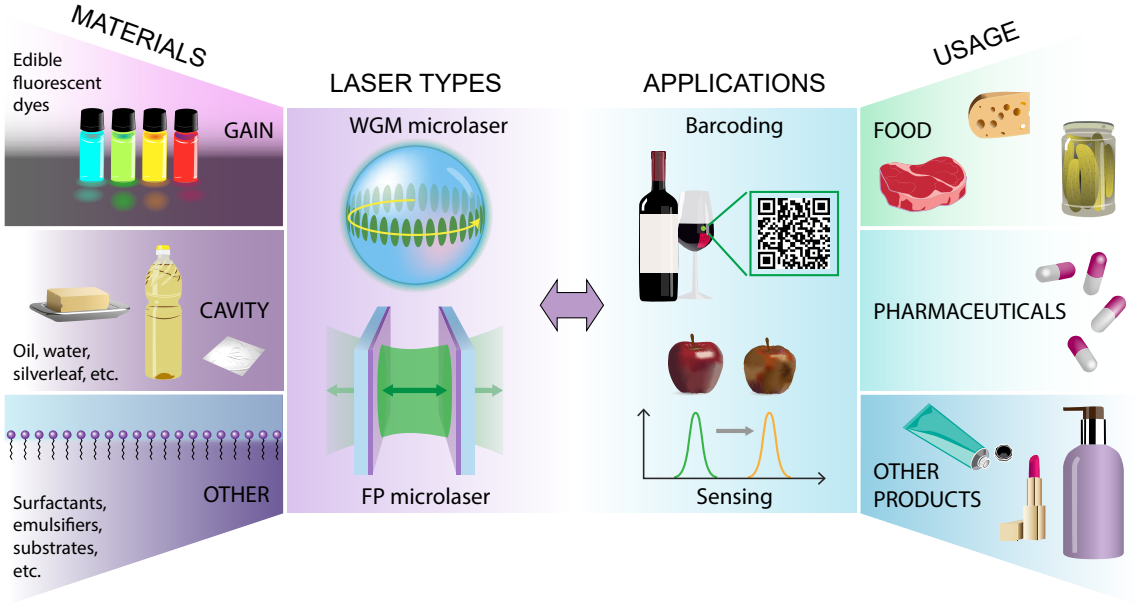


Figure 1.7: Conceptual overview of completely edible microlasers, from materials to applications. Edible components can serve as gain media (e.g., chlorophyll or riboflavin), optical cavities (e.g., oil-based droplets or solid microspheres), and other essential elements such as surfactants, silver leaf, and supporting matrices (e.g., gelatin or agarose). These materials enable different microlaser and microcavity configurations, including WGM and FP. The resulting emission can be exploited for optical barcoding and sensing in food and other consumable products.

Chapter 2

Theoretical Background

2.1 Optical Microcavities

Optical microcavities are fundamental components in modern photonics, capable of confining light within micrometer-scale volumes through reflection or total internal reflection. This strong confinement significantly enhances light-matter interactions, making microcavities essential platforms for investigating a wide range of optical phenomena, such as cavity quantum electrodynamics (QED) [108], nonlinear optics [109], and optical frequency comb generation [110]. In their simplest form, optical microcavities, also referred to as optical resonators, consist of two or more mirrors or reflective interfaces arranged such that light undergoes multiple reflections along a closed optical path. Optical resonance occurs when the round-trip optical path length equals an integer multiple l of the resonant wavelength. This condition, known as the resonant condition, can be expressed as:

$$nL_c = l\lambda_l, \tag{2.1}$$

where n is the effective refractive index, L_c is the round-trip cavity length, l is the longitudinal mode number, and λ_l is the resonant wavelength.

Optical microcavities are generally classified according to their geometry and light-confinement mechanism. Planar cavities, such as Fabry–Pérot (FP) cavities, confine light between two parallel mirrors. Circular cavities, including microspheres and microdisks, trap light through total internal reflection, giving rise to whispering gallery modes (WGMs). Distributed feedback (DFB) cavities achieve light confinement through periodic modulation of the refractive index, while random cavities depend on multiple scattering within disordered media to provide optical feedback. Each type of cavity exhibits distinct mode confinement and emission characteristics. Some examples are shown in Figure 2.1.

In this thesis, we specifically investigated WGM and FP cavities. The microspheres–including both liquid droplets and solid spheres–had diameters ranging from 40 µm to 100 µm and were dispersed in water, dilute sugar solutions, or, in some cases, embedded within hydrogel matrices. The microspheres consisted of either chlorophyll-doped oil droplets or chlorophyll-doped silica microspheres, both having a refractive index of approximately 1.46. Similarly, for the FP cavities, the optical cavity thickness ranged from 0.5 mm to 1 mm. These cavities were filled with a gain medium and incorporated edible silver mirrors, which provided optical feedback through reflection.

The wavelength spacing between two consecutive resonant modes is known as the free spectral range (FSR):

$$\mathrm{FSR} = \lambda_l - \lambda_{l-1}. \tag{2.2}$$

A large FSR is generally desirable because it allows resonant modes to be well separated in wavelength, making individual modes easier to distinguish. The FSR is inversely pro-

portional to the cavity size, meaning that smaller cavities exhibit larger mode spacing. Another important characteristic is the mode volume, which describes the spatial region occupied by the electromagnetic field of a particular resonant mode within the cavity. In WGM, the mode volume can range from several tens to several thousands of cubic micrometers, depending on the cavity size and refractive index contrast. A smaller mode volume results in a higher optical energy density, which is beneficial for enabling nonlinear optical effects and enabling strong light-matter interactions.

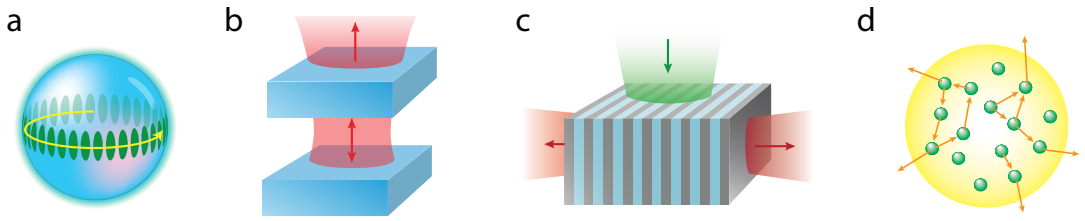


Figure 2.1: Schematics of different types of microcavities a) Whispering-gallery-mode (WGM), b) Fabry–Pérot (FP), c) Distributed-feedback (DFB), and d) Random laser.

2.1.1 Quality factor

The performance of an optical resonator is commonly characterized by its quality factor (Q-factor), which quantifies the cavity's ability to store light (optical energy). The Q-factor provides a measure of how spectrally sharp a resonance is relative to its central wavelength or frequency. It can also be defined as the ratio of the energy stored within the cavity to the energy lost per optical cycle:

$$Q = \omega \cdot \frac{\text{Stored energy}}{\text{Power loss}}, \tag{2.3}$$

where $\omega = \frac{2\pi c}{\lambda}$ is the angular optical frequency. The Q-factor is directly proportional to the photon lifetime or decay time of the cavity τ, which represents the average time a photon remains confined within the cavity, given by $Q = \omega\tau$. As a result, a higher Q-factor corresponds to a longer photon lifetime and lower optical losses. Different optical modes within the same cavity may experience different loss mechanisms, resulting in different Q-factors for each of the modes. For a passive cavity, the Q-factor is inversely proportional to the resonance linewidth $\Delta\lambda$ of a given optical mode. In this case, the Q-factor can be approximated as the ratio of the resonant wavelength to the full width half maximum (FWHM) of the spectral peak. This relationship is given by:

$$Q = 2\pi c\frac{\tau}{\lambda} = \frac{\lambda}{\Delta\lambda}. \tag{2.4}$$

Here, c is the speed of light, and $\Delta\lambda$ is the FWHM of the spectral peak at wavelength λ. WGMs, such as microspheres and microdisks, typically exhibit Q factors ranging from 10^3 to 10^9, depending on the material properties, fabrication quality, and surrounding environment [111], [112], [113]. In contrast, FP cavities generally exhibit lower Q factors, often on the order of 10^4 [114]. Due to high Q factors of WGM resonators, the corresponding resonance linewidths ($\Delta\lambda$) are often extremely narrow, sometimes approaching or falling below the resolution limit of the spectrometers. Consequently, precise experimental determination of the Q factors can be challenging. In our experiments, the measured

Q-factor for chlorophyll-doped droplets exceeded 9000, with the measurement limited by the spectrometer resolution.

From a theoretical perspective, the total Q-factor of a WGM microcavity arises from several independent loss mechanisms [115], which collectively determine the overall cavity performance:

$$\frac{1}{Q} = \sum_i \frac{1}{Q_i}, \tag{2.5}$$

where Q_i denotes the contribution from the following loss mechanisms: radiative loss (Q_{rad}), which originate from curvature-induced radiation leakage and are typically negligible for microspheres larger than 15 µm; surface scattering loss (Q_{ss}), which arise from surface roughness, inhomogeneities, or contaminants; and material absorption loss (Q_{mat}), which result from intrinsic absorption and scattering within the cavity material.

2.1.2 Purcell effect

The spontaneous emission of a two-level system depends not only on the intrinsic properties of the emitter but also on its surrounding electromagnetic environment. In free space (vacuum), the optical mode density is uniform and relatively low. In contrast, an optical cavity exhibits strongly frequency-dependent optical mode density, with significant enhancement at its resonance frequencies. This modification of spontaneous emission induced by the optical cavity is known as the Purcell effect. The resulting enhancement of emission is quantified by the Purcell factor:

$$P = \frac{3}{4\pi^2}\left(\frac{\lambda}{n}\right)^3 \cdot \frac{Q}{V}, \tag{2.6}$$

where λ is the resonance wavelength, n is the refractive index of the medium, Q is the quality factor, and V is the mode volume of the cavity. At resonance, spontaneous emission is enhanced and preferentially coupled into specific cavity modes, resulting in narrow and intense spectral peaks. In contrast, at non-resonant frequencies, the reduced mode density can suppress spontaneous emission, similar to the behavior observed in photonic bandgap materials, where emission at certain frequencies is entirely forbidden. It is important to note that the Purcell effect cannot be fully described using classical electrodynamics alone. While classical theory can predict the resonant modes of a cavity, it cannot explain the origin of spontaneous emission or its modification by vacuum field fluctuations. These effects require a cavity-QED description, which accounts for the interaction between quantized electromagnetic modes and the emitter [114].

In this thesis, the Purcell effect plays an essential role in interpreting the emission behavior of chlorophyll-doped silica microspheres under continuous-wave (CW) laser excitation. Even below the lasing threshold, narrow WGM peaks were observed in the emission spectra, which are attributed to Purcell-enhanced spontaneous emission into the cavity modes.

2.2 Whispering-Gallery Modes

WGM microcavities are typically microscale structures with a circular geometry, such as microspheres, microdisks, or microrings. To effectively confine the light within these structures, the cavity must possess an optically smooth surface to minimize the scattering losses, as well as a refractive index higher than that of the surrounding medium. Under these conditions, total internal reflection occurs at the cavity boundary, allowing light to circulate repeatedly along the perimeter of the cavity.

Resonance occurs when the optical path length of a single round trip equals an integer multiple of the wavelength ($L_c = l\lambda$), where L_c is the round-trip length and l corresponds to the azimuthal mode number. When this resonance condition is satisfied, the circulating light constructively interferes with itself, forming standing-wave patterns at specific resonant frequencies. These standing-wave patterns, known as eigenmodes, consist of a particular set of transverse and longitudinal cavity modes. The transverse modes are determined by the lateral dimension of the cavity, while the longitudinal modes depend on the optical length along the direction of light propagation. Each mode can be classified according to its polarization, being either transverse electric (TE) or transverse magnetic (TM).

2.2.1 Geometric approximation

For a spherical microcavity with radius R and effective refractive index n, the round-trip optical path length is $2\pi nR$. Since WGMs are strongly confined near the cavity boundary, the effective refractive index depends on both the refractive index of the cavity material (internal) and that of the surrounding medium (external). Under this approximation, the resonance condition can then be expressed as:

$$2\pi nR = l\lambda. \tag{2.7}$$

This geometric approximation provides a quick estimate of the resonance wavelengths, and it is particularly accurate for large polar mode numbers l, where light is tightly confined near the boundary. This approximation highlights how WGM resonances depend on the radius of the cavity and effective refractive index, but it does not account for polarization, field penetration into the surrounding medium, or the electromagnetic field distribution. To obtain exact resonance wavelengths and field distribution, Maxwell's equations must be solved with appropriate boundary conditions.

In this thesis, the FSR between two consecutive WGM resonances is used to determine the cavity diameter directly from the experimentally measured spectra. By averaging the FSR over multiple modes of the same polarization and using the known internal refractive index, a reliable estimate of the cavity diameter can be obtained.

$$FSR_i = \frac{1}{\lambda_{i-1}} - \frac{1}{\lambda_i}, \quad D = \frac{1}{\pi n_{\text{in}}\, FSR_{\text{avg}}}, \tag{2.8}$$

where D is the cavity diameter, n_{in} is the internal refractive index, and FSR_{avg} is the average free spectral range across multiple modes of the same polarization. Here, as a first approximation, we take $n_{\text{eff}} \approx n_{\text{in}}$.

2.2.2 Exact electromagnetic solution

In spherical geometries, exact solutions to Maxwell's equations yield the eigenmodes of the electromagnetic field under the appropriate boundary conditions at the cavity interface. Each mode is characterized by its polarization (TE or TM) and by the set of three mode numbers. The radial mode number q indicates the number of intensity maxima in the radial direction inside the cavity. The polar mode number l determines the number of wavelengths fitting along one circulation of the light around the cavity equator. The azimuthal mode number m defines the angular dependence of the mode within the spherical coordinate system.

For isotropic spherical microcavities, the resonance conditions for TE and TM modes are described by the following characteristic equations:

$$\frac{[n_r x_{nl} j_l(n_r x_{nl})]'}{j_l((n_r x_{nl})} = \frac{[x_{nl} h_l^{(1)}(x_{nl})]'}{h_l^{(1)}(x_{nl})}, \tag{2.9}$$

$$\frac{[n_r x_{nl} j_l(n_r x_{nl})]'}{n_r^{(2)} j_l((n_r x_{nl})} = \frac{[x_{nl} h_l^{(1)}(x_{nl})]'}{h_l^{(1)}(x_{nl})}, \tag{2.10}$$

where $n_r = n_{in}/n_{ext}$ is the relative refractive index between the resonator n_{in} and the surrounding medium n_{ext}. The x_{nl} is the size parameter, expressed as $x_{nl} = n_{ext} \cdot \omega_{nl} \cdot R/c$, where ω_{nl} is the angular eigenfrequency, R is the radius of the resonator, and c is the speed of light. The functions j_l and h_l denote the spherical Bessel and Hankel functions, respectively, and the primes indicate differentiation with respect to their arguments. Numerical solution of these characteristic equations gives the exact resonance frequencies and electromagnetic field distributions for both TE and TM modes. For each polar mode number (l), several solutions are possible, corresponding to different radial mode numbers (q). Each solution is associated with a complex eigenfrequency (ω_{nl}), reflecting the fact that resonant modes continuously dissipate energy through radiation into the surrounding medium.

Although these exact electromagnetic solutions provide fully accurate resonant conditions, they are computationally intensive. In many practical cases, particularly for high-Q microcavities with large polar mode numbers (typically on the order of 100) and low radial mode numbers, the optical field is strongly localized near the cavity boundary ($r = R$). In this regime, asymptotic approximations offer an efficient and accurate alternative by using analytic expansions of the Bessel functions. The resonant frequencies can then be expressed as an asymptotic series in powers of $(l/2)^{-1/3}$ [116], [117]:

$$n_{in} kR = l - \alpha_q \left(\frac{l}{2}\right)^{1/3} - \frac{\chi n_r}{\sqrt{n_r^2 - 1}} + \frac{3\alpha_q^2}{20}\left(\frac{l}{2}\right)^{-1/3} - \frac{\alpha_q n_r \chi (2\chi^2 - 3n_r^2)}{6(n_r^2 - 1)^{3/2}}\left(\frac{l}{2}\right)^{-2/3} + \mathcal{O}(l^{-1}), \tag{2.11}$$

where R is the cavity radius, k is the wavenumber, and χ depends on polarization: $\chi = 1$ for TE modes and $\chi = 1/n_r^2$ for TM modes. The polar mode number satisfies $l \gg 1$, and $q = 1, 2, 3, \ldots$ is the radial mode number; the approximation becomes less accurate for higher radial modes ($q > 1$). The parameter α_q denotes the q-th zero of the Airy function corresponding to the radial mode.

In this thesis, the asymptotic approximation is first employed to obtain an initial estimate of the external refractive index (n_{ext}) by comparing the calculated positions of TE and TM mode with the experimentally observed resonances. Once an optimal value of the external refractive index is identified, the resonance wavelengths are refined by numerically solving the characteristic equations (Eqs. (2.9) and (2.10); MATLAB code developed by Matevž Marinčič and Gregor Pirnat, whose contributions are gratefully acknowledged), which provides higher accuracy than the asymptotic model (Eq. (2.11)) alone. By combining this fitted refractive index with the cavity diameter extracted from the experimental FSR, the method enables simultaneous determination of both the cavity size and the refractive index of the surrounding medium.

2.3 Whispering-Gallery Mode Sensing Mechanisms

Even minute variations in the microsphere radius (well below the optical diffraction limit), cavity shape, or refractive index–either of the resonator itself or of the surrounding medium–can lead to measurable shifts in the spectral positions of WGM resonances. The resonance

wavelengths primarily depend on three key parameters: the cavity size, the refractive index of the resonator, and the refractive index of the surrounding medium. This strong dependence makes WGMs particularly attractive for label-free, real-time optical sensing applications.

Several sensing mechanisms have been demonstrated in WGM-based sensing, including resonance mode shifting [118], mode spitting [119], and linewidth broadening [120]. In this thesis, the resonance mode shifting mechanism is primarily employed to monitor changes in the refractive index of the surrounding medium.

2.3.1 Mode shifting

Relative spectral shifts ($\frac{\Delta\lambda}{\lambda}$) in WGM resonance arise from changes in the refractive index of resonator (Δn_{in}), surrounding medium (Δn_{ext}), and/or variation in the cavity radius ($\frac{\Delta R_0}{R_0}$). This relationship can be expressed as:

$$\frac{\Delta\lambda}{\lambda} = \frac{\Delta R_0}{R_0} + \frac{\Delta n_{ext}}{n_{ext}} \cdot F + \frac{\Delta n_{int}}{n_{int}} \cdot (1 - F), \tag{2.12}$$

where F is the sensitivity function, also referred to as the filing or field overlap factor. This parameter represents the fraction of the optical mode energy that extends into the surrounding medium. When $F = 0$, the optical field is almost entirely confined within the resonator, resulting in low sensitivity to external refractive index changes. Conversely, as F approaches 1, a significant portion of the optical field overlaps with the surrounding medium, leading to high sensitivity to variations in the refractive index of the surrounding medium. The value of F can be determined either from the exact solutions of the WGM characteristics equations (Eqs. (2.9) and (2.10)) or using the asymptotic approximation (Eq. (2.11)).

2.4 Fabry-Pérot Cavity

A FP-cavity is a one-dimensional optical resonator typically composed of two parallel mirrors separated by a uniform gain medium. When light enters the cavity, it undergoes multiple reflections between the mirrors, passing repeatedly through the gain medium where it is amplified by stimulated emission. The repeated back-and-forth propagation of lights between the two mirrors allows counter-propagating waves to interfere, producing either constructive or destructive interference. Constructive inference gives rise to standing waves when the distance between the mirrors L corresponds to an integer multiple of half-wavelengths, expressed as ($L = m \cdot \frac{\lambda}{2n}$), where m is the integer representing the longitudinal mode number and n is the effective refractive index. If the cavity is filled with a homogeneous gain medium, the effective refractive index can be taken as the refractive index of that material. As light propagates within the cavity, it accumulates a round-trip phase shift given by:

$$\delta = \frac{4\pi n L}{\lambda}. \tag{2.13}$$

For a symmetric FP cavity, in which both mirrors have identical reflectivity R, the spectral transmission T through the cavity can be described by the Airy formula as a function of round-trip phase shift δ:

$$T(\delta) = \frac{(1-R)^2}{(1-R)^2 + 4R\sin^2\left(\frac{\delta}{2}\right)}. \tag{2.14}$$

Transmission maxima (sharp peak) occur when δ equals integer multiples of 2π, corresponding to constructive interference, while transmission minima occur at odd multiples

of π, corresponding to destructive interference. As a result, the transmission spectrum exhibits a series of narrow, regularly spaced resonant peaks. The resonance wavelengths of an FP cavity can be tuned by varying the cavity length, changing the mirror curvature, or inserting material into the cavity. While the Airy expression accurately describes the transmission characteristics of an ideal FP cavity, in this thesis, it is employed primarily to illustrate the interference mechanism rather than for quantitative fitting. Due to uncertainties in facet reflectivity and scattering losses, the analysis is based mainly on the experimentally observed spacing between resonant modes.

The performance of an FP cavity is primarily characterized by two key parameters: the FSR and the Q factor. The FSR defines the spacing between adjacent longitudinal resonant modes, while the Q factor quantifies the spectral sharpness of each resonance. In this thesis, the FSR was determined directly from the measured emission spectra. The spacing between successive longitudinal modes was obtained in inverse-wavelength form:

$$FSR_i = \left| \frac{1}{\lambda_{i+1}} - \frac{1}{\lambda_i} \right|. \tag{2.15}$$

In this thesis, this relation is used as the primary method for determining the effective cavity thickness, with the cavity length obtained directly from the experimentally measured FSR:

$$L = \frac{1}{2n\, FSR_{\text{avg}}}, \tag{2.16}$$

where FSR_{avg} denotes the average spacing across all identified longitudinal modes. This method allows the cavity thickness to be accurately determined from the measured resonances.

Lasing occurs in an FP cavity when the optical gain compensates for all cavity losses. The threshold gain required to achieve this condition, which can be expressed as:

$$g_{th} = \frac{1}{2L} \ln\left(\frac{1}{R_1 R_2}\right), \tag{2.17}$$

where R_1 and R_2 are the reflectivities of the two mirrors. Lasing occurs once the material gain equals or exceeds this threshold, enabling continuous amplification of the resonant modes. Beyond the conventional mirror-based structure, FP-type resonators can also be realized where both the cavity and gain medium are combined within a single structure. Examples include elongated high-index organic single-crystalline waveguides, in which crystal facets serve as mirrors while the crystal itself acts as the gain medium [121], as well as semiconductor nanowires [122], which simultaneously function as both the optical cavity and the gain medium.

In addition to the longitudinal modes discussed above, FP cavities can in principle support both TE and TM polarization states. However, for a planar FP cavity operating at normal incidence, the Fresnel reflection coefficients for the TE and TM polarizations are identical, resulting in degenerate resonance frequencies for both polarization states. As a consequence, the TE and TM modes cannot be spectrally resolved and appear as a single set of longitudinal resonances in the measured emission spectrum. This is in contrast to WGM resonators (discussed in Section 2.2), where the curved cavity geometry imposes different boundary conditions on TE and TM modes, resulting in a measurable frequency splitting that appears as two distinct mode families in the emission spectrum.

2.5 Excitation of Optical Cavities

Optical microcavities can be excited using two general approaches: passive excitation and active excitation.

In passive excitation, an external light source is coupled into the cavity that does not contain a gain medium. The coupling mechanism depends strongly on the cavity geometry. For WGM resonators, light confinement relies on total internal reflection, which requires evanescent-field coupling. In this approach, the cavity is positioned within a submicron distance (typically less than 1 µm) from a tapered optical fiber or a prism to enable efficient evanescent coupling. This configuration allows highly efficient coupling or energy transfer into the cavity modes and enables the observation of ultra-high Q resonances. However, it also requires extremely precise alignment and mechanical stability. In contrast, passive excited FP cavities are often illuminated directly, since incident light can be coupled into the cavity through one of the partially transmissive mirrors. While the alignment requirements are simpler than for WGM resonators, achieving high Q factors typically requires mirrors with high reflectivity.

In active excitation, the cavity either contains or is doped with a fluorescent gain medium, which greatly simplifies the excitation process. In this method, a free-space laser beam at a shorter wavelength is focused onto the edge or the active region of the doped WGM resonator. The gain medium absorbs excitation light and emits fluorescence at longer wavelengths. A fraction of this emitted light is trapped within the cavity modes, primarily due to the Purcell effect, resulting in dominant spectral peaks corresponding to the cavity resonance. This excitation approach is particularly advantageous for practical applications, where moderately high Q factors are sufficient. Active FP cavities operate on a similar principle, with the cavity filled with a fluorescent gain medium and optically excited through one of the mirrors. The emitted light undergoes multiple reflections within the cavity, resulting in longitudinal resonance modes. Importantly, when the pump intensity exceeds the threshold for stimulated emission, both WGM and FP cavities containing gain material can operate in the lasing regime; this transition from fluorescence to lasing is described in the following sections.

In this thesis, both WGMs and FP cavities are investigated primarily in their active configuration. The cavities are excited using either a tunable pulsed laser or a continuous-wave (CW) laser (for excitation of the WGMs below the lasing threshold).

2.6 Properties and Characteristics of Lasers

A laser is a unique light source characterized by high temporal and spatial coherence, arising from the process of stimulated emission. The term LASER stands for Light Amplification by Stimulated Emission of Radiation. A typical laser consists of a gain medium–a material capable of amplifying light, enclosed within an optical resonator formed by reflective boundaries. The resonator forces the light to pass repeatedly through the gain medium, enhancing amplification and enabling the generation of coherent, spectrally narrow, and directional output.

In microcavity lasers, such as WGMs and FP resonators, the small cavity dimensions and high Q-factors significantly enhance the light-matter interaction. This enhancement can reduce the lasing threshold and enable lasing even in gain media with relatively modest fluorescence quantum yields.

2.6.1 Light-matter interaction

Light interacts with matter primarily through absorption, spontaneous emission, and stimulated emission. When a photon with energy $h\nu$ equal to the energy difference between two electronic states interacts with an atom or molecule in its ground state $|1\rangle$ (energy E_1), it can be absorbed, exciting it to a higher energy state $|2\rangle$ (energy E_2), where $E_2 - E_1 = h\nu$.

After a typical lifetime of approximately 10 ns, the excited atom relaxes back to ground state via spontaneous emission, emitting a photon with random phase, direction, and polarization. This process produces fluorescence. In contrast, stimulated emission occurs when an incident photon of energy $h\nu$ induces an excited atom or molecule to return to the lower energy state while emitting a second photon that is identical in energy, phase, direction, and polarization to the incident photon. This process results in coherent amplification of light.

The coherent amplification process is the key mechanism for laser action, which was first introduced by Einstein through the A and B coefficients, which quantify the probabilities of spontaneous emission, absorption, and stimulated emission. The rate equations can be expressed as:

$$\frac{dn_1}{dt} = -B_{12}n_1u(\nu), \tag{2.18}$$

$$\frac{dn_2}{dt} = -A_{21}n_2, \tag{2.19}$$

$$\frac{dn_2}{dt} = -B_{21}n_2u(\nu), \tag{2.20}$$

where n_1 and n_2 are the population of the lower ($|1\rangle$) and upper energy levels, respectively; A_{21}, B_{12}, and B_{21} are the Einstein coefficients for spontaneous emission, absorption, and stimulated emission; and $u(\nu)$ is the spectral energy density. The overall rate of change of the excited-state population is given by:

$$\frac{dn_2}{dt} = B_{12}n_1u(v) - A_{21}n_2 - B_{21}n_2u(\nu)\cdot \tag{2.21}$$

At thermal equilibrium, the ratio of populations between the two energy levels follows the Boltzmann distribution:

$$\frac{N_2}{N_1} = \exp\left(\frac{-E_2 + E_1}{k_BT}\right)\cdot \tag{2.22}$$

At absolute zero, almost all electrons occupy the lower energy level, while at infinite temperature, the populations are equally distributed between both levels. This fundamental limitation implies that external pumping is required to achieve population inversion, a necessary condition for lasing.

2.6.2 Population inversion and optical gain

For lasing, population inversion ($N_2 > N_1$) must be achieved so that stimulated emission dominates absorption. In a simple two-level system, population inversion is not practically achievable because absorption and emission occur with equal probabilities. Therefore, at least a three- or four-level system is required. In a three-level system, electrons are pumped from the ground state $|1\rangle$ to a higher energy state $|3\rangle$ and then rapidly relax to a metastable intermediate state $|2\rangle$. If the relaxation from $|3\rangle$ to $|2\rangle$ is much faster than from $|2\rangle$ to $|1\rangle$, a population inversion between $|2\rangle$ and $|1\rangle$ can be achieved. Similarly, in a four-level system, inversion occurs between two excited states, making the lasing process more efficient. Once population inversion is achieved, photons generated by stimulated emission are amplified during each round trip through the gain medium, while the optical cavity enforces feedback, optical mode selection, and coherence.

In this thesis, edible gain media such as chlorophyll and riboflavin are employed. Both dyes absorb strongly around 450 nm and emit near 680 nm (chlorophyll) and 550 nm (riboflavin). In solution, their effective absorption coefficients are approximately $\alpha \sim$

10^4 cm^{-1} for chlorophyll and approximately $\alpha \sim 8 \times 10^3$ cm^{-1} for riboflavin at millimolar concentrations, enabling efficient absorption. In this work, dye concentrations of approximately 2 mM for chlorophyll and 3 mM for riboflavin were selected to balance absorption efficiency with reabsorption effects and concentration-dependent quenching effects.

The fluorescence quantum yields of chlorophyll (approximately 0.3) and riboflavin (approximately 0.27) indicate that a substantial fraction of absorbed photons is re-emitted radiatively. Although these values are less compared to conventional lasing dyes, the strong optical confinement and feedback provided by microcavity resonators significantly enhance the effective light–matter interaction. Photons generated within the gain medium undergo multiple round-trip through the cavity, increasing the effective interaction length and amplification per photon. As a result, lasing or pronounced cavity-enhanced emission can be attained even in gain media that would not lase in bulk configurations.

The cavity geometry and material properties determine the optical mode structure, FSR, and feedback, while the gain medium properties, such as absorption coefficient, concentration, emission spectrum, and quantum yield, determine the achievable optical gain.

2.7 Principles of Optical Barcoding Based on Microcavities

Optical microcavities can function as optical barcodes by encoding information into their emission characteristics, such as spectral position, linewidth, polarization, and spatial mode pattern. These characteristics are determined by the cavity geometry, refractive index, and properties of the gain material. The primary objective of microcavity-based barcoding is to generate a large number of unique and distinguishable spectral signatures, referred to as optical microbarcodes. Microcavities are particularly ideal candidates for this because they significantly modify and control the emission properties of the embedded fluorescent material.

Typical fluorescent materials exhibit broad emission spectra, with FWHM on the order of tens of nanometers (i.e., 50 nm, see Figure 2.2a). In contrast, microcavities can produce extremely narrow emission with linewidths below 0.1 nm, as shown in Figure 2.2b. This drastic reduction in emission linewidths enables a corresponding increase in the number of distinguishable spectra (optical barcodes). Beyond linewidth narrowing, microcavities also alter several other key properties of the emitted light. For example, in the case of lasing, the emitted light intensity exhibits a highly nonlinear dependence on the input energy, characterized by a well-defined lasing threshold. Both below and above the lasing threshold, the emitted light can be strongly polarized and confined to well-defined spatial modes, which are determined by the cavity geometry. These modes can be observed as a particular intensity pattern and directional emission, in contrast to the diffuse and unpolarized emission typical of conventional fluorescence. These properties, including ultra-narrow linewidths, threshold behavior, polarization control, and distinct mode structure makes optical microcavities a powerful platform for optical barcoding and sensing applications.

2.7.1 Encoding using single- and multi-mode emission

Microcavity emission can be encoded using a variety of spectral and physical parameters, including the emission wavelength of single or multiple spectral lines, linewidth, emission intensity, cavity size, and lasing threshold. Optical barcodes can be random, arising from inherent fabrication variation in microcavities, or predefined, where the encoding parameters are controlled during fabrication.

In single-mode emission, the central emission wavelength alone serves as the barcode. This is typically observed in small WGM cavities with a large FSR, where only a single

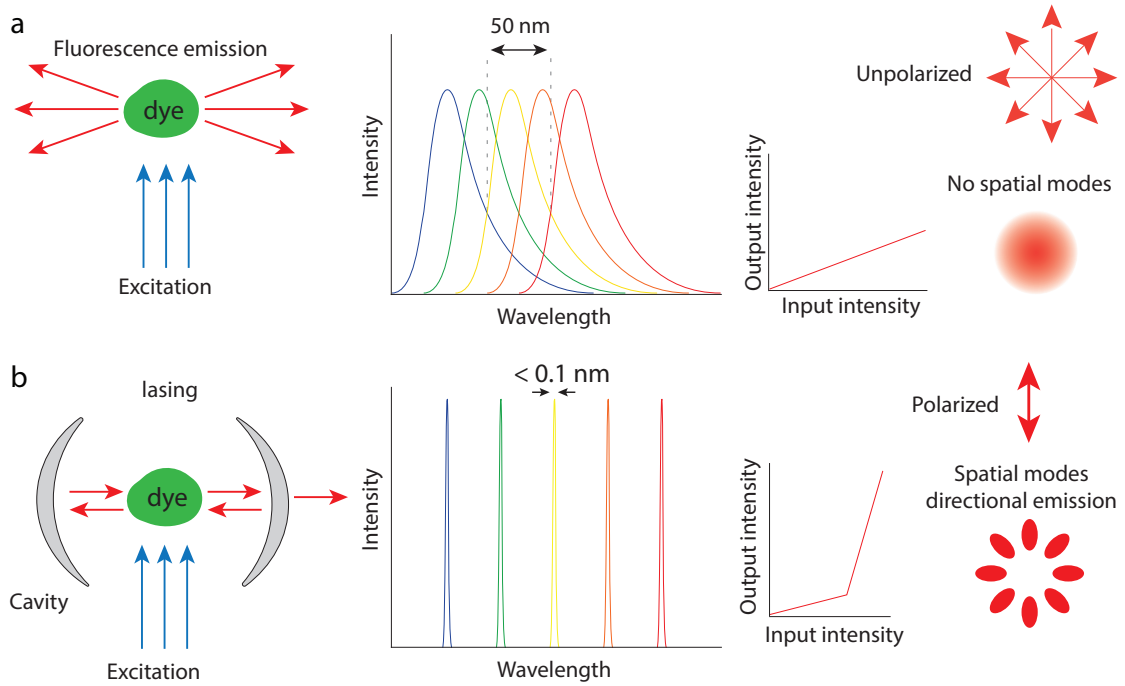


Figure 2.2: Comparison of emission properties. a) Spontaneous fluorescence emission. b) Emission from a microcavity or microlaser. The main differences include the emission spectrum width, output nonlinearity, polarization, and the presence of spatial modes.

mode falls within the gain bandwidth. DFB lasers similarly exhibit single-mode emission, in which the emission wavelength corresponds directly to the grating periodicity, as shown in Figure 2.3a.

In multi-mode emission, multiple spectral lines provide unique identifiers in several possible ways. The wavelength, linewidth, and intensity of each spectral peak can all be used as independent barcode elements. For example, in random lasers, where optical feedback arises from structural disorder, the spectral peaks are relatively independent of each other, allowing both their spectral position and relative intensities to serve as barcode features (see Figure 2.3b). This enables a barcoding strategy conceptually similar to conventional linear barcodes, where the positions of the bars correspond to the central wavelengths of the spectral peaks, and the bar widths correspond to their intensities.

In contrast, in many multi-mode cavities, the resonant modes are not independent of each other. In a simple FP cavity, the modes are equally spaced in wavelength, and the positions of all spectral peaks are determined by a single parameter: the optical length of the cavity. Thus, the FSR becomes the defining barcode feature, as schematically shown in Figure 2.3c for two FP cavities of different lengths.

In addition, a characteristic FSR is also observed in multi-mode WGM microcavities, which depends on the cavity diameter and refractive index. In this case, the resonant spectrum arises from light circulating along the curved cavity boundary via total internal reflection, rather than from linear back-and-forth propagation as in FP resonators (Figure 2.3c). Consequently, microcavities of different sizes exhibit distinct sets of resonant peaks with different FSRs, as illustrated in Figure 2.3d. Therefore, in WGM-based barcoding, the physical size of the cavity (and the resulting FSR) serves as the primary encoding parameter.

In this thesis, multi-mode WGM microcavities are employed as optical barcodes both

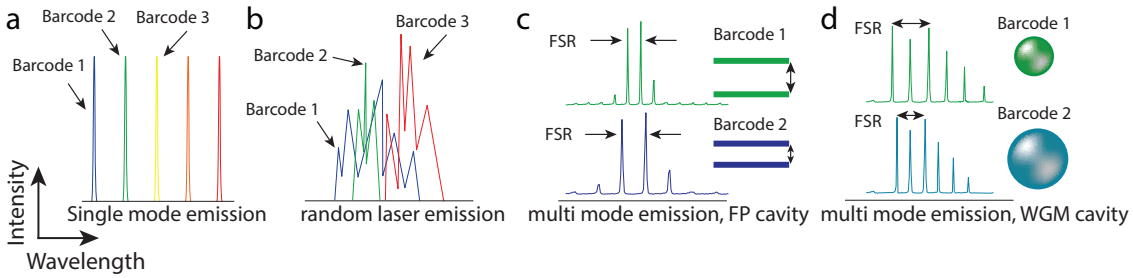


Figure 2.3: Schematic illustration of single- and multi-mode laser emission represented as barcodes. a) Single-mode emission from a DFB laser, tunable via the grating periodicity. b) Emission from a random laser showing irregular spectral modes. c) Multi-mode emission from FP cavities with different cavity lengths, exhibiting distinct FSR. d) Multi-mode emission from WGM microcavities of different sizes, also showing characteristic FSR spacing.

below and above the lasing threshold, with the physical size of the cavity serving as the primary encoding parameter. In the following section, we focus specifically on barcoding using WGMs and discuss how their spectral characteristics can be exploited to encode and decode information.

2.7.2 Random versus predefined WGM barcodes

Most microcavity-based barcodes reported to date have been generated randomly, without intentionally encoding specific information [38], [39], [40]. For example, commercially available polydisperse fluorescent polystyrene beads (with a mean diameter 8.8 µm and a coefficient of variation of 18%) exhibit small variations in their spectral resonances due to size polydispersity, thereby producing inherently unique optical barcodes. This intrinsic randomness can often be advantageous, as it enables the generation of complex and practically non-reproducible barcodes.

However, when there is a requirement to encode specific information, predefined information, similar to conventional macroscopic barcodes, the fabrication process must be precisely controlled. To date, only a limited number of studies have demonstrated predefined WGM barcodes [111], [123]. In this thesis, we report predefined WGM microcavity barcodes, in which the encoded information is directly determined by the cavity diameter. The information capacity (number of bits) of a microcavity barcode is given by $\log_2(N)$, where N is the number of unique barcodes. Notably, even a large number of distinct spectral signatures corresponds to a relatively modest amount of encoded information. For example, 1,000 unique spectra correspond to only about ~ 10 bits of information. Consequently, multiplexing strategies are often required to significantly enhance the encoding capacity.

2.7.3 Multiplexing

Multiplexing enhances the encoding capacity by combining multiple independent cavity properties, such as cavity size, gain material, polarization, or mode structure. For example, using multiple fluorescent dyes with distinct emission spectra, in combination with different cavity sizes, enables the generation of multi-dimensional optical barcodes with substantially increased uniqueness.

One straightforward multiplexing strategy is to combine multiple microcavities into a

single barcode (as shown in Figure 2.4a). If each barcode consists of m microcavities, and each microcavity can exist in one of D distinct states (such as different resonance wavelengths or cavity sizes), the total number of unique barcodes is given by the number of possible combinations:

$$N = \binom{D}{m} = \frac{D!}{m!(D-m)!}. \tag{2.23}$$

Here it is assumed that the order of microcavities within a barcode is not important– only their identity matters. This combinatorial encoding scales very favorably with m: for a fixed number of distinguishable states D, increasing the number of microcavities per barcode rapidly expands the encoding capacity. For instance, using $m = 5$ microcavities per barcode drawn from $D = 100$ possible states yields approximately 7×10^7 unique barcodes. Achieving this in practice requires that each microcavity state be reliably distinguishable from its emission spectrum, which places a direct requirement on the measurement precision of the spectral characterization method.

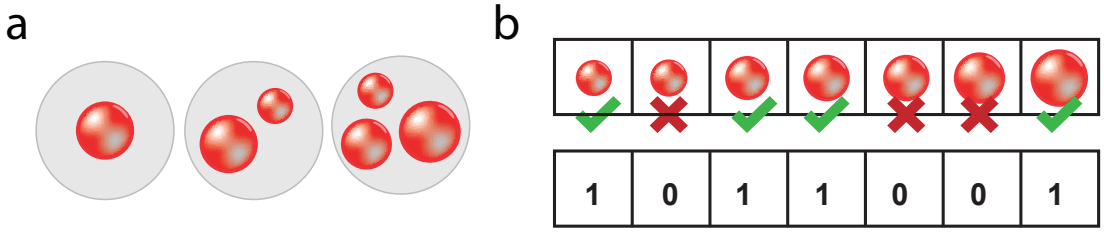


Figure 2.4: Principles of multiplexing. a) A single barcode can consist of multiple microcavities, greatly increasing the number of possible unique barcodes. b) Barcoding principle in which any number of unique states can be selected to create a single barcode. Unlike (a), where the barcode is defined by a fixed number of microcavities, here the barcode is encoded by the presence ("1") or absence ("0") of each state.

Another commonly employed multiplexing strategy involves binary encoding, in which information is represented by the presence ('1') or absence ('0') of specific microcavity states, such as particular cavity size, resonance wavelength, or lasing threshold (see Figure 2.4b). In this approach, the total number of microcavities is not fixed, and the barcode corresponds to a binary sequence defined by the available cavity states. The total number of unique barcodes K can be calculated as:

$$K = 2^D, \tag{2.24}$$

where D is the number of distinguishable microcavity states. The total number of unique barcodes increases exponentially with the number of distinguishable states. For example, 20 distinct microsphere sizes allow for the generation of approximately 10^6 unique barcodes. In this thesis, 14 distinct cavity sizes are employed to generate unique WGM-based optical barcodes using this binary encoding approach.

2.8 Multimodal Application of Microcavities: Barcoding and Sensing

Microcavities are valuable not only as optical barcodes but also as sensitive optical sensors capable of detecting a wide range of parameters, including temperature, humidity, pH, and the presence of specific microorganisms. In WGM microcavities, both the cavity size

and the refractive index of the surrounding medium can be extracted from the emission spectrum, both above and below the lasing threshold. This capability allows a microcavity to function simultaneously as a unique barcode and as a sensor, with both types of information obtained from a single optical measurement.

Similarly, FP cavities can function as sensors or indicators by monitoring changes in the optical cavity length, which manifest as shifts in the FSR of the resonance modes. In WGM microcavities, sensing is most commonly observed as shifts in the resonance wavelength, which primarily reflect relative changes in the local refractive index rather than absolute refractive index values.

To achieve selective detection of specific analytes or stimuli, the microcavity can be externally coated with, or fabricated from, responsive materials such as a polymer or other smart material. These materials interact with the surrounding environment, leading to measurable resonance shifts and enabling selective detection. FP cavities can be designed similarly by incorporating responsive materials into the cavity structure. Such materials may swell, contract, or deform in response to external stimuli, resulting in detectable shifts in resonance or preventing the cavity from fulfilling the resonance conditions.

In this thesis, we demonstrate the multimodal functionality of WGM microcavities across several configurations, highlighting their potential as both optical barcodes and sensors. Detailed experimental methodologies and results are presented in the following chapters.

Chapter 3

Materials and Methods

3.1 Components of Edible Lasers

As discussed in the previous chapter, a laser consists of three essential components: a gain medium, an optical cavity, and an excitation source. This chapter describes the materials and experimental procedures used to realize these components using entirely edible substances. This constitutes a crucial part of the thesis, as it focuses on identifying and utilizing suitable edible materials that can function as the core elements of edible lasers in several configurations. In all experiments, optical pumping using an external laser source was employed to excite the edible gain medium.

The initial search for suitable edible gain materials was initiated by Dr. Maruša Mur, whose contributions are gratefully acknowledged. In addition, thanks are extended to Ana Krišelj for preparing the solutions and samples that were crucial for the design of the microcavities and for carrying out the sensing experiments.

3.1.1 Edible gain media

In principle, any edible material exhibiting fluorescence may serve as a gain medium. In this thesis, the selection was restricted to naturally occurring edible substances and approved food additives that are safe for human consumption and were used without any chemical modification. Initially, a broad range of edible fluorescent materials was investigated (see Table 3.1), including curcumin, quinine, and several approved food colorants such as E102 (tartrazine, yellow), E122 (carmoisine, red), and E132 (indigo carmine, blue), as well as natural pigments including saffron, and bixin (annatto). In addition, riboflavin, riboflavin sodium phosphate, and chlorophyll-A were evaluated as potential edible gain media. These candidates were selected because they are inexpensive, widely available, and commonly used in food products. The initial screening revealed that only materials with a fluorescence quantum yield (QY) exceeding approximately 0.2 were suitable for use as gain media. Furthermore, some materials, such as quinine, were excluded due to their poor solubility in edible solvents such as water and vegetable oils. Among the tested materials, riboflavin ($QY \approx 0.27$), riboflavin sodium phosphate ($QY \approx 0.23$), chlorophyll-A ($QY \approx 0.30$), and bixin demonstrated both sufficient fluorescence efficiency and good compatibility with edible solvents. These materials were therefore selected for further investigation and used as gain media in the demonstration of edible lasers in various configurations.

The selected edible gain media were classified according to their solubility. Riboflavin (vitamin B2) and riboflavin sodium phosphate are soluble in water, whereas chlorophyll-A (Sigma-Aldrich) and bixin (Sigma-Aldrich) are soluble in vegetable oils. Although riboflavin exhibits limited solubility in water, it remains suitable as a gain medium due to

its relatively high fluorescence QY [124]. Its solubility can be increased by adjusting the pH of the solvent; however, such modifications may reduce fluorescence efficiency. In contrast, riboflavin sodium phosphate is highly soluble in water and therefore more convenient for aqueous gain media preparation.

Table 3.1: List of the edible dyes that we investigated as gain media for different laser configurations.

Edible gain medium	Solvents
Quinine	Water
Nor bixin (annatto)	
Saffron	
E122 Red	
E102 Yellow	
E132 Blue	
Curcumin	
Chlorophyllin	
Riboflavin (vitamin B2)	
Riboflavin sodium phosphate	
NADH	Ethanol
Chlorophyll-A	
Chlorophyll extracted from spinach	
Bixin	

For aqueous gain media, riboflavin and riboflavin sodium phosphate were dissolved in a mixture of water-glycerol (80:20 v/v) at final concentrations of 3 mM and 5 mM, respectively. Glycerol was added to reduce the rate of evaporation. The prepared solutions were stored in light-protected containers until use.

Chlorophyll-A and bixin were not readily soluble directly in vegetable oil but were easily dissolved in ethanol. Therefore, each dye was first dissolved in ethanol and subsequently mixed with vegetable oil. The mixtures were stirred continuously at 50 °C overnight to ensure complete evaporation of ethanol, resulting in final dye concentrations of 2 mM for chlorophyll-A and 4 mM for bixin. The prepared oil-based gain media were stored under dark conditions to minimize photodegradation. Because commercially available chlorophyll-A is relatively expensive, alternative and more cost-effective sources were explored. It was found that certain olive oils naturally contain sufficient chlorophyll to function directly as a gain medium without further modification. In addition, chlorophyll extracted from fresh spinach leaves was successfully used in several lasing demonstrations.

3.1.1.1 Chlorophyll extraction from spinach leaves

Fresh spinach leaves were obtained from a local supermarket for chlorophyll extraction. Approximately 2 g of the spinach leaves were thoroughly washed with hot water, and the main veins were removed to facilitate pigment release. The de-veined leaves were then ground in a mortar with 1 g anhydrous sodium sulfate and 4 mL acetone until a smooth paste was formed (see Figure 3.1a and b). The paste was transferred to a 50 mL centrifuge tube, to which 4 mL hexane was added. The mixture was gently shaken, followed by the addition of 4 mL of distilled water. After gentle mixing and occasionally venting, the sample was centrifuged until a clear phase separation occurred (as shown in Figure 3.1c). A dark green organic layer (top) containing chlorophyll formed above an aqueous layer (bottom) consisting primarily of acetone and water. The organic layer was carefully transferred to

a clean centrifuge tube. To maximize extraction yield, repeated extraction was performed adding 2 mL hexane to the remaining aqueous phase, followed by shaking, centrifugation and collection of the top organic layer, which was combined with the organic extract collected previously.

To remove residual moisture and impurities, 1 g anhydrous sodium sulfate was added to the organic phase and left to stand for 10 min. The solvent (hexane) was then evaporated at approximately 40 °C under reduced pressure using a rotary evaporator (see Figure 3.1d). The resulting chlorophyll residue was dissolved in ethanol and subsequently mixed with vegetable oil to prepare the final gain medium used in lasing experiments.

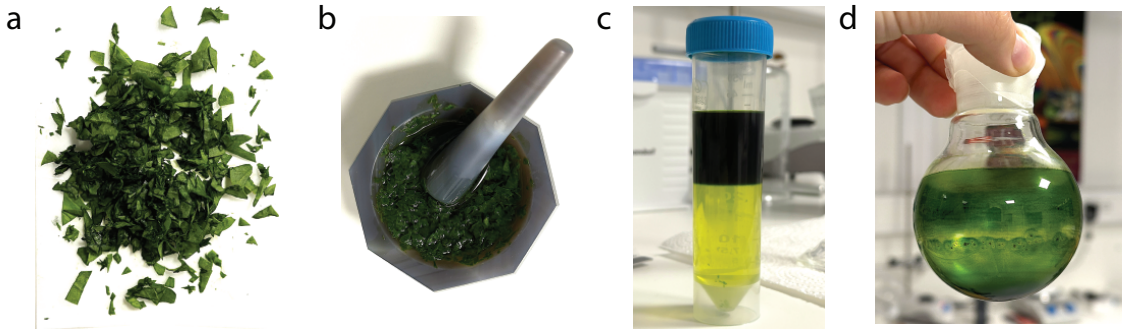


Figure 3.1: Stepwise extraction of chlorophyll from spinach: a) deveining, b) grinding, c) phase separation, and d) solvent evaporation to obtain the chlorophyll extract (photo credit: Ana Krišelj).

3.1.2 Edible optical cavity

Following the preparation of suitable edible gain media, the next essential component of the laser system was the optical cavity or resonator. The choice of the cavity material was determined by the specific laser configuration and its intended function. In general, the cavity materials were required to be optically transparent to minimize losses such as scattering and absorption. In certain configurations, a higher refractive index was desirable to ensure strong optical confinement, whereas in other cases, reflective materials were required to form mirror-based resonators (FP-cavities).

To develop edible optical resonators, a range of food-grade materials were investigated for their optical properties (see Table 3.2). Transparent liquids such as various vegetable oils, including sunflower oil and cinnamon oil, were used as droplet resonators. These materials form smooth liquid-liquid interfaces and possess a refractive index higher than that of water, enabling efficient total internal reflection and supporting WGM resonances. Similarly, melted butter was used to generate liquid droplets, which, upon cooling and solidification, formed solid or semi-solid microcavities suitable for optical confinement.

For mirror-based resonators (FP-cavities), thin silver leaves, commonly used as decorative edible foils, were employed as reflective layers forming both mirrors of the cavity. This approach enabled the construction of partially or fully reflective cavities without introducing non-edible materials. To provide mechanical stability and maintain mirror alignment, thin films of agar were used as supporting layers for the silver leaves and the overall cavity structure. In addition to the primary cavity, several other edible substances, including agarose, chitosan, Tween 20, and gelatin, were employed as non-optical components. These materials served to provide mechanical support, encapsulation, or stabilization of droplet

emulsions, ensuring that the cavity geometry remained stable during experiments. In some configurations, they also enabled responsiveness to external parameters such as temperature, pH, or microbial growth, thereby extending the functionality of the edible cavities beyond lasing alone.

Table 3.2: List of the edible materials that we investigated as optical cavities for different laser configurations. Not all evaluated materials are discussed further in this thesis, as only a subset was selected for the demonstrations presented.

Edible materials for optical cavity
Sunflower oil
Olive oil
Melted butter
Cinnamon oil
Water-glycerol
Shellac (E904)
Egg white
Thin silver leaf

3.2 Fabrication of Microcavities and Their Applications

In this thesis, two main configurations of edible lasers (WGM and FP) were demonstrated. This section describes the fabrication methods used to realize optical microcavities using edible gain media introduced in the previous section.

3.2.1 Whispering-gallery modes (WGMs)

3.2.1.1 Oil-in-water emulsion

Polydisperse WGM microcavities were produced using a standard oil-in-water emulsion technique. In this method, chlorophyll-doped sunflower oil served as the dispersed (droplet) phase, while deionized water served as the continuous phase. To stabilize the emulsion, 1 % polyoxyethylene (20) sorbitan monolaurate (Tween 20, Sigma Aldrich) was dissolved in the aqueous phase as a surfactant. Subsequently, 1 % of the chlorophyll-doped sunflower oil was added to the continuous phase, and the mixture was vigorously shaken to generate polydisperse oil droplets (see Figure 3.2a). The resulting emulsion contained oil droplets with diameters ranging from a few micrometers to several tens of micrometers, suitable for supporting WGM modes. Bixin-doped sunflower droplets were produced similarly by replacing the chlorophyll with bixin.

Solid WGM microcavities were produced using a similar procedure, with chlorophyll-doped melted butter replacing sunflower oil as the droplet phase. Following emulsification, the emulsion was cooled to approximately 8 °C, causing the droplets to solidify. The resulting semi-solid microcavities were stable and suitable for demonstrating WGM-based sensing applications.

3.2.1.2 Spraying on hydrophobic/superhydrophobic surfaces

While the oil-in-water emulsion method provides a simple and effective way to produce polydisperse WGM microcavities for testing edible gain media. However, it is inherently

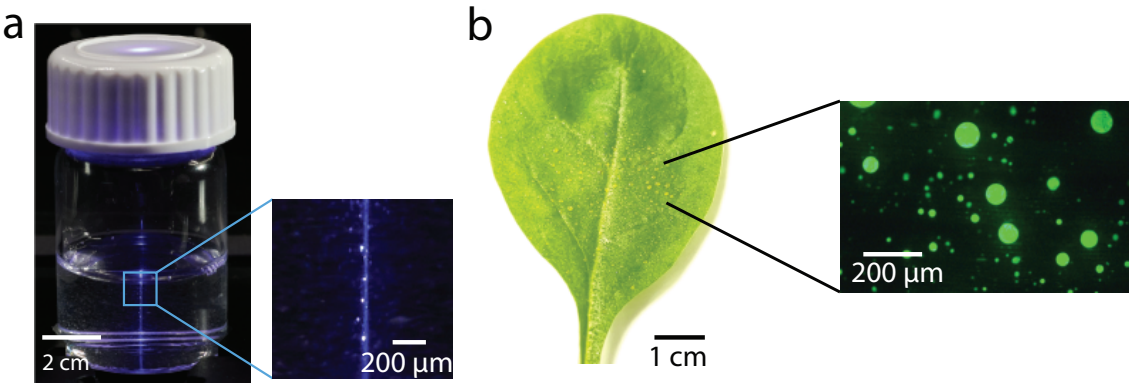


Figure 3.2: a) Chlorophyll-doped oil droplets inside water under the illumination of a blue pulsed laser. b) Riboflavin-doped water-glycerol solution was sprayed onto a spinach leaf, and the fluorescence of the resulting droplets was imaged.

limited to oil-soluble gain media. To extend WGM microcavities fabrication to water-soluble gain media, edible hydrophobic surfaces were employed to induce droplet formation.

Considering both edibility and availability, fresh spinach leaves were used as hydrophobic substrates. Aqueous solutions of riboflavin and riboflavin sodium phosphate, prepared in a water-glycerol mixture, were sprayed onto the leaf surface. Due to surface tension and the hydrophobic nature of the leaf, the sprayed liquid formed nearly spherical droplets (see Figure 3.2b) that functioned as WGM microcavities. This approach demonstrates a simple and effective proof of concept for producing WGM microcavities using water-soluble gain media. However, this method is not suitable for large-scale fabrication or the use of these microcavities for practical application, since the droplets are not mechanically fixed and gradually evaporate over time, leading to changes in cavity size, shape, and optical performance.

3.2.1.3 Microfluidics

Monodisperse WGM microcavities were produced using a commercially available droplet generator (hydrophilized Fluidic 440, Chipshop). Each microfluidic chip consisted of eight independent single-cross channels with a flow focusing geometry and nozzle sizes ranging from 50 µm to 80 µm. Each channel contained two inlets–one for the dispersed (droplet) phase and one for the continuous phase–and a single outlet for droplet collection (as shown in Figure 3.3a and b. An Elveflow OB1 MKIII+ pressure controller was used to precisely regulate the flow at both inlets. The pressure controller provided three independently adjustable pressure channels with operating ranges of 0 mbar to 200 mbar, 0 mbar to 2000 mbar, and −950 mbar to 1000 mbar, respectively. Prior to each experiment, the microfluidic channels were flushed at sufficiently high pressure to remove air bubbles and clear any potential blockages within the channels. I gratefully acknowledge Rok Štanc (Institute of Biophysics, Faculty of Medicine, University of Ljubljana, Slovenia) for his support and guidance during the initial microfluidics experiments.

For droplet generation, the dispersed-phase reservoir containing chlorophyll-doped sunflower oil was connected to one inlet, while the continuous phase reservoir containing a water-surfactant solution was connected to the second inlet. The outlet was connected to an empty collection reservoir (see Figure 3.3b). By selecting channels with different nozzle sizes and adjusting the inlet pressures, 14 distinct samples of monodisperse chlorophyll-

doped oil droplets were produced. For example, droplets with an average diameter of 95 µm were generated using a channel with an 80 µm nozzle by applying an inlet pressure of 60 mbar to the dispersed phase and 25 mbar to the continuous phase. Smaller droplets, with diameters in the range of 40 µm to 50 µm), were produced using narrower nozzles and higher pressure ratios between the continuous and dispersed phases.

After the collection of each droplet population, both the reservoir and outlet tubing were replaced to prevent cross-contamination. Additionally, following any change in inlet pressure, the system was allowed to operate for several minutes to flush out droplets formed under intermediate pressure conditions, ensuring a narrow size distribution for each collected sample.

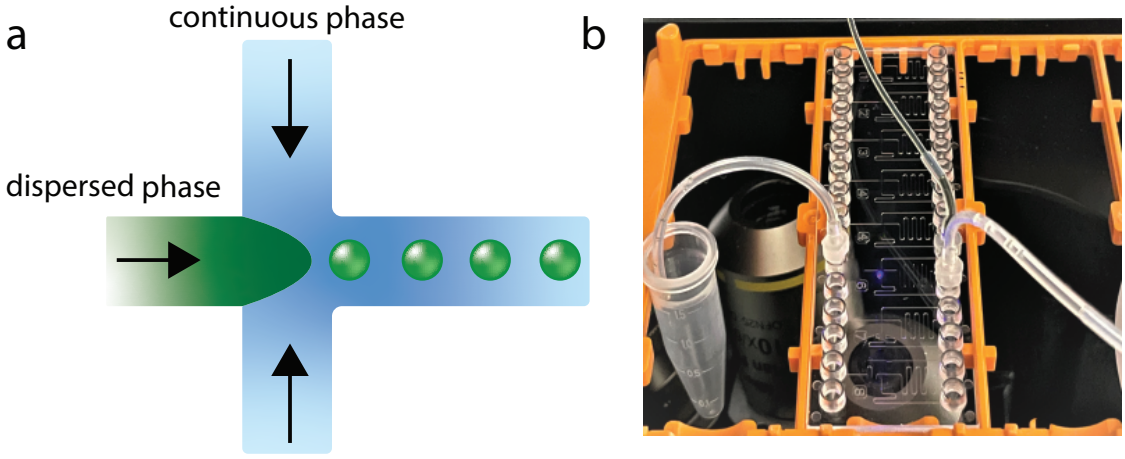


Figure 3.3: a) Schematic of the experimental setup for the generation of monodisperse droplets. b) Photograph of the setup taken during the experiment.

3.2.1.4 Mass scale production of WGM microcavities

Although microfluidic platforms are highly effective for producing monodisperse droplets (microcavities), their throughput is inherently limited, making them less suitable for large-scale production. To overcome this limitation, alternative methods were explored to produce edible monodisperse WGM microcavities at large scale while minimizing processing time.

Solid microcavities fabricated from materials such as polymethyl methacrylate (PMMA), polystyrene, and silica have been widely reported in the literature, typically produced via emulsion or dispersion polymerization processes [125], [126]. Among these materials, silica is edible and approved for use as a food additive [127]. Therefore, commercially available monodisperse silica microspheres of various diameters (Glantreo and CD Bioparticles) were employed and subsequently coated with an additional layer of chlorophyll-doped silica to form edible WGM microcavities. Dr. Slavko Kralj supported the development and optimization of the silica-based WGM microcavities through the preparation of the microcavities.

A stock chlorophyll-A solution was prepared by dissolving 1.2 mg of chlorophyll A (USP, reference standard, Rockville, USA) in 0.25 mL of ethanol. To this solution, 10 µL of (3-aminopropyl)triethoxysilane (99%; Merck KGaA, Darmstadt, Germany) and 10 µL of aqueous nitric acid solution (pH = 1) were added. The mixture was stirred at 600 rpm for 15 minutes in the dark to prevent photodegradation. Separately, 110 mg of silica

microspheres (for all three microsphere sizes) were dispersed in a solvent mixture containing 6 mL of ethanol, 6 mL of distilled water, and 0.5 mL of aqueous ammonia solution (26 wt.%). Into this dispersion, 125 µL of the prepared chlorophyll A solution was added, followed by 15 µL of tetraethoxysilane (TEOS; Merck KGaA, Darmstadt, Germany). The reaction mixture was stirred at 350 rpm for 6 hours in the dark to allow the uniform deposition of chlorophyll-doped silica on the microspheres. To achieve optimal coating, the procedure was repeated once to deposit a second chlorophyll-containing silica layer. The multilayer approach ensured that the TEOS concentration in each step remained sufficiently low, thereby reducing the risk of homogeneous nucleation and formation of free silica nanoparticles instead of uniform coating. Since chlorophyll molecules are incorporated into the silica matrix primarily through electrostatic and hydrophobic interactions rather than covalent bonds, some leaching could occur over time. To address this, the microspheres were coated with an additional outer silica layer that contained no chlorophyll. This final protective coating was applied using the same procedure as before, but omitting the chlorophyll solution. After the final coating step, the chlorophyll-coated silica microspheres were washed three times with 15 mL of distilled water and stored in the dark until use.

In some of the experiments, these microcavities were embedded in food-grade agarose films. To prepare these films, 0.5 g of agarose powder (Fisher Bioreagents, BP160-100) was dissolved in 50 mL of distilled water with continuous stirring to prevent clumping. The mixture was autoclaved at 121 °C for 20 min to ensure complete dissolution. After autoclaving, the solution was allowed to cool to approximately 80 °C. The chlorophyll-coated silica microspheres were then added and mixed thoroughly. The resulting mixture was poured into petri dishes and allowed to solidify at room temperature. The solidified plates were then sealed with parafilm to prevent evaporation and stored at 4 °C until use. All prepared plates were used within one week of preparation.

3.2.2 WGMs for sensing

3.2.2.1 pH sensing based on WGM microcavities

To demonstrate the sensing capability of edible WGM microcavities, chlorophyll-coated silica microspheres were embedded in a chitosan film for pH sensing. The chitosan films containing silica-chlorophyll microspheres were prepared as follows: 0.2 g of chitosan powder (low molecular weight, Sigma Aldrich) was dissolved in 20 mL of deionized water containing 2 wt% acetic acid. The solution was heated to 80 °C and stirred continuously for one hour until complete dissolution was achieved. The chlorophyll-coated silica microspheres were then added and dispersed uniformly by continued stirring. The resulting mixture was poured into a silicone mold and dried in an oven at 50 °C for 12 hours to remove water and acetic acid through evaporation. After drying, the chitosan film was gently detached from the mold, cut into the required dimensions, and washed with ethanol to remove any surface residues. The final thickness ranged from 0.15 mm to 0.4 mm.

3.2.2.2 Sugar sensing based on WGM microcavities

We demonstrated sugar sensing using WGM microcavities operated both below and above the lasing threshold. In both cases, the microcavities were directly dispersed in aqueous solutions containing different sugar concentrations. The microcavities were excited using CW lasers for solid microcavities and pulsed lasers for droplet microspheres, respectively.

3.2.3 Edible FP cavity

A FP cavity is a linear optical resonator consisting of two parallel mirrors separated by a gain medium. This configuration enables the use of both oil-soluble and water-soluble edible gain media. In this work, thin edible silver leaves were used as reflective mirrors, while food-grade agar served as both a spacer and a mechanical support for the cavity structure. The edible mirrors were prepared by attaching thin silver leaves onto agar films. The agar films were prepared by dissolving 1 g of agar (Sigma Aldrich) in 100 g of distilled water. The solution was sterilized by autoclaving at 121 °C for 20 min, then cooled to approximately 65 °C and poured into plates to obtain films about 1 mm thick. These flexible agar films provided smooth and stable substrate onto which the delicate silver leaves could be gently pressed. The FP cavity was assembled by positioning two edible mirrors parallel to each other, with an additional agar spacer layer placed at the edges to define the cavity length. This configuration created an enclosed volume between the mirrors, which was subsequently filled with the edible gain medium, either 2 mM chlorophyll-doped sunflower oil or 5 mM riboflavin sodium phosphate in water. The thickness of the agar spacer defined the optical path length of the cavity, which ranged from approximately 0.5 mm to 1 mm across different experiments. To enable the optical pumping and emission, one of the edible mirrors was made slightly shorter, allowing excitation light to enter the cavity and the resulting light to exit.

3.2.3.1 Edible sealant

An edible sealant was essential for enclosing the edible FP cavity, ensuring that the gain medium was retained and the cavity geometry was maintained during the handling and testing. In some of our experiments, the sealed cavities were even submerged in liquids for sensing applications. The sealant was prepared by mixing 2.5% w/w agar and 3.75% w/w glycerol, and 93.75% w/w distilled water. The mixture was heated on a hot plate at 80 °C under continuous stirring until a homogeneous solution was obtained. Glycerol acted as a plasticizer, improving the flexibility. The slightly cooled solution was then carefully applied around the edges of the FP cavity to form a thin sealing layer. Upon cooling to room temperature, this thin layer solidified.

3.2.4 FP cavity for sensing

To enhance the functionality of the edible FP cavity, its design was modified to make it responsive to specific environmental changes. This was achieved by introducing additional edible layers or modifying the cavity materials according to the intended sensing application. The following sections describe the fabrication of pH-sensitive and microorganism-sensitive edible FP cavities.

3.2.4.1 FP cavity as a pH sensor

To make the edible FP cavity responsive to pH variations, a chitosan film was introduced within the existing edible FP cavity structure. Chitosan was selected because it is both edible and pH-sensitive. In the modified FP cavity, the chitosan film was inserted between the mirrors of the FP cavity, serving as a sensing layer.

The chitosan films were prepared in collaboration with the Bikaris Laboratory at Aristotle University of Thessaloniki, which provided support in sample preparation and material characterization. Specifically, 1 wt % of chitosan powder (low molecular weight, Sigma Aldrich) was dissolved in 40 ml of deionized water containing 2 wt % acetic acid. The resulting mixture was stirred until fully homogeneous, then poured into a silicone mold

and dried in an oven at 50 °C for 12 hours to allow complete evaporation of water and acetic acid. After drying, the resulting film was gently detached from the mold, cut into the desired dimensions, and washed with ethanol to remove any residual acetic acid. The final chitosan film thickness ranged from 0.2 mm to 0.5 mm.

3.2.4.2 FP cavity as a microorganism sensor

The edible FP cavity was further adapted to serve as a sensor for monitoring microbial growth, achieved by replacing the agar films with modified gelatin films that supported microbial proliferation. These modified gelatin films were prepared as follows. A mixture of 12 % gelatin (Sigma Aldrich) with 5 g/L casein hydrolysate (Sigma Aldrich) and 3 g/L yeast extract (Biolife) was prepared in distilled water. The solution was sterilized by autoclaving at 121 °C for 20 min, then cooled to approximately 65 °C, and poured into plates to form films of roughly 1 mm thickness. After solidification, these nutrient-rich gelatin films were ready for further use.

3.3 Optical Setup

The optical characterization setup integrated multiple illumination sources with light-guiding and collection optics into an inverted optical microscope (Nikon Eclipse Ti2). The entire setup was mounted on an air-damped optical table to minimize vibration and provide a stable environment for precise optical measurements. The microscope was equipped with two side ports, a front port, and two dichroic mirror turrets, enabling flexible coupling of external light sources and detectors. The dichroic mirrors were configured to efficiently separate excitation light from the collected emission, allowing simultaneous illumination and detection. This arrangement provided a versatile platform capable of rapidly switching between different excitation sources without disturbing sample alignment. Samples were mounted on a motorized microscopic stage with high positional accuracy, allowing the precise alignment and individual positioning of microcavities during measurements.

Several illumination sources were employed depending on the experimental requirements. For wide-field imaging and sample inspection, a white LED source (CoolLED, pE-300) provided uniform illumination across the full field of view, enabling rapid localization of regions of interest within the sample. Furthermore, for selective excitation and operation below the lasing threshold, continuous-wave (CW) laser sources at wavelengths of 450 nm and 532 nm were coupled into the microscope and focused onto the sample using a 20X objective with a numerical aperture of 0.45. By tightly focusing the excitation beam onto a localized region of a microcavity, WGMs confined to a single circulation plane could be preferentially excited while minimizing photobleaching across the rest of the cavity.

For lasing experiments, a nanosecond pulsed laser (Opolette 355LD) equipped with a tunable optical parametric oscillator (OPO) covering a wavelength range from 400 nm to 2400 nm was used as the excitation source. The laser produced pulses with durations of approximately 5 ns to 7 ns and pulse energies of up to 3.5 mJ, enabling precise control of the excitation fluence and allowing operation both below and above the lasing threshold.

Emission from the microcavities was collected in an epi-illumination configuration using the same microscope objective employed for excitation. The collected light was directed to a spectrometer (Shamrock 500i, Andor Technology) for spectral analysis. The spectrometer was equipped with three interchangeable diffraction gratings and an adjustable entrance slit, typically set to a width of 10 µm, providing a balance between signal throughput and spectral resolution, with a maximum spectral resolution of approximately 0.05 nm.

3.3.1 Setup for barcode readout

For most demonstrations, microcavities were excited and their emission was collected using the inverted microscope integrated with both the optical pumping sources and the spectrometer, as described in the previous section.

However, to enable the excitation and readout of edible microcavities embedded directly within food items, a compact fiber-lens optical assembly was developed. This setup allowed flexible measurements outside the microscope environment. In this configuration, a single optical fiber was coupled to a collimating and focusing lens, which directed the excitation light onto the surface of the sample. The same fiber simultaneously collected the emitted light from the microcavities in an epi-illumination geometry. After collection, the emitted light was separated from the residual excitation beam using a dichroic mirror and subsequently directed to the spectrometer for spectral analysis.

3.3.2 Line scaning

To further accelerate the barcode readout process, a line-scanning illumination setup was employed. In this setup, a cylindrical lens was used to focus the excitation beam into a narrow line across the sample. The cylindrical lens was used exclusively for shaping the illumination beam, while the emitted light was collected by an imaging spectrometer aligned with the illumination line. This configuration enabled the spectrometer to record spatially resolved emission spectra along its entrance slit, with one axis corresponding to spatial position and the other corresponding to wavelength. As a result, multiple microcavities could be read out simultaneously in a single acquisition, significantly increasing throughput.

3.4 Analysis of Emission Signal

Emission spectra from individual microcavities were collected under different excitation conditions, both below and above the lasing threshold, depending on the resonator type (FP or WGM). These spectra were analyzed to determine key parameters, including the cavity radius (or optical length in the case of FP cavities), as well as the refractive index of the surrounding medium.

Initially, the raw spectra were first pre-processed to remove background fluorescence. For weak emission signals, partial vertical binning was applied by summing the adjacent CCD rows to enhance the signal-to-noise ratio without compromising the spectral resolution of the spectrometer. Following the background correction, the positions of individual resonance peaks were identified. Even when the resonance's linewidth appeared below the spectrometer's resolution limit, the peak positions could still be accurately determined using a Lorentzian peak-fitting algorithm applied to data points in the vicinity of each observed resonance.

3.4.1 WGMs

For spherical microcavities, the analysis begins by measuring the FSR between resonances of the same polarization, which provides a direct estimate of the cavity diameter. Based on this diameter, a set of theoretical whispering gallery modes is calculated using the asymptotic approximation. Because the asymptotic model depends on the refractive index contrast between the cavity and its surrounding medium, the experimentally observed splitting between TE and TM modes is used to obtain an initial estimate of the external refractive index. These parameters are then used as input for the exact WGM solver, which

calculates resonance wavelengths without approximation. The exact model is evaluated over a narrow parameter range around the initial diameter and refractive index to refine the predicted mode positions. Finally, the measured and calculated resonances are aligned by minimizing an overlap metric defined as the sum of absolute wavelength differences between each experimental peak and its nearest theoretical mode. Through this iterative approach, optimized values for the cavity size, the refractive index of the surrounding medium, and the corresponding mode numbers of the experimentally observed WGMs are obtained.

3.4.2 FP cavities

In the case of FP cavities, the longitudinal resonance condition directly relates the cavity length to the spacing between consecutive spectral peaks. From the experimentally measured FSR, we first determine the optical cavity length, defined as the product of the physical cavity length and the refractive index of the cavity medium. Specifically, the optical length was obtained from the average difference in the reciprocal wavelength between successive resonance modes. Because this approach is independent of mirror reflectivity and gain characteristics, it provides a robust and straightforward method for determining the cavity's optical thickness. If the physical cavity length is required, it can be subsequently extracted by dividing the optical length by the refractive index of the cavity medium.

Chapter 4

Experimental Results and Discussion

This chapter presents the experimental results obtained from edible optical microcavities developed in this thesis. Optical resonances and lasing were demonstrated in a range of fully edible microcavities–from dye-doped liquid droplets and solid microspheres supporting whispering-gallery modes, to a linear Fabry–Pérot cavity. Beyond optical characterization, these structures were employed as optical barcodes, physical unclonable functions, and sensors capable of monitoring food-relevant parameters including sugar concentration, pH, and microorganism growth, all directly within consumable products. Together, the results establish edible optical microcavities as a unique platform for food authentication, anti-counterfeiting, and real-time quality monitoring.

4.1 Whispering-Gallery Modes Microcavities

4.1.1 Chlorophyll-doped sunflower oil droplets dispersed in water

WGM-based microlasers consist of dye-doped droplets or solid spheres in an environment with a lower refractive index. These microcavities confine light through multiple total internal reflections that occur on smooth surfaces [128]. WGMs typically exhibit very high Q factors and correspondingly low lasing thresholds, making them an ideal platform for testing potential edible dyes.

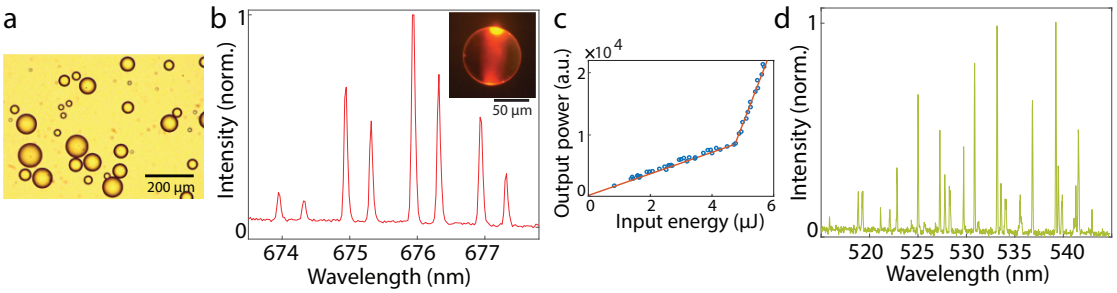


Figure 4.1: a) Bright-field image of polydispersed chlorophyll-doped oil droplets with a size range 20 µm to 120 µm. b) Emission spectrum (at pulse energy of 5.2 µJ) from a single chlorophyll-doped oil droplet with a diameter of approximately 100 µm shown in the inset. c) The output power of a droplet laser (same as in b) shows a typical threshold behavior as the input pulse energy is increased. d) Laser emission spectrum from a bixin-doped oil droplet under the excitation of a pulsed laser at 450 nm.

Lasing was achieved from droplets containing 2 mM chlorophyll-A or 4 mM bixin dis-

solved in sunflower oil. The oil phase was dispersed in water to form polydisperse droplets (see Figure 4.1a), and an edible surfactant was added to stabilize the emulsion. The droplets were optically pumped using a pulsed laser source. The emission spectra exhibited sharp spectral lines corresponding to TE and TM polarized WGM modes (Figure 4.1b for a chlorophyll-doped droplet and Figure 4.1d for a bixin-doped droplet). For chlorophyll-doped droplets, the measured Q-factors exceeded 9000, which is limited by the spectrometer resolution. The laser output power as a function of the input energy exhibited the typical threshold behavior, confirming the lasing action (see Figure 4.1c). The lasing threshold energies were 4.7 µJ for chlorophyll-A and 6.8 µJ for bixin, respectively.

We further investigated the size-dependent lasing threshold for chlorophyll-doped droplets with sizes ranging from 40 µm to 60 µm. The average lasing threshold was 4.5 µJ, with a standard deviation of 0.2 µJ. The smallest droplet size required to achieve lasing was approximately 35 µm. The lasing threshold for droplets doped with edible gain media is higher compared to WGM cavities containing high-quantum-yield commercial laser dyes (order of nanojoules), but it remains within a usable range and well below the damage threshold, which was observed at laser pulse energies about two orders of magnitude higher ($\sim$500 µJ). However, the photobleaching of the dye due to laser exposure occurred well below the damage threshold and limited continuous lasing stability. We observed stable lasing from chlorophyll-sunflower oil droplets (size 50 µm) for up to 150 consecutive pulses on average, when pumped just above the lasing threshold. In principle, however, a single pulse laser was sufficient to obtain distinct laser emission and thus determine the droplet size and optical properties.

To further evaluate the effect of pulsed laser exposure, particularly in relation to the safety of food products, we performed calculations to estimate the temperature rise in a droplet upon pulsed laser irradiation, for chlorophyll-sunflower oil droplets with diameters between 40 µm to 100 µm, the instantaneous temperature increase caused by a single 5 µJ pulse was estimated to be between 0.2 and 1 °C, indicating negligible thermal effects on the food.

4.1.2 Extracted chlorophyll-doped sunflower oil droplets in water

Instead of using commercially available chlorophyll-A, a non-purified mixture of chlorophyll extracted from spinach was also tested, along with pure olive oil. Both produced laser emission (see Figure 4.2a and b) when dispersed in water, under the excitation of a blue- or green-wavelength pulsed laser, although the lasing threshold was approximately three times higher than that of chlorophyll-A in sunflowers. Interestingly, olive oil naturally contains sufficient chlorophyll to function as a laser gain medium in the form of oil droplets, without the addition of any other substance.

4.1.3 Extracted chlorophyll-doped sunflower oil droplets inside agar matrix

In previous experiments, commercially available or extracted chlorophyll-doped sunflower oil droplets were freely dispersed in water. Their buoyancy depended on the oil density. For example, in the case of sunflower oil, after the emulsion, the droplets tended to move toward the top of the surface of the aqueous medium because of their lower density compared to the water. In contrast, droplets made from cinnamon oil remained at the bottom of the suspension because of their higher density relative to water. To immobilize the droplets and prevent such movement, we embedded them in an agar matrix.

Extracted chlorophyll-sunflower oil droplets were produced directly within the agar solution while the solution was in the liquid phase at a mildly elevated temperature. After

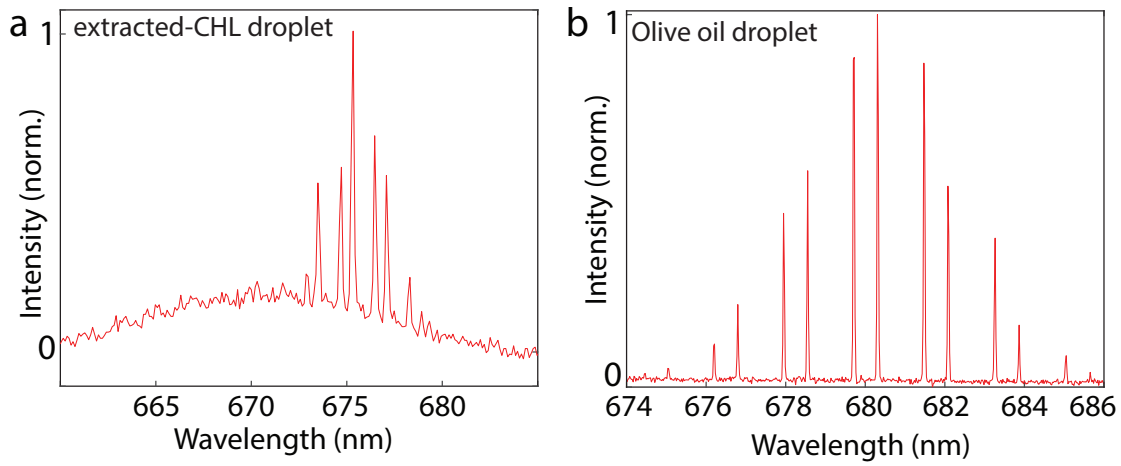


Figure 4.2: Laser emission spectra from droplets dispersed in water, upon illuminating with a blue pulsed laser, a) from an extracted chlorophyll droplet, and b) an olive oil droplet.

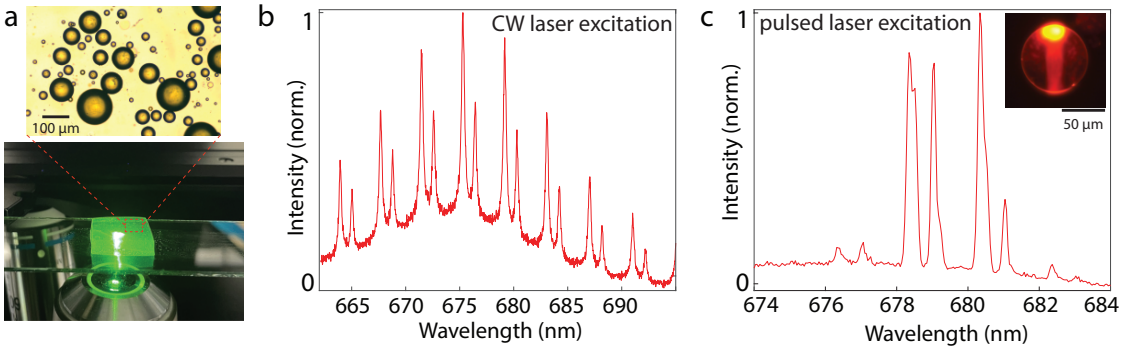


Figure 4.3: a) Extracted chlorophyll droplets inside agar matrix positioned under the microscope and illuminated with green CW laser, and the image of the droplets was recorded. b) WGM modes emission under the illumination of a green CW laser. c) Laser emission spectrum from a single droplet under the illumination of a green pulsed laser; the droplet is shown in the inset.

cooling to approximately 8 °C, the agar solidified, trapping the droplets within the matrix. The resultant solidified gel was then cut into small patches for optical characterization under a microscope, as shown in Figure 4.3a. When a single droplet embedded in the agar matrix was excited with a green CW and pulsed laser, distinct peaks were observed in the emission spectrum both below and above the lasing threshold, as shown in Figure 4.3b and c.

4.1.4 Riboflavin-doped water droplets

WGM microlasers doped with water-soluble edible dyes were also produced using riboflavin and riboflavin sodium phosphate, dissolved in a water-glycerol mixture at concentrations of 3 mM and 5 mM, respectively. These microlasers were realized as water droplets sprayed on hydrophobic or superhydrophobic surfaces, as shown in Figure 4.4a (i.e., surfaces with a water contact angle greater than 150°).

Initially, a CYTOP-coated glass substrate was employed as a superhydrophobic sub-

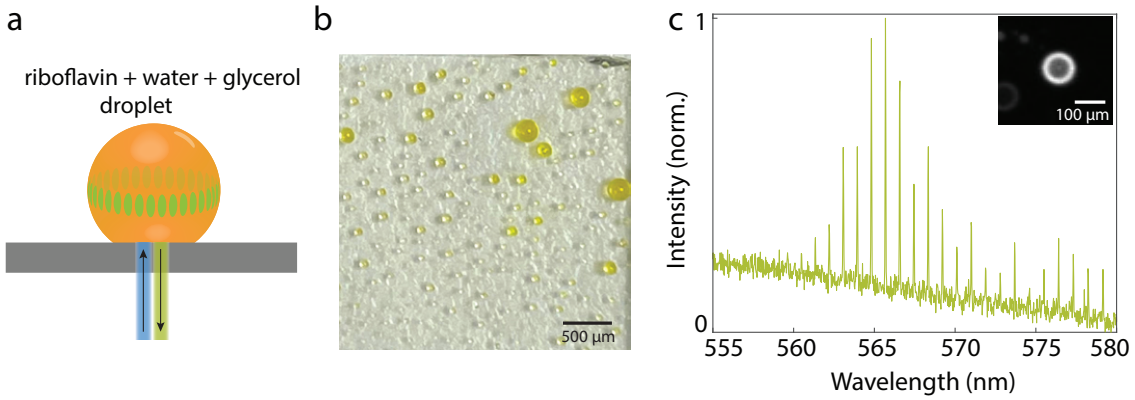


Figure 4.4: a) Illustration of an edible WGM laser as a dye-doped droplet on a superhydrophobic surface. b) Image of riboflavin-doped water-glycerol solution sprayed onto a CYTOP-coated glass substrate. c) Laser emission spectrum from a single droplet shown in the inset.

strate, on which riboflavin solution was sprayed, as shown in Figure 4.4b. When one of the droplets was pumped with a blue pulsed laser, multiple lasing modes appeared in the emission spectra (see Figure 4.4c), which may be due to the relatively larger droplet size, resulting in support of multiple optical modes.

To replace the non-edible substrate and achieve a fully edible microlaser, we explored an edible substrate suitable for this application. Many plant leaves are known to exhibit hydrophobic or even superhydrophobic behavior [129], [130], and certain edible materials have also been demonstrated to form superhydrophobic coating [131]. Therefore, spinach leaves were selected as a hydrophobic substrate to produce a completely edible laser. Following a similar procedure, the riboflavin solution was sprayed onto a spinach leaf (Figure 4.5a), forming polydispersed microdroplets. The spinach leaf was positioned on the microscope as shown in Figure 4.5b. The microdroplets emitted green fluorescent light upon excitation with a blue LED (Figure 4.5a).

When excited by a pulsed laser at 450 nm, narrow irregular peaks were observed in the emission spectra, typical of lasing modes as shown in Figure 4.5c.

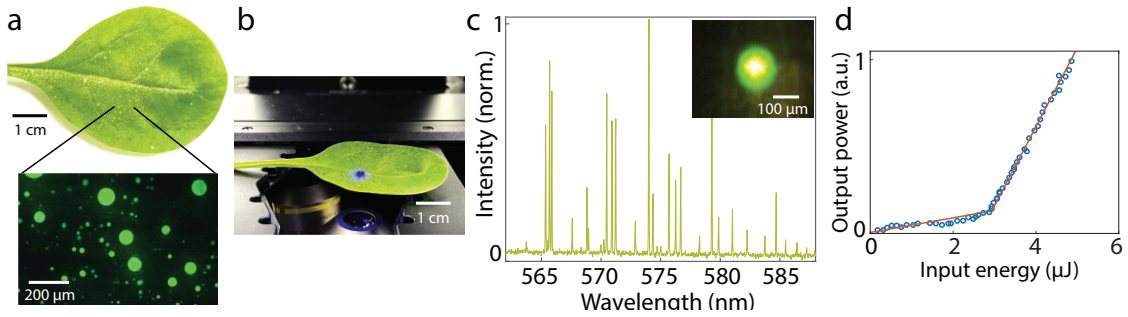


Figure 4.5: a) Riboflavin-doped water-glycerol solution was sprayed onto a spinach leaf, and the fluorescence of the resulting droplets was imaged. b) The spinach leaf was positioned on the microscope and excited by a blue pulsed laser to achieve lasing. c) Laser emission spectrum (at pulse energy of 4 µj) from a single droplet shown in the inset. d) Output of a droplet laser (same as in c) on a leaf as the pump energy is increased shows typical threshold behavior.

The laser output power as a function of input energy showed the characteristic threshold behavior, confirming the onset of lasing (Figure 4.5d). Below the lasing threshold, only fluorescence was observed. Although this result demonstrates that lasing can be achieved using edible, water-soluble dyes, such lasers are not practical for real-world applications. The droplets can slip from the surface, merge with neighboring droplets, or eventually evaporate over time. Nevertheless, this work represents a clear and important proof-of-concept demonstration.

4.1.5 Edible bubble laser

Millimeter-scale edible bubbles were produced at the end of the capillary and illuminated with a blue pulsed laser to demonstrate lasing. The bubbles consisted of a blended solution containing riboflavin, riboflavin sodium phosphate, glycerol, and Tween20. This approach is conceptually related to previously reported bubble lasers based on soap films and liquid interfaces, which can support optical resonances within their curved geometry [132]. To generate the bubbles, the capillary was dipped into this solution, and the internal air pressure was briefly increased to inflate a bubble of the desired size. The bubble size could be further adjusted by gently inflating or deflating them through controlled changes in air pressure.

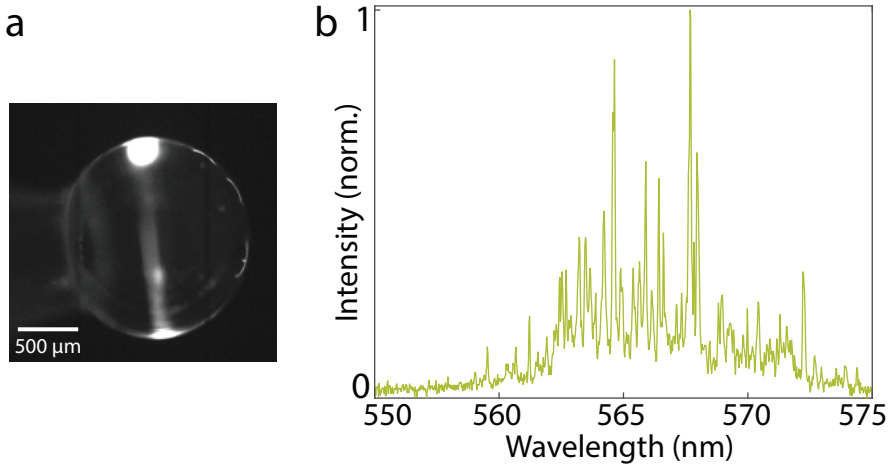


Figure 4.6: a) Bubble formed from a blended mixture with a size of approximately 1.5 mm, under the illumination of blue pulsed laser, and b) resulting emission spectrum.

Bubbles with diameters in the range of approximately 1.5-2 mm were generated and subsequently excited using a blue pulsed laser, as shown in Figure 4.6a. The resulting emission spectrum exhibited a distinct peak that confirmed the occurrence of lasing (see Figure 4.6b). However, no regularly spaced resonant peaks were observed in the spectrum, likely because of the large bubble size supporting many optical modes.

4.1.6 Edible WGM solid microspheres

Commercially available monodisperse silica microspheres with diameters ranging from 40 µm to 70 µm were used as edible WGM microcavities. The microspheres were coated with a chlorophyll-doped silica layer, followed by a protective silica layer, using the modified Stöber method [133]. The total thickness of the coating ranged from 1 µm to 2 µm. This multilayer coating approach ensured homogeneous incorporation of chlorophyll, minimized leaching, and maintained the surface smoothness of the microspheres necessary for

efficient optical confinement. Both chlorophyll extracted from spinach leaves and commercially purchased pure chlorophyll were found to be suitable as gain media, each producing clear WGM resonances.

To excite the chlorophyll-coated silica microspheres (Figure 4.7a), a 450 nm CW laser was employed. Under CW laser excitation, the chlorophyll-coated silica microsphere emitted light (as shown in Figure 4.7a), which was collected and analyzed using a spectrometer. The resulting emission spectrum exhibited a series of distinct peaks corresponding to the WGMs, as shown in Figure 4.7b. By fitting the emission spectra using the exact WGM solution, both the cavity diameter and the refractive index contrast between the cavity and its surrounding medium were determined. The refractive index of the silica microspheres was assumed to be 1.457, consistent with reported values for fused silica at visible wavelengths [134]. This known cavity refractive index allowed determination of the absolute refractive index of the surrounding medium.

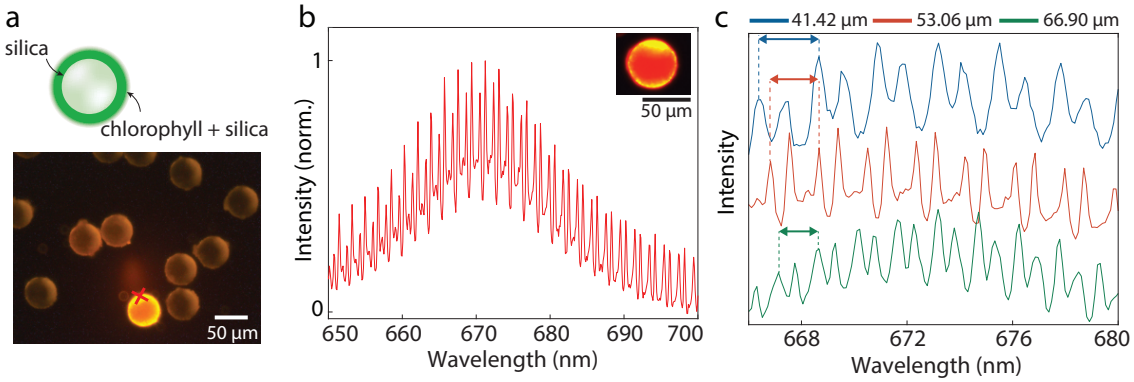


Figure 4.7: a) Schematics of the chlorophyll-coated silica microspheres and image of chlorophyll-coated silica microspheres with a mean size of 52.10 µm, one of them is under the excitation of CW laser (highlighted with a red cross). b) Emission spectrum from a single chlorophyll-coated silica microsphere (diameter of 53.06 ± 0.06 µm) immersed in water. The corresponding microsphere is shown in the inset. c) Comparison of the emission spectra of chlorophyll-coated silica microspheres of three different sizes (41.42 µm, 53.06 µm, and 66.90 µm). The colored arrows indicate the free spectral range for each microsphere, which decreases with increasing microsphere size.

Three different sizes of chlorophyll-coated silica microspheres were tested, and their corresponding emission spectra are shown in Figure 4.7c. The measured Q factors for microspheres with diameters ranging from 40 µm to 70 µm were between 2,000 and 10,000, while for sizes above 50 µm the measured Q factor was limited by the resolution of the spectrometer. In our case, the minimum microsphere size was approximately 40 µm, which was sufficient to support WGM modes. Reducing the size further lowers the Q factor. However, for microspheres larger than 100 µm tend to support high-order WGMs, making spectral analysis more challenging.

4.2 Demonstration of Edible Microcavities-Based Barcodes

The diameter of a WGM microcavity can be determined from its emission spectrum with nanometer-scale precision [72], [123], allowing it to serve as a unique optical barcode. Two main approaches exist for WGM-based barcoding: random and predefined barcodes.

Random barcodes are generated through inherent variations in microcavity size (poly-

dispersity) that occur during the fabrication process, resulting in each microcavity having a unique and practically irreproducible spectral signature. This uniqueness is valuable for anti-counterfeiting applications. Moreover, random barcoding allows the production of a large number of unique barcodes [38], [39], [40]. Conversely, predefined barcodes require the generation of microcavities of multiple well-defined and non-overlapping sizes, and then mixing only the selected sizes to produce a unique barcode.

Only a few demonstrations of predefined WGM barcodes have been reported, such as edible WGM microlasers of well-defined sizes produced by microfluidics [111]. Furthermore, microdroplets and nanobeads were produced at the tip of the microcapillary under controlled pressure, achieving higher information capacity [123], but with comparatively slow fabrication. In general, random barcodes can be readily produced in bulk with minimal complexity. In contrast, predefined barcodes often require microfluidic or high-precision fabrication techniques, which make them comparatively slow and limited in throughput.

4.2.1 Edible microlasers barcodes produced via microfluidics

Using a microfluidic droplet generator chip (Figure 4.8a), we produced highly monodisperse chlorophyll-doped sunflower-oil droplets of various sizes. The bright-field image of the monodisperse droplets from one sample and their size distribution (extracted from their emission spectra) are shown in Figure 4.8b and c.

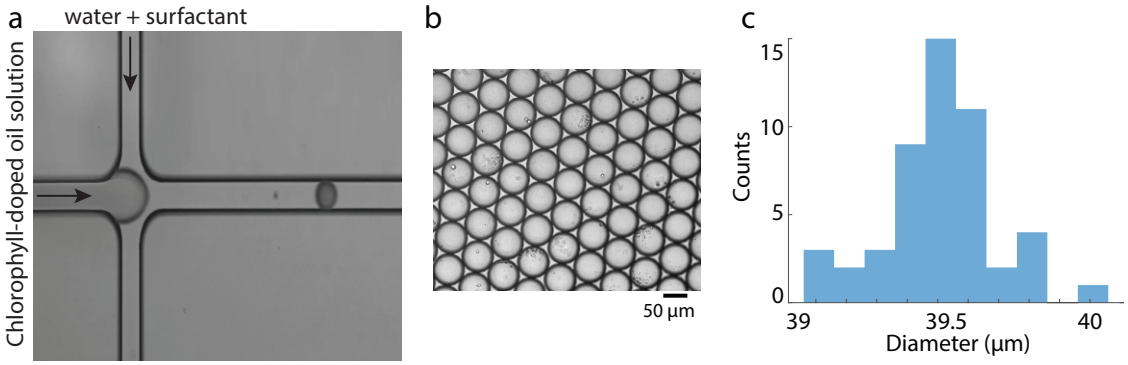


Figure 4.8: a) Microscopic view of the generation of monodisperse droplets. b) Bright-field image of monodisperse chlorophyll-doped oil droplets. c) A typical size distribution of droplets within one sample.

Upon excitation with a pulsed laser, each droplet exhibited a typical WGM lasing spectrum that depended on its diameter (FFigure 4.9a and b). Pairs of peaks were visible, corresponding to TE and TM polarizations. The size of each droplet was determined by fitting the peak positions to theoretical WGM mode solutions [135]. In this fitting, the diameter of the droplet and the refractive index of the surrounding medium (external refractive index) were used as fitting parameters, while the internal refractive index was known in advance (1.46 for chlorophyll-doped sunflower oil, measured using a refractometer).

The resulting diameter estimate had an absolute fitting error of approximately 1.2 nm. Measurements performed on about 50 droplets revealed a size coefficient of variation (CV) in the range of 0.2 % to 0.4 %. A change in the refractive index of the surrounding medium causes a shift in the WGM mode positions; however, the fitted droplet diameter, which encodes the optical barcode, remains unchanged. Thus, these barcodes are inherently robust to changes in the environment.

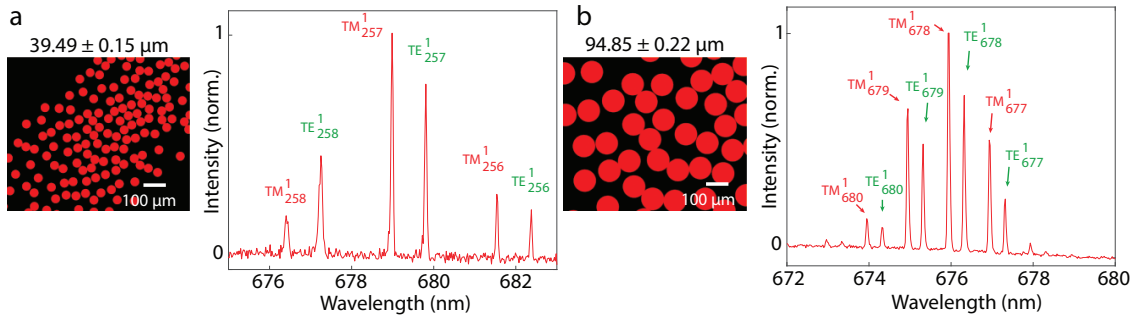


Figure 4.9: a) Fluorescence image of monodisperse chlorophyll-doped oil droplets (mean diameter $39.49 \pm 0.15\,\mu m$) and a lasing spectrum of a single droplet. b) Fluorescence image of monodisperse chlorophyll-doped oil droplets (mean diameter $94.85 \pm 0.22\,\mu m$) and a lasing spectrum of a single droplet.

To demonstrate information encoding, we produced 14 distinct sets of monodisperse droplets with non-overlapping diameters in the range of 39 µm to 95 µm (Figure 4.10a, and table 4.1). Each distinct droplet size represents one bit of binary information, being either present "1" or absent "0" in a sample. Consequently, $2^{14} = 16.384$ unique binary strings can be produced. Information such as manufacturing or expiry date, country of origin, and manufacturer identification could be encoded into food and pharmaceutical products.

Depending on the specific product and application, there are many options for positioning the microlasers in different regions of the medium. By using oils of different densities (or their mixtures), the droplets can be designed to settle at the top or bottom of a food container, or remain neutrally buoyant, allowing uniform dispersion of the microlasers throughout the whole volume of the liquid product. This approach is particularly promising as an anti-counterfeiting measure for liquid products, e.g. olive oil and honey, which are commonly adulterated. For solid non-transparent food and pharmaceutical tablets, a more suitable approach would be to embed the microlasers in a hydrogel matrix (such as agar, as discussed in the previous section) and apply it on the surface.

4.2.1.1 Demonstration of edible barcodes in liquid consumables

To demonstrate practical barcoding, we encoded a specific date in a peach compote in a glass jar and other grocery items, including a pickle jar and a juice bottle. The selected encoded date corresponded to the first international "Stop Food Waste Day" commemorated on April 26, 2017. In our encoded scheme, January 1, 2000, was defined as the starting date, represented by the binary code 00000000000001. Each subsequent day corresponded to an increment in the binary sequence, allowing coverage of approximately 44 years. The chosen date, April 26, 2017, occurred 6325 days after the starting date of our encoding scheme. When converted into a binary string of 14 digits, 6325 corresponds to the binary value of 0110001010101 (Figure 4.10b).

For this demonstration, the barcode was introduced by adding chlorophyll-doped oil droplets directly into the food product after opening the sealed container. Only <5 µL chlorophyll-doped sunflower oil was required to encode the information. Adding 5 µL of sunflower oil to 500 mL of fruit compote increased its energy content by only 0.008 kcal per 100 mL, which is negligible compared to the typical energy content of ~60 kcal per 100 mL of fruit compote. At this concentration, the added oil represents less than one part in 100,000 of the total volume of the product and is therefore expected to have a negligible effect on both the nutritional value and sensory properties of the food. In

Table 4.1: Average diameters and diameter standard deviations of the chlorophyll-doped oil droplets produced by the droplet generator chip (based on the emission spectra of individual droplets), which were used for barcoding. For each sample, 50 droplets were analyzed.

Sample	**Average diameter** (µm)	**Standard deviation** (µm)
1	39.49	0.16
2	42.88	0.11
3	45.69	0.17
4	47.24	0.17
5	52.32	0.14
6	56.39	0.22
7	62.30	0.14
8	67.76	0.28
9	70.38	0.26
10	73.43	0.21
11	81.45	0.20
12	84.30	0.15
13	87.49	0.17
14	94.85	0.22

practical applications, the barcode could be introduced after food preparation and before packaging. In this work, the thermal stability of the barcode was not investigated under cooking or sterilization conditions.

To read the encoded barcode, the sealed glass jar was scanned using a pulsed laser (Figure 4.10c). When a droplet passed through the illumination path, sharp spectral lines corresponding to WGM lasing appeared in the collected emission spectrum (Figure 4.10d). The size of each lasing droplet was calculated from its spectrum and plotted as a histogram (Figure 4.10b). All the encoded droplet sizes introduced into the glass jar were successfully detected, with an average of 5 lasers of each size observed during a few-seconds of measurement.

The barcode could be read even after more than a year of storage at room temperature on a shelf in a glass container without special light protection. However, after that period, the fluorescence intensity decreased, and the lasing was no longer sustained.

To improve the long-term stability, microlasers could be made from a solid material or embedded into an edible matrix, rather than being dispersed directly in food. The amount of encoded information could be further increased by extending the droplet size range, reducing size intervals, or using oils with higher refractive indices such as cinnamon oil ($n = 1.55$). In the size range of 40 µm to 100 µm, with a CV of 1.9 µm, approximately 30 distinct sizes can be produced with minimal spectral overlap.

4.2.2 Edible barcodes based on WGM solid microspheres

To investigate the potential of chlorophyll-coated silica microspheres as edible optical barcodes, emission spectra were collected from approximately 60 chlorophyll-coated silica microspheres from all three available sizes, with each microsphere illuminated individually using a CW laser. The microsphere sizes were determined from their WGM emission spectra, with mean sizes of 41.78 µm, 52.10 µm, and 66.89 µm. The resulting size distributions for all three sizes (Figure 4.11a) exhibited coefficients of variation (CV) of 0.45%,0.58%, and 0.48%, respectively, confirming that all three sizes are monodisperse.

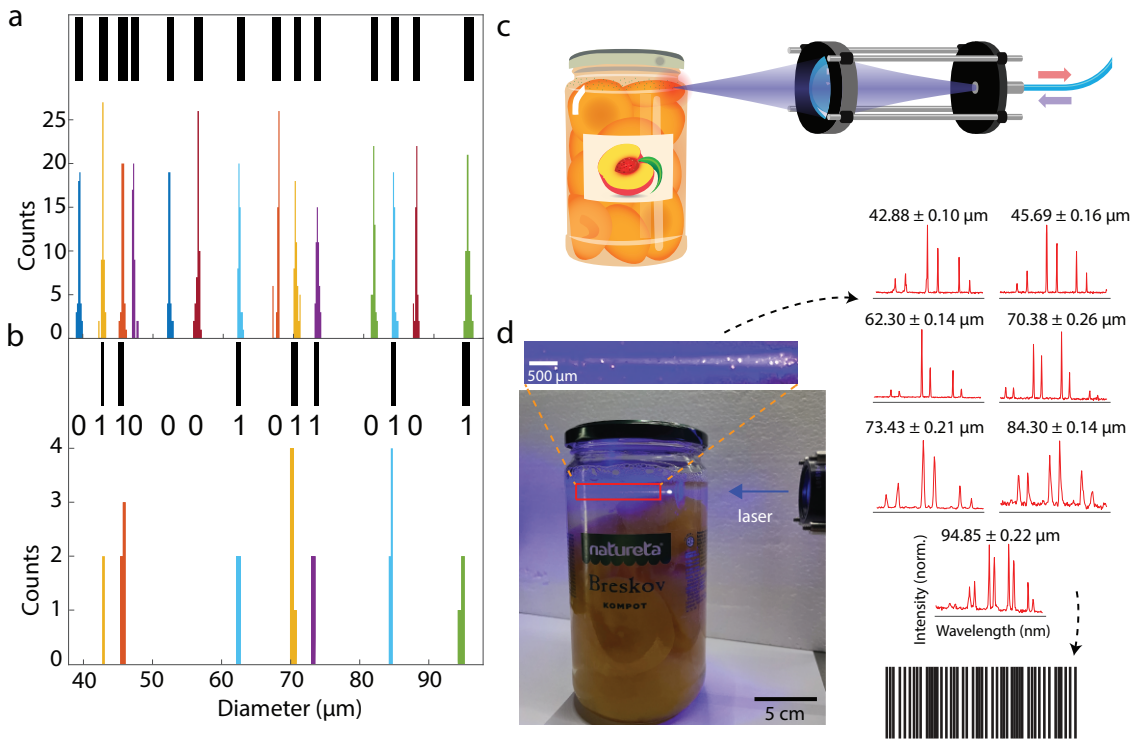


Figure 4.10: a) Size distribution of chlorophyll-doped oil droplets of 14 different diameters produced by a droplet generator chip. b) Distribution of droplet sizes detected in the jar after the date of "Stop Food Waste Day" was encoded by adding selected droplet sizes into the sample. All sizes were reliably detected. c) Schematics of the experimental setup for reading the barcodes, which includes an optical fiber for excitation and collection of the emission signals. d) Reading of an edible barcode based on chlorophyll-doped oil droplets in a jar of compote. The food product is scanned by a nanosecond pulsed laser at 440 nm. Droplet sizes are calculated from the acquired spectra, and the corresponding barcode is reconstructed.

In this demonstration, the microsphere size served as a unique barcode, since each size produced a distinct emission spectrum. This proof-of-concept demonstration was limited to only three commercially available sizes, thus only enabling the encoding of three bits of information. However, this approach can be readily extended to approximately 30 unique sizes within the range 40 µm to 100 µm without overlap, thereby increasing the information encoding capacity up to 30 bits of information. Chlorophyll-coated silica microspheres can function directly as edible barcodes without requiring embedding in a supporting matrix when suspended in low-refractive-index media such as water. They can be easily mixed into aqueous food products or sprinkled onto solid consumables.

While bare microcavities are sensitive to the change of the refractive index of the surroundings, resulting in spectral shifts. However, the size and the external refractive index can be extracted from the spectrum independently, so that even if the refractive index change influences the spectrum, the size measured from the spectra remains the same. To experimentally confirm this stability, chlorophyll-coated silica microspheres were dispersed in water containing sugar concentrations of 0% and 15%. As shown in Figure 4.11b, the size distribution remained the same in both media, indicating that the encoding information is not affected by the variation in surrounding conditions.

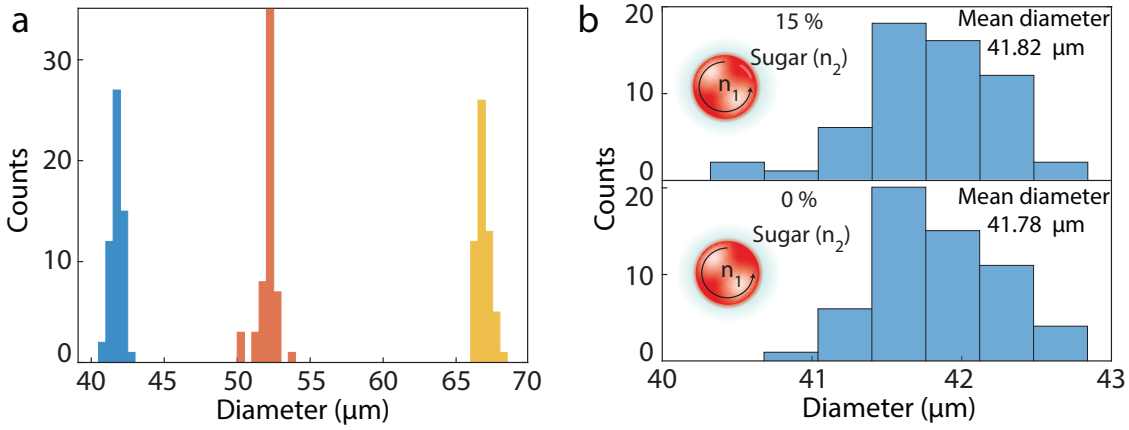


Figure 4.11: a) Size distribution of chlorophyll-coated silica microspheres from three samples of distinct sizes, obtained by analyzing the emission spectrum of 60 individual microspheres per sample. b) Size distribution of a single sample of chlorophyll-coated silica microspheres dispersed in water at 0 and 15% sugar concentration, showing that the size distribution is independent of sugar concentration.

4.2.2.1 Barcodes for high-refractive-index media

In higher-refractive-index environments, such as honey and edible oils, these bare silica spheres do not function properly due to the insufficient refractive index contrast between the microsphere and the surrounding medium. To address this issue, the chlorophyll-coated silica microspheres were embedded within a low-refractive-index agarose matrix, providing a suitable refractive index environment for microspheres. In a practical implementation, such agarose matrices containing the coated microspheres can be immersed directly into high-refractive-index consumables, such as honey. The barcode readout can be achieved by a compact setup where both excitation and emission can be guided through an optical fiber and focusing optics, as shown in Figure 4.12a.

As a proof-of-concept demonstration, an agarose thin film, 2 cm × 2 cm and 0.2 mm thick, embedding chlorophyll-coated silica microspheres was introduced into a bottle of honey, as shown in Figure 4.12b. The corresponding emission spectrum from a single microsphere within the film is shown in Figure 4.12c. The film remained stable for at least one month.

4.2.2.2 Barcodes for solid consumables

In this demonstration, an agarose thin film containing chlorophyll-coated silica microspheres was applied directly to the surface of an apple, as shown in Figure 4.12d. To evaluate the long-term stability of the barcode within the agarose matrix, we measured the emission spectra at the initial time (0 months) and again after 6 months, as shown in Figure 4.12e. During this period, the agarose matrix containing the microspheres dried completely. As a result, in later measurements, only single modes were visible, possibly because of the smaller difference in their refractive index between the dried agarose film and chlorophyll-coated silica microspheres. Nevertheless, the fitted size remained the same in both cases, which is critical for barcoding applications.

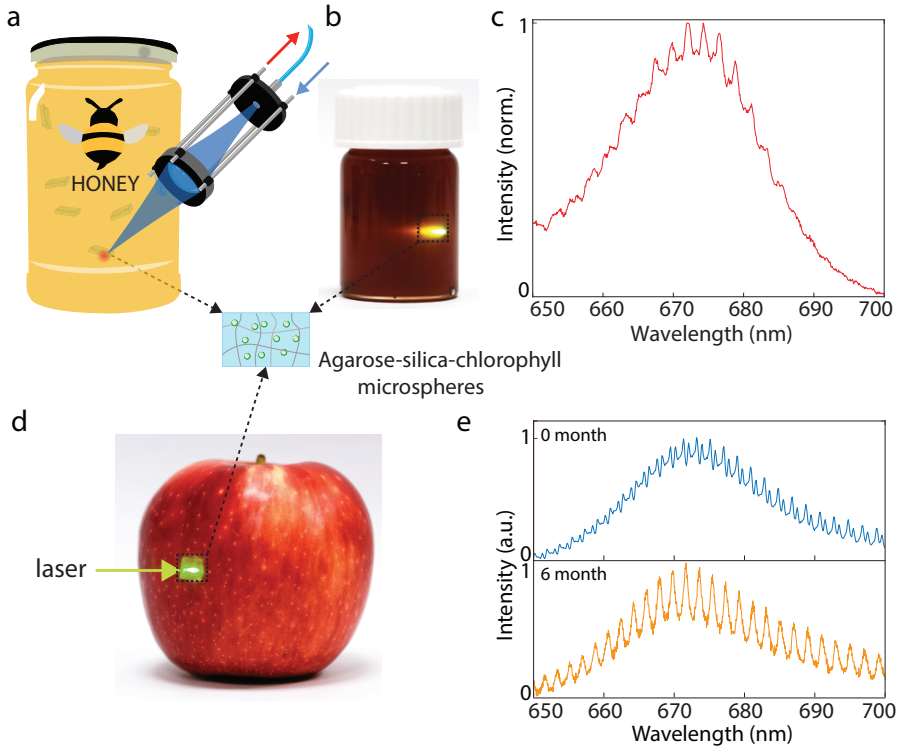


Figure 4.12: a) Illustration of an optical fiber integrated with focusing optics designed to illuminate microspheres and collect their emission in a real-time application. b) Agarose matrix containing chlorophyll-coated silica microspheres inside a honey bottle (agarose patch attached to the inner wall of an empty glass jar, which was subsequently filled with honey), illuminated by a CW laser, and c) emission spectrum collected from agarose matrix. d) Agarose matrix containing chlorophyll-coated silica microspheres attached to an apple surface, illuminated by a green CW laser. e) Emission spectra of chlorophyll-coated silica microspheres inside the agarose matrix at 0 and 6 months, under the excitation of CW laser, note that the agarose film was fully dried before the six-month measurement.

4.3 Edible Physical Unclonable Functions (PUFs)

A PUF is a physical system that naturally produces unique and unpredictable responses to specific inputs, owing to inherent random variations in its physical structure. These variations are practically impossible to reproduce or duplicate, even by the original manufacturer. PUFs can be realized using edible optical microcavities, such as droplets or solid microspheres, where slight variations in their sizes lead to unique emission spectra. Such edible PUFs can be embedded within or dispersed directly into consumable products, providing a unique and secure method for authentication of consumable products.

4.3.1 Edible PUFs based on droplet microlasers

Droplet microlasers can serve as edible PUFs because of the intrinsic randomness in their size distribution. The small but unavoidable polydispersity within each defined size range (Figure 4.8c) can be used to encode a random optical barcode that is unique for each sample. Because the droplet size can be optically measured with a precision of approximately 1 nm, while the droplets themselves can only be generated with a precision of about ~200 nm, exact duplication of a specific barcode is practically impossible. There-

fore, the droplet lasers can encode information and simultaneously function as a PUF, providing an effective anti-counterfeiting measure for high-value products. When information encoding is not required, and only PUF is required, droplets can be intentionally produced with greater size variability [38], [39], [40]. In such cases, microfluidics fabrication is unnecessary–droplets can be formed simply by dispersing oil in water through mechanical stirring.

4.3.2 Demonstration of edible PUFs based on solid microspheres

Although droplet microlasers effectively demonstrate the edible PUFs concept, they require a pulsed laser source to obtain their optical signatures, which is relatively bulky and expensive. To overcome this limitation, we demonstrated edible PUFs using chlorophyll-coated silica microspheres that can be excited using a CW laser.

Microspheres of various sizes (as shown in Figure 4.11a) can each function as a PUF. The slight natural polydispersity within a microsphere sample (mean size $\pm$ 0.5 µm) produces a random distribution, which acts as a unique identifier. The size of the microsphere can be measured with a precision of 40 nm (estimated by repeated measurements of the same microsphere). In contrast, the production precision is limited to approximately 500 nm. This significant mismatch between measurement resolution and microsphere production ensures that the exact replication of any PUF sample is impossible.

For proof-of-concept demonstration, chlorophyll-coated silica microspheres with an average diameter of 52 µm were embedded into small agarose patches, forming edible PUF samples. Six different agarose patches were prepared, each containing 5 to 10 chlorophyll-coated silica microspheres. Initially (at 0 months), individual microspheres in each sample were manually positioned under the microscope, illuminated with a CW laser, and their emission spectra were recorded to determine their sizes. The same samples were re-measured after six months to evaluate stability. Figure 4.13a shows the microsphere sizes measured for one sample at the beginning and after six months. Each patch was thus characterized by a distinct distribution of microsphere sizes, resulting in stable, unique, and non-reproducible PUFs.

Using microspheres with a mean diameter of 52 µm $\pm$ 0.26 µm and a measurable size precision of 40 nm, approximately 13 different microsphere sizes can be fitted in this size range. The total number of unique PUFs can be estimated as the number of possible combinatorial relationships: $N_{\mathrm{PUFs}} = \binom{n}{k}$, where $n = 13$ is the number of distinguishable microsphere sizes and $k = 5$ is the number of microspheres within one patch. This corresponds to approximately $N_{\mathrm{PUFs}} = 10^3$ unique PUFs. This number can be significantly increased by taking a larger interval of sizes instead of taking just the relatively monodisperse single sample. By expanding the whole usable size range of 40 µm to 70 µm, the number of unique measurable sizes is 750, the resultant a total number of combinations would be $N_{\mathrm{PUFs}} = \binom{750}{5} = 10^{13}$.

To accelerate the scanning process, we followed a line-scanning illumination using a cylindrical lens as shown in Figure 4.13b). The cylindrical lens was used only for illumination, while the emitted light was collected by an imaging spectrometer aligned with the illumination line. This configuration enabled the spectrometer to record spatially resolved spectra along its slit, with one axis corresponding to the spatial position and the other to wavelength. However, in our measurements, the recorded spectra were summed along the slit and over time to obtain a single integrated emission spectrum for the whole sample. Thus, the final spectrum represents the sum of spectra from all the microcavities in the sample. The integrated spectrum comprises emission peaks originating from multiple beads and provides a unique spectral signature without requiring individual bead-size fitting. Although it is possible to acquire a full hyperspectral image by keeping both spa-

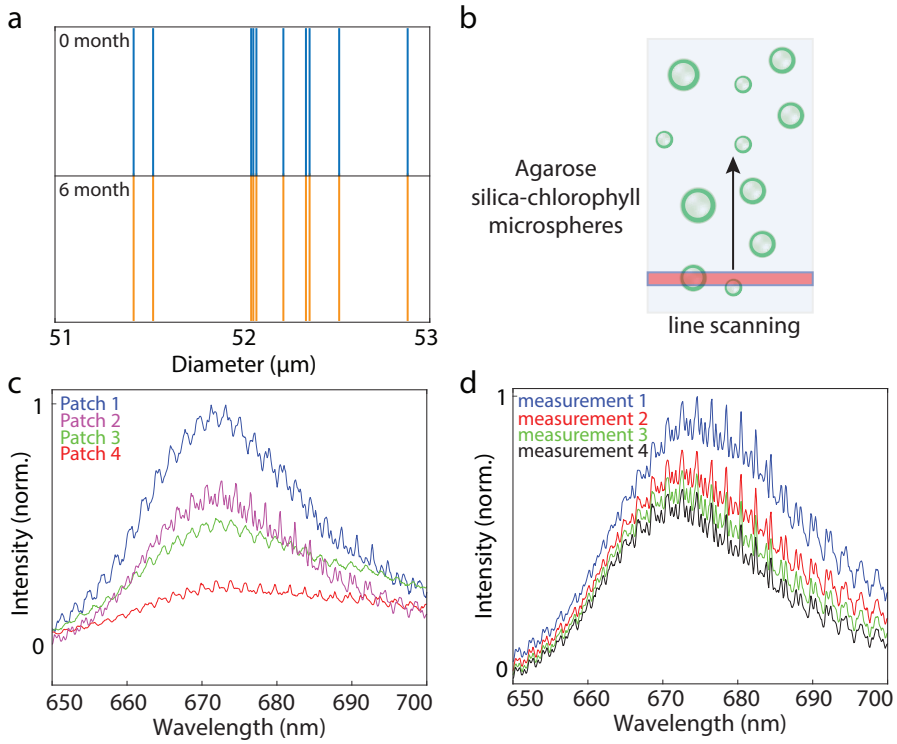


Figure 4.13: a) Size distribution of chlorophyll-coated silica microspheres within the agarose matrix, measured at 0 and 6 months, by illuminating individual microspheres with a laser. b) Schematics of an agarose patch containing chlorophyll-coated silica microspheres as PUFs, with line scanning used to illuminate the microspheres. c, d) Integrated emission spectra from line scans of agarose patches (200 µm × 500 µm) containing chlorophyll-coated silica microspheres c) Spectra from four different patches, each with 4–5 microspheres, d) Spectra from repeated scans of a single patch with five microspheres, with each spectrum representing one scan.

tial and spectral information, such an approach requires comparatively more processing time and data handling. Alternatively, our method enables faster measurements while still producing a sufficient number of unique PUFs. Using this method, four samples (agarose patches containing chlorophyll-coated silica microspheres) were scanned. Each scanned patch covered a 2D area of 200 µm × 500 µm, containing 4–5 microspheres, and the scan was performed at a speed of 0.2 mm s^{-1}, the total scan time per sample was 50 s. The resulting emission spectra (Figure 4.13c) demonstrated the uniqueness of the optical PUFs. Under the same conditions, a single patch was scanned four times at one-minute intervals (Figure 4.13d). The emission spectra remained consistent across all scans, indicating good reproducibility, although a gradual decrease in emission intensity was observed, possibly due to photodegradation of chlorophyll.

This fast and repeatable readout could greatly enhance the applicability of these edible PUFs for barcoding applications. In the future, the current setup, which relies on stage movement for sample positioning, could be further simplified by replacing the stage motion with optical scanning using galvanometer mirrors (galvo mirrors), which rapidly steer the excitation beam across the sample without requiring mechanical movement of the sample itself.

4.4 Edible WGM Sensors

WGM microcavities are widely used in sensing applications due to their extreme sensitivity to changes in size, shape, and the refractive index of their surroundings [43], [44]. Even very small perturbations lead to measurable shifts in the WGM resonance wavelengths, enabling the detection of chemical and physical parameters in a medium. In this thesis, we demonstrate edible WGM microcavity-based sensors mainly in two forms: chlorophyll-doped sunflower oil droplets serving as microlasers, and chlorophyll-coated silica microspheres operating below the lasing threshold. These edible optical sensors can be directly integrated into food and other consumable products for real-time sensing. Specifically, we demonstrate sensing of sugar concentration and pH through refractive-index-induced shifts of the WGM resonances, as well as temperature sensing based on thermally induced deformation of the microcavity.

4.4.1 Demonstration of sugar sensing based on WGM microlaser

One key parameter routinely measured in the food industry is sugar content, typically estimated via refractive index using a refractometer. For beverages such as wine, beer, maple syrup, or honey, a sample must be collected and inserted into a refractometer to measure the refractive index. If such a sensor were present inside the fluid itself, it would be possible to continuously monitor sugar concentration, including in a sealed container, such as in a bottle where fermentation occurs. The refractive index increases with sugar concentration because dissolved sugar molecules increase the optical density and polarizability of the solution. Consequently, higher sugar concentrations result in a higher refractive index, providing the basis for refractometric sugar measurements.

WGM microcavities can be used to measure the absolute refractive index of the surrounding medium [72], [136]. We used chlorophyll-doped sunflower oil droplets to measure the external refractive index at several different glucose concentrations. Fitting of the droplet size and the external refractive index was performed for the spectra of each droplet, and the external refractive index was averaged over five droplets from each sample, with a standard deviation of 0.0003 RIU (Figure 4.14). This allows a glucose concentration measurement with a 0.2 percentage point error, comparable to standard commercial refractometers. Other substances in the food, apart from sugar, could also change the refractive index. However, especially in the beverage industry, the refractive index is commonly used to measure sugar concentration. Therefore, our method is compatible with the standard measurements within these food industries.

The demonstrated concentration range was limited by the refractive-index contrast between the sunflower-oil microcavity and the surrounding medium. Measurements at substantially higher sugar concentrations would likely require edible microcavities with a higher refractive index to maintain efficient optical confinement by total internal reflection.

4.4.2 Temperature indicator

We developed an edible temperature indicator using a WGM laser, which irreversibly changes when exposed to a specific temperature (Figure 4.15a). This indicator can detect if food has been exposed to high temperature, unfrozen, or adequately heat-treated to eliminate harmful pathogens.

Our indicator was made from chlorophyll-doped butter microspheres. At a temperature above butter's melting point of 35 °C, the beads deformed, and the lasing ceased (Figure 4.15a and b). To show the transient change, a series of emission spectra at various temperatures is shown in Figure 4.15c. Once the cavity is deformed, it cannot be reversed.

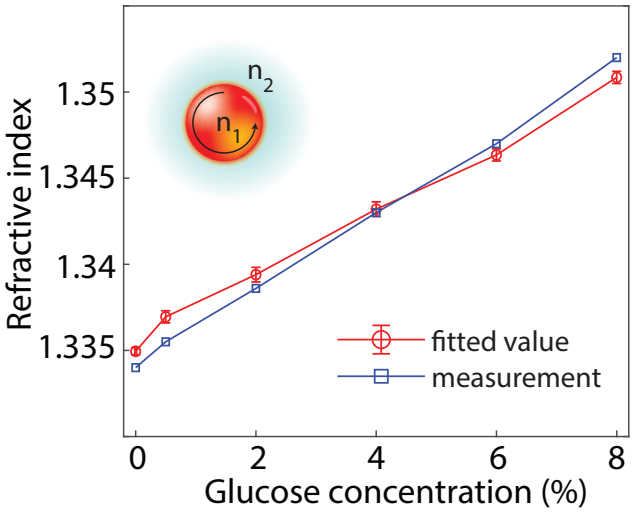


Figure 4.14: The refractive index was measured for different concentrations of glucose in water. The red line represents the refractive index determined from the lasing spectrum of the droplets, while the blue line corresponds to measurements obtained using a conventional refractometer.

Therefore, it is a good indication that the temperature was above the melting point at some point during the transport or storage of food or pharmaceutical products. Our sensor can show if a product was at a temperature above the melting temperature of the sensor, but not for how long it was exposed to that temperature. Based on the desired application, cavity materials with different melting points can be used. Fatty acids have a broad range of melting temperatures from −45 °C to 80 °C [137]. Edible waxes can also be used instead of fats.

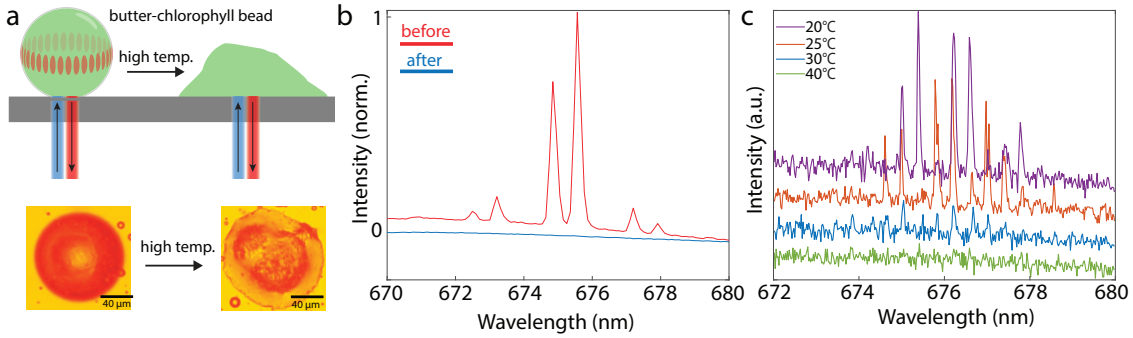


Figure 4.15: a) Schematic diagram of the temperature indicator before and after exposure to a high temperature, and bright-field images of the temperature sensor based on a chlorophyll-doped butter bead at low and high temperatures. b) Emission spectra from a temperature sensor at room temperature and after it has been exposed to a high temperature (35 °C). c) Emission spectra from a chlorophyll-doped butter microsphere at various temperatures upon the excitation with a blue pulsed laser.

4.4.3 Demonstration of edible sensors based on WGM microspheres

4.4.3.1 Sugar sensing

To further explore the edible sugar sensing, we employed chlorophyll-coated silica microspheres as edible optical microcavities operating below the lasing threshold to determine the sugar concentration of aqueous solutions by monitoring variations in their refractive index. The microspheres were dispersed in aqueous sugar solutions of varying concentrations. For each concentration, the spectra of five individual microspheres were recorded, and the external refractive index was determined by fitting the emission spectra (Figure 4.16a). The resulting refractive index values increased linearly with sugar concentration, resulting in a slope of 0.0031 RIU per % sugar. The average variation among the refractive index values was 0.0013 RIU, with a minimum detectable shift of 0.0007 RIU. Based on slope calibration, these values correspond to sugar concentration uncertainties of 0.42 and 0.23 percentage points, respectively. For validation, the same sugar solutions were measured using a standard refractometer (Figure 4.16a). The refractive index values determined from the edible microcavities showed excellent agreement with the refractometer, with an average absolute deviation of 0.001 RIU, which corresponds to only 0.07 percentage points across all concentrations. For reference, commercially available refractometers used in industrial applications, such as measuring sugar in wine, typically have an accuracy of ± 0.2 percentage points.

One possible application of our edible sensor is the continuous monitoring of sugar content in sealed beverages, such as sparkling wine or beer, during fermentation. To assess the compatibility of our chlorophyll-coated silica microspheres with the alcoholic environment, the microspheres were directly dispersed in different media, and their refractive indices were measured (Figure 4.16b). The edible microcavities showed stable optical emission in these media for over one month. For validation, the refractive indices of the same samples were also measured using a refractometer, resulting in comparable values (Figure 4.16b). For practical implementation, the edible microspheres can be embedded within an agarose matrix and either attached to the inner surface of the bottle (Figure 4.16c) for convenient optical readout or scanning, or left freely suspended within the liquid, allowing them to float throughout the solution.

In addition to determining the refractive index from spectral fitting, sugar concentration can also be quantified directly from the spectral shift of the WGM emission peak. Figure 4.16d shows the emission spectra of chlorophyll-coated silica microspheres dispersed in two aqueous sugar solutions with different concentrations. A clear red-shift of the emission peak is observed as the sugar concentration increases, corresponding to the increase in the refractive index of the surrounding medium. From the measured wavelength shifts and the corresponding refractive index values, an optical sensitivity of 208 nm/RIU was determined. This demonstrates that the edible microcavities can also function as refractive-index sensors based solely on monitoring spectral shifts.

4.4.3.2 pH sensing

Beyond sugar detection, pH monitoring is essential to assess food freshness [89], [138], as changes in pH often indicate spoilage or microbial activity. To address this, we embedded the chlorophyll-coated silica microspheres into a chitosan film (Figure 4.17a). Chitosan is an edible, pH-responsive polymer that swells at lower pH due to increased water uptake, leading to a decrease in its refractive index. To evaluate the sensitivity of chitosan, we immersed a pure chitosan film in solutions of three different pH levels separately, demonstrating different swelling behavior, as shown in the Figure 4.17b. Subsequently, we tested the chitosan film containing chlorophyll-coated silica microspheres (see Figure 4.17a) for

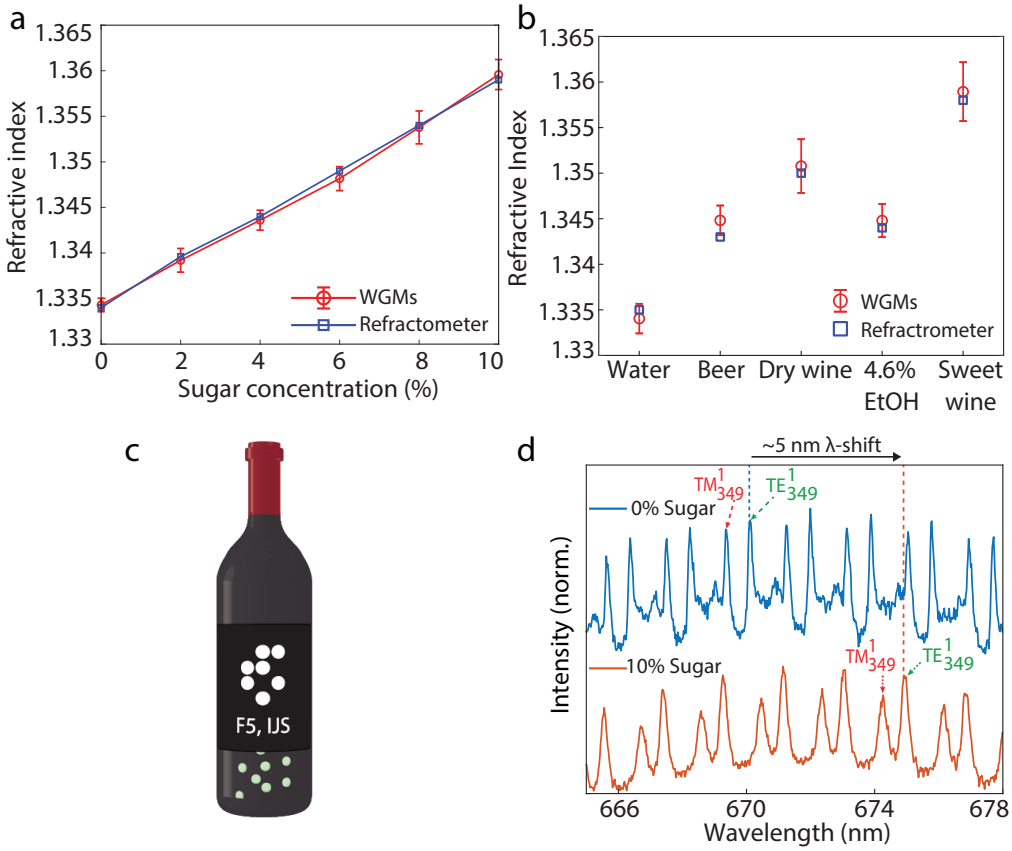


Figure 4.16: a) Comparison of refractive index measurements: a) of sugar solutions at different concentrations, and b) across various media using edible microcavities by directly dispersing chlorophyll-coated silica microspheres inside the solutions and measuring with a refractometer. c) Schematic of a wine bottle containing chlorophyll-coated silica microspheres, which can serve as a barcode. d) Emission spectra of chlorophyll-coated silica microspheres dispersed in two different sugar solution concentrations.

pH sensing based on refractive index variations (Figure 4.17c). The results reveal a clear decrease in the refractive index of chitosan film at a lower pH solution, which was validated using refractometer measurements. Our method is capable of estimating the pH of the solution with an error of ±0.3 pH units, determined from the standard deviation of multiple measurements at each pH. This approach enables real-time pH monitoring of various food products, such as milk and fruit juices. Moreover, these edible sensors offer a non-invasive solution for food safety and quality control and are suitable for integration into packaging. While other packaging sensors often rely on colorimetric dyes to detect parameters such as pH, temperature, or oxygen levels, they are limited by lower sensitivity [90] and are mostly composed of materials that are not fully edible.

Beyond refractive-index fitting, pH can also be determined directly from the spectral shift of the WGM emission peak. Emission spectra of chlorophyll-coated silica microspheres embedded within a chitosan film were recorded while the film was immersed in solutions of different pH. From the measured wavelength shifts and the corresponding pH values, an average pH sensitivity of approximately 5.7 nm/pH was obtained over the pH range from 7 to 3 (see Figure 4.17d). Notably, the highest sensitivity was observed between pH 7 and pH 6, reaching approximately 13.7 nm/pH. As the pH decreased further below pH

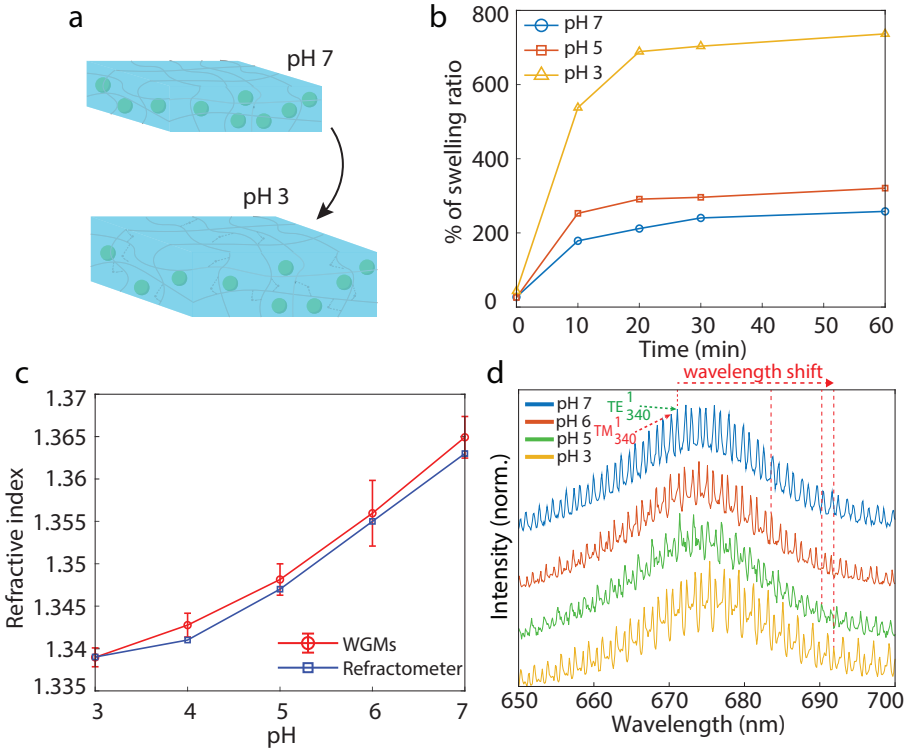


Figure 4.17: a) Schematic of chlorophyll-coated silica microspheres embedded within a chitosan hydrogel matrix at pH 7 and pH 3. As the pH decreases, the chitosan swells progressively, taking up more water and thereby reducing its refractive index. b) Chitosan film immersed in various pH solutions, with its weight measured at different time intervals, and the swelling behavior was significantly pH-dependent. c) Comparison of refractive indices measured using edible microcavities and a refractometer. A chitosan film embedded with chlorophyll-coated silica microspheres was immersed in solutions of known pH, and the refractive indices obtained from both methods showed good agreement. d) Emission spectra of chlorophyll-coated silica microspheres embedded within a chitosan film were measured while immersed in solutions of different pH.

5, chitosan swelling approached saturation, resulting in a reduced spectral sensitivity.

4.5 Edible FP Cavity

The second type of an edible laser was based on an FP resonator, a linear cavity consisting of two mirrors with a gain medium between them. The most reflective edible materials are silver, gold, and aluminum. In food, they are usually used in the form of extremely thin leaves, mainly as decorations for sweets and drinks. In our proposed FP edible laser, two edible mirrors, each consisting of a thin silver leaf attached to a layer of agar for structural support, were separated by an additional agar layer acting as a spacer, but only at the cavity edges (Figure 4.18a and b). The space in between the mirrors was filled with 2 mM chlorophyll solution in sunflower oil or with 5 mM riboflavin sodium phosphate solution in water. One edible mirror was made intentionally shorter to enable the excitation light to enter the cavity and the resulting laser light to exit the cavity. Upon pumping the cavity filled with a chlorophyll-doped sunflower oil with a pulsed laser, above the lasing-threshold energy of 6 µJ, sharp, equally spaced peaks appeared in the emission spectrum, indicative

of lasing within the FP cavity (Figure 4.18c and d). The average lasing threshold was 5.9 µJ, with a standard deviation of 0.2 µJ. Similarly, lasing was also achieved with a cavity filled with riboflavin sodium phosphate solution in water. Using the flexible agar for the mirror substrate and especially for spacers makes the device susceptible to mechanical deformations that could impair its lasing output. This can be solved by attaching the laser to a firm food packaging or replacing the agar with other, more rigid edible materials, such as shellac, silk, and natural gums.

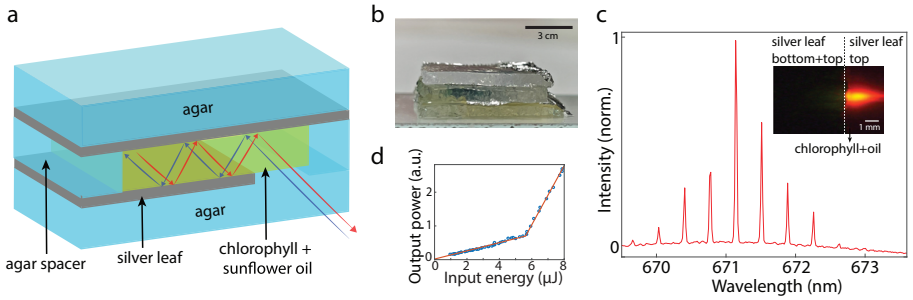


Figure 4.18: a) Schematics of an edible FP cavity laser. The cavity is filled with chlorophyll-doped oil and illuminated by a pulsed laser. The excitation/emission light enters/exits at the position where the silver leaf is only present on one side of the cavity. b) Side view of an edible FP cavity laser. c) Laser emission spectrum (at pulse energy of 6.5 µJ) from an edible FP cavity shown in the inset. d) Output of a FP cavity laser (same as in c) as the pump energy is increased, shows typical threshold behavior.

4.6 Demonstration of Edible Sensors Based on FP Cavity

4.6.1 pH sensing

We demonstrated a completely edible pH sensor based on the edible FP cavity. The free spectral range of an FP cavity can be calculated as FSR $= (2nL)^{-1}$, where n is the refractive index within the cavity (refractive index of the gain solution), and L is the cavity thickness. From the measured value of the FSR (Figure 4.18c), we were able to calculate the thickness of the optical cavity of 300 µm with an error of 600 nm. To make the FP microlaser pH sensitive, an additional chitosan film was introduced in between the edible mirrors (Figure 4.19a). Chitosan swells as the pH value decreases (Figure 4.17b) [139]. When a change in pH occurred, the thickness and refractive index of the chitosan film changed, which resulted in a change of the FSR of the laser emission (Figure 4.19b). The FSR decreased approximately linearly with increasing pH (Figure 4.19c). Across the sensor, the chitosan film thickness exhibited a variation of up to 0.1 mm, which translates into an error of 0.3 pH units. Therefore, to measure the pH accurately, the sensor was always pumped at the same spot, resulting in repeatable and robust measurements. The error in measuring pH was 0.05 pH units, which was estimated by repeating the measurements. In the future, if such sensors were made on an industrial scale, the thickness could easily be made much more uniform, meaning that pumping at any position would give the same result. It is worth noting that the swelling ratio changes with temperature. The swelling ratio nearly doubles at the same pH when the temperature increases from 25 °C to 45 °C [140]. This could be compensated for if the temperature is measured simultaneously with another edible sensor.

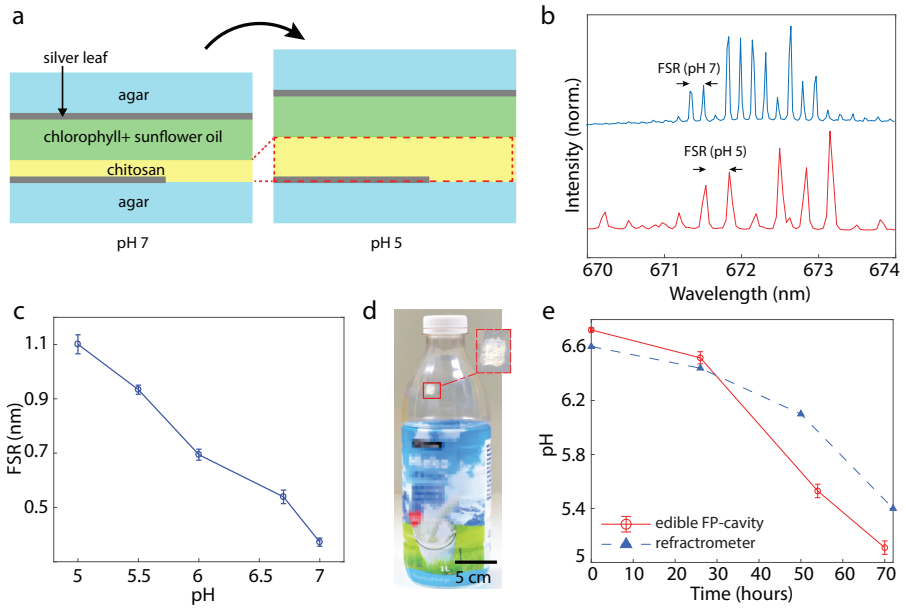


Figure 4.19: a) Schematic diagram of the edible FP cavity-based pH sensor at two different pH values. The chitosan layer swells as the pH is reduced, changing the emission of the laser. b) Emission spectra from an FP cavity pumped with a nanosecond pulsed laser at 440 nm at two different pH values. c) The change of FSR with respect to the pH change. d) An edible FP-laser pH sensor inside a milk bottle measures the pH of milk. e) Change of the milk's pH over two days when left at room temperature, measured by a FP laser and a pH meter on two different samples. Lowering of the pH indicates milk spoilage.

We tested the pH sensor by measuring milk pH as it spoiled over several days at room temperature. The sensor was fixed inside a milk bottle with an edible sealant (Figure 4.19d) and submerged in milk during the measurement. By taking into account the previously measured dependence of FSR on pH (Figure 4.19c), the change of pH in time was determined (Figure 4.19e). These results agree well with the usual drop in pH when milk gets spoiled [141].

4.6.2 Detection of microorganism growth

We developed an FP cavity-based sensor for detecting microorganism growth inside food. The FP laser was assembled as described before (Figure 4.18a), except that the agar layers were replaced by nutrient-enriched gelatin (Figure 4.20a). During its preparation, the sensor was contaminated with microorganisms (bacteria/fungi) from the air, leading to microorganism growth in gelatin in the following days. Some microorganisms produce the enzyme gelatinase, which digests the gelatin layers within several days, resulting in liquefaction of the medium. This caused the laser cavity to fall apart and not support lasing anymore (Figure 4.20b and c). The disappearance of the laser signal indicated significant microbial growth. The microbial growth is highly dependent on the temperature. Therefore, this could also indicate if the food was kept at an elevated temperature for a longer time. In some cases, mold also started growing on the sensor, which can block the light in the cavity and indicate food spoiling. Gelatin melts at elevated temperatures. This could be exploited to use it as a multifunctional sensor, not only to detect microorganism growth but also to detect if the food was stored at a certain temperature. Alternatively, other hydrogels less sensitive to temperature, such as agar, could be used if temperature

sensitivity is undesirable. While here as a proof of concept, we purposely contaminated our sensor with microorganisms; for real-life applications, the sensor should not contain microorganisms, since this could contaminate the food. Also, the composition of the sensor must be optimized so that the rate of microorganism growth is slower than in the food product itself.

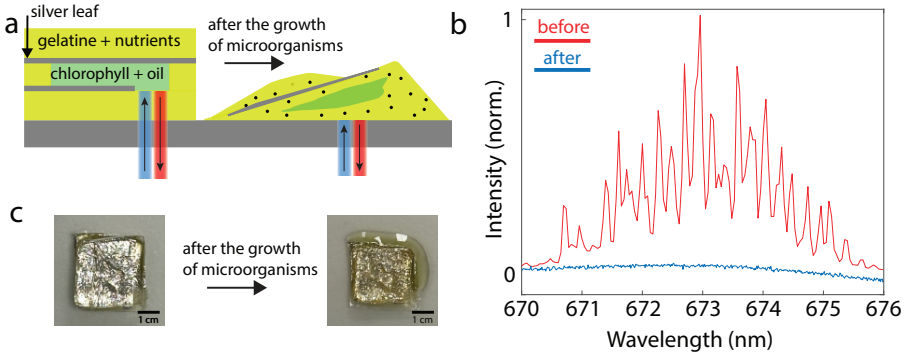


Figure 4.20: a) Schematic diagram of the microlaser-based microorganism sensor before and after the growth of microorganisms, and images of the microorganism sensor before (day 0) and after (day 5) the growth of bacteria (view from top). b) Emission spectra from the microorganism sensor before (day 0) and after the growth of bacteria (day 5).

Chapter 5

Conclusions

This thesis demonstrates that fully edible microcavities–operating both below and above the lasing threshold–can be realized and function as powerful tools for optical barcoding and sensing within consumable products.

A major contribution of this work is the identification and systematic investigation of naturally derived gain materials that serve as both optical gain media and cavity components. This thesis provides the first comprehensive demonstration of fully edible whispering-gallery-mode (WGM) and Fabry-Pérot (FP) cavities. When operated above the lasing threshold, these edible cavities exhibit ultra-narrow emission linewidths, enabling optical barcoding with the capacity to encode tens of bits of information. At the same time, their strong environmental sensitivity allows them to function as sensors, responding to changes in refractive index, sugar concentration, pH, temperature, and microbial activity. In this way, edible microcavities integrate identification and monitoring simultaneously.

A significant advancement towards practical implementation is the development of cavity-enhanced emission under continuous-wave (CW) excitation. While pulsed laser excitation enables above-threshold lasing, CW operation below the lasing threshold maintains sufficiently sharp and stable resonances for spectral encoding and sensing, while substantially reducing system complexity and cost. This strategy represents an important transition from laboratory-scale demonstrations to real-world applications. To enable this approach, monodisperse silica microspheres coated with chlorophyll were demonstrated as scalable optical barcodes and sensors compatible with CW excitation. These microcavities exhibited stable, size-dependent WGM resonances suitable for structured information encoding, physical unclonable functions (PUFs), and sensing. Their large-scale fabrication supports practical implementation, while natural size variations inherently enhance security through PUFs. Embedding the coated microspheres in edible matrices such as agarose further enabled their operation in high-refractive-index consumables (such as oil and honey) and also facilitated direct integration onto solid food surfaces. The sensing performance for sugar concentration and pH was validated through comparison with standard refractometric measurements.

Beyond the technical achievements, this research introduces a conceptual shift in product authentication and monitoring–from external labeling towards intrinsic photonic tagging. By embedding optical microcavities directly within consumables, the technology inherently resists tampering and removal, overcoming long-standing limitations of conventional packaging-based barcodes and external sensors.

Further developments may focus on expanding the range of edible gain and functional materials, optimizing cavity design, and integrating miniaturized spectral readout systems to enable compact and user-friendly authentication devices. Advances in scalable fabrication and responsive edible matrices will further strengthen the feasibility of practical

implementation. Although developed primarily for food applications, the principles established here are directly transferable to pharmaceuticals, cosmetics, agriculture, and other high-value consumables where traceability, safety, and product integrity are increasingly important.

In conclusion, this thesis establishes fully edible photonic cavities as a new class of multifunctional optical devices that combine spectral encoding and environmental sensing within consumable materials. It provides the scientific and technological foundation for embedding edible microcavities and microlasers directly into products, enabling secure authentication and real-time quality monitoring.

References

[1] Y. Wang, Z. Yuan, and Y. Tang, "Enhancing food security and environmental sustainability: A critical review of food loss and waste management," *Resources, Environment and Sustainability*, vol. 4, p. 100 023, 2021.

[2] S. Medina, R. Perestrelo, P. Silva, J. A. Pereira, and J. S. Câmara, "Current trends and recent advances on food authenticity technologies and chemometric approaches," *Trends Food Sci Technol*, vol. 85, pp. 163–176, 2019.

[3] H. Ye et al., "A comprehensive overview of emerging techniques and chemometrics for authenticity and traceability of animal-derived food," *Food Chem.*, vol. 402, p. 134 216, 2023.

[4] S. A. Wadood, G. Boli, Z. Xiaowen, I. Hussain, and W. Yimin, "Recent development in the application of analytical techniques for the traceability and authenticity of food of plant origin," *Microchem. J.*, vol. 152, p. 104 295, 2020.

[5] P. Jain, D. Gupta, H. Kaur, S. Singh, and K. K. Gaikwad, "Advanced anti-counterfeit inks in food packaging: A comprehensive review focusing on functional materials to digital integration," *Trends in Food Science & Technology*, p. 105 229, 2025.

[6] Y. Yang et al., "Exploring blockchain and artificial intelligence in intelligent packaging to combat food fraud: A comprehensive review," *Food Packaging and Shelf Life*, vol. 43, p. 101 287, 2024.

[7] J. Zuo et al., "Rfid-based sensing in smart packaging for food applications: A review," *Future Foods*, vol. 6, p. 100 198, 2022.

[8] A. R. Anwar, M. Mur, and M. Humar, "Microcavity-and microlaser-based optical barcoding: A review of encoding techniques and applications," *ACS photonics*, vol. 10, no. 5, pp. 1202–1224, 2023.

[9] L. Zhou, Y. Fan, R. Wang, X. Li, L. Fan, and F. Zhang, "High-capacity upconversion wavelength and lifetime binary encoding for multiplexed biodetection," *Angew. Chem. Int. Ed.*, vol. 130, no. 39, pp. 13 006–13 011, 2018.

[10] G. Lin, M. A. Baker, M. Hong, and D. Jin, "The quest for optical multiplexing in bio-discoveries," *Chem*, vol. 4, no. 5, pp. 997–1021, 2018.

[11] C. D. Keating and M. J. Natan, "Striped metal nanowires as building blocks and optical tags," *Adv. Mater.*, vol. 15, no. 5, pp. 451–454, 2003.

[12] Y. Zhang et al., "Multicolor barcoding in a single upconversion crystal," *J. Am. Chem. Soc.*, vol. 136, no. 13, pp. 4893–4896, 2014.

[13] J. Lee, P. W. Bisso, R. L. Srinivas, J. J. Kim, A. J. Swiston, and P. S. Doyle, "Universal process-inert encoding architecture for polymer microparticles," *Nat. Mater.*, vol. 13, no. 5, pp. 524–529, 2014.

[14] K. Braeckmans, S. C. De Smedt, C. Roelant, M. Leblans, R. Pauwels, and J. Demeester, "Encoding microcarriers by spatial selective photobleaching," *Nat. Mater.*, vol. 2, no. 3, pp. 169–173, 2003.

[15] C. Lin et al., "Submicrometre geometrically encoded fluorescent barcodes self-assembled from DNA," *Nat. Chem.*, vol. 4, no. 10, pp. 832–839, 2012.

[16] L. Wang, C. Yang, and W. Tan, "Dual-luminophore-doped silica nanoparticles for multiplexed signaling," *Nano Lett.*, vol. 5, no. 1, pp. 37–43, 2005.

[17] S. A. Dunbar, "Applications of luminex® xmap™ technology for rapid, high-throughput multiplexed nucleic acid detection," *Clin. Chim. Acta*, vol. 363, no. 1-2, pp. 71–82, 2006.

[18] X. Li et al., "Controlled fabrication of fluorescent barcode nanorods," *ACS Nano*, vol. 4, no. 8, pp. 4350–4360, 2010.

[19] Y. Li, Y. T. H. Cu, and D. Luo, "Multiplexed detection of pathogen DNA with DNA-based fluorescence nanobarcodes," *Nat. Biotechnol.*, vol. 23, no. 7, pp. 885–889, 2005.

[20] T. Maetzig, M. Morgan, and A. Schambach, "Fluorescent genetic barcoding for cellular multiplex analyses," *Exp. Hematol.*, vol. 67, pp. 10–17, 2018.

[21] T. A. Weissman and Y. A. Pan, "Brainbow: New resources and emerging biological applications for multicolor genetic labeling and analysis," *Genetics*, vol. 199, no. 2, pp. 293–306, 2015.

[22] A. V. Anzalone, M. Jimenez, and V. W. Cornish, *FRAME-tags: Genetically encoded fluorescent markers for multiplexed barcoding and time-resolved tracking of live cells*, April 09, 2021. bioRxiv, https://doi.org/10.1101/2021.04.09.436507 (accessed 2023-04-07).

[23] Y. Hou, Z. Gao, Y. S. Zhao, and Y. Yan, "Organic micro/nanoscale materials for photonic barcodes," *Org. Chem. Front.*, vol. 7, no. 18, pp. 2776–2788, 2020.

[24] Y. Tang, C. He, X. Zheng, X. Chen, and T. Gao, "Super-capacity information-carrying systems encoded with spontaneous raman scattering," *Chem. Sci.*, vol. 11, no. 11, pp. 3096–3103, 2020.

[25] F. Hu et al., "Supermultiplexed optical imaging and barcoding with engineered polyynes," *Nat. Methods*, vol. 15, no. 3, pp. 194–200, 2018.

[26] L. Shi et al., "Highly-multiplexed volumetric mapping with raman dye imaging and tissue clearing," *Nat. Biotechnol.*, vol. 40, no. 3, pp. 364–373, 2022.

[27] Y. Wang, B. Yan, and L. Chen, "SERS tags: Novel optical nanoprobes for bioanalysis," *Chem. Rev.*, vol. 113, no. 3, pp. 1391–1428, 2013.

[28] J. Chao et al., "Nanostructure-based surface-enhanced raman scattering biosensors for nucleic acids and proteins," *J. Mater. Chem. B*, vol. 4, no. 10, pp. 1757–1769, 2016.

[29] Z. Wang, S. Zong, L. Wu, D. Zhu, and Y. Cui, "Sers-activated platforms for immunoassay: Probes, encoding methods, and applications," *Chem. Rev.*, vol. 117, no. 12, pp. 7910–7963, 2017.

[30] J. Langer et al., "Present and future of surface-enhanced raman scattering," *ACS nano*, vol. 14, no. 1, pp. 28–117, 2019.

[31] Z. Wang et al., "SERS-fluorescence joint spectral encoding using organic–metal–QD hybrid nanoparticles with a huge encoding capacity for high-throughput biodetection: Putting theory into practice," *J. Am. Chem. Soc.*, vol. 134, no. 6, pp. 2993–3000, 2012.

[32] Y. Zhao et al., "Multifunctional photonic crystal barcodes from microfluidics," *NPG Asia Mater.*, vol. 4, no. 9, e25, 2012.

[33] X. Wei et al., "Multiplexed detection strategy for bladder cancer microRNAs based on photonic crystal barcodes," *Anal. Chem.*, vol. 92, no. 8, pp. 6121–6127, 2020.

[34] Y. Jo, J. Kwon, M. Kim, W. Choi, and M. Choi, "Microsphere-based interferometric optical probe," *Nat. Commun.*, vol. 9, no. 1, pp. 1–10, 2018.

[35] S. Shikha, T. Salafi, J. Cheng, and Y. Zhang, "Versatile design and synthesis of nano-barcodes," *Chem. Soc. Rev.*, vol. 46, no. 22, pp. 7054–7093, 2017.

[36] Y. Leng, K. Sun, X. Chen, and W. Li, "Suspension arrays based on nanoparticle-encoded microspheres for high-throughput multiplexed detection," *Chem. Soc. Rev.*, vol. 44, no. 15, pp. 5552–5595, 2015.

[37] P. H. Dannenberg, J. Wang, Y. Zhuo, S. Cho, K.-H. Kim, and S.-H. Yun, "Droplet microfluidic generation of a million optical microparticle barcodes," *Opt. Express*, vol. 29, no. 23, pp. 38 109–38 118, 2021.

[38] N. Martino et al., "Wavelength-encoded laser particles for massively multiplexed cell tagging," *Nature photonics*, vol. 13, no. 10, pp. 720–727, 2019.

[39] M. Humar and S. H. Yun, "Intracellular microlasers," *Nature photonics*, vol. 9, no. 9, p. 572, 2015.

[40] M. Schubert et al., "Lasing within live cells containing intracellular optical microresonators for barcode-type cell tagging and tracking," *Nano letters*, vol. 15, no. 8, pp. 5647–5652, 2015.

[41] M. T. Hill and M. C. Gather, "Advances in small lasers," *Nat. Photonics*, vol. 8, no. 12, pp. 908–918, 2014.

[42] L. He, Ş. K. Özdemir, J. Zhu, W. Kim, and L. Yang, "Detecting single viruses and nanoparticles using whispering gallery microlasers," *Nat. Nanotechnol.*, vol. 6, no. 7, pp. 428–432, 2011.

[43] D. Yu, M. Humar, K. Meserve, R. C. Bailey, S. N. Chormaic, and F. Vollmer, "Whispering-gallery-mode sensors for biological and physical sensing," *Nat Rev Methods Primers*, vol. 1, no. 1, p. 83, 2021.

[44] N. Toropov, G. Cabello, M. P. Serrano, R. R. Gutha, M. Rafti, and F. Vollmer, "Review of biosensing with whispering-gallery mode lasers," *Light Sci. Appl.*, vol. 10, no. 1, p. 42, 2021.

[45] Y. Wang, S. Zeng, G. Humbert, and H.-P. Ho, "Microfluidic whispering gallery mode optical sensors for biological applications," *Laser Photonics Rev.*, vol. 14, no. 12, p. 2 000 135, 2020.

[46] M. Schubert et al., "Monitoring contractility in cardiac tissue with cellular resolution using biointegrated microlasers," *Nat. Photonics*, vol. 14, no. 7, pp. 452–458, 2020.

[47] Q. Chen et al., "Self-assembled dna tetrahedral optofluidic lasers with precise and tunable gain control," *Lab on a Chip*, vol. 13, no. 17, pp. 3351–3354, 2013.

[48] S. Cho, M. Humar, and S.-H. Yun, "Laser-particle stimulated emission (lase) microscopy with super resolution," in *2016 Conference on Lasers and Electro-Optics (CLEO)*, IEEE, 2016, pp. 1–2.

[49] M. Schubert et al., "Lasing in live mitotic and non-phagocytic cells by efficient delivery of microresonators," *Sci. Rep.*, vol. 7, no. 1, pp. 1–9, 2017.

[50] Q. Chen, Y.-C. Chen, Z. Zhang, B. Wu, R. Coleman, and X. Fan, "An integrated microwell array platform for cell lasing analysis," *Lab on a Chip*, vol. 17, no. 16, pp. 2814–2820, 2017.

[51] Q. Song et al., "Random lasing in bone tissue," *Optics letters*, vol. 35, no. 9, pp. 1425–1427, 2010.

[52] Y.-C. Chen, Q. Chen, and X. Fan, "Lasing in blood," *Optica*, vol. 3, no. 8, pp. 809–815, 2016.

[53] M. C. Gather and S. H. Yun, "Single-cell biological lasers," *Nat. Photonics*, vol. 5, no. 7, pp. 406–410, 2011.

[54] A. Jonáš et al., "In vitro and in vivo biolasing of fluorescent proteins suspended in liquid microdroplet cavities," *Lab Chip*, vol. 14, no. 16, pp. 3093–3100, 2014.

[55] D. M. Chudakov, M. V. Matz, S. Lukyanov, and K. A. Lukyanov, "Fluorescent proteins and their applications in imaging living cells and tissues," *Physiological reviews*, vol. 90, no. 3, pp. 1103–1163, 2010.

[56] A. J. Kuehne and M. C. Gather, "Organic lasers: Recent developments on materials, device geometries, and fabrication techniques," *Chemical Reviews*, vol. 116, no. 21, pp. 12 823–12 864, 2016.

[57] S. Nizamoglu, M. C. Gather, and S. H. Yun, "All-biomaterial laser using vitamin and biopolymers," *Adv. Mater*, vol. 25, no. 41, pp. 5943–5947, 2013.

[58] X. Wu, Q. Chen, Y. Sun, and X. Fan, "Bio-inspired optofluidic lasers with luciferin," *Applied Physics Letters*, vol. 102, no. 20, 2013.

[59] T. Pan, D. Lu, H. Xin, and B. Li, "Biophotonic probes for bio-detection and imaging," *Light: Science & Applications*, vol. 10, no. 1, p. 124, 2021.

[60] M. Humar, A. Upadhya, and S. H. Yun, "Spectral reading of optical resonance-encoded cells in microfluidics," *Lab Chip*, vol. 17, no. 16, pp. 2777–2784, 2017.

[61] A. H. Fikouras et al., "Non-obstructive intracellular nanolasers," *Nat. Commun.*, vol. 9, no. 1, p. 4817, 2018.

[62] Z. Lv et al., "Intracellular near-infrared microlaser probes based on organic microsphere–SiO_2 core–shell structures for cell tagging and tracking," *ACS Appl. Mater. Interfaces*, vol. 10, no. 39, pp. 32 981–32 987, 2018.

[63] E. Fernandez-Rosas et al., "Intracellular polysilicon barcodes for cell tracking," *Small*, vol. 5, no. 21, pp. 2433–2439, 2009.

[64] S. E. Gratton et al., "The effect of particle design on cellular internalization pathways," *Proc. Natl. Acad. Sci. U.S.A*, vol. 105, no. 33, pp. 11 613–11 618, 2008.

[65] L. Y. Chen et al., "Mass fabrication and delivery of 3D multilayer μtags into living cells," *Sci. Rep.*, vol. 3, no. 1, pp. 1–6, 2013.

[66] O. González, R. L. Smith, and S. B. Goodman, "Effect of size, concentration, surface area, and volume of polymethylmethacrylate particles on human macrophages in vitro," *J. Biomed. Mater. Res.*, vol. 30, no. 4, pp. 463–473, 1996.

[67] E. Fernández-Rosas et al., "Internalization and cytotoxicity analysis of silicon-based microparticles in macrophages and embryos," *Biomed. Microdevices*, vol. 12, no. 3, pp. 371–379, 2010.

[68] R. Gómez-Martínez et al., "Intracellular silicon chips in living cells," *Small*, vol. 6, no. 4, pp. 499–502, 2010.

[69] K.-H. Kim, P. H. Dannenberg, H. Yan, S. Cho, and S.-H. Yun, "Compact quantum-dot microbeads with sub-nanometer emission linewidth," *Adv. Funct. Mater.*, vol. 31, no. 48, p. 2 103 413, 2021.

[70] S. J. Kwok et al., *Laser particle barcoding for multi-pass high-dimensional flow cytometry*, June 04, 2022. bioRxiv, https://doi.org/10.1101/2022.06.03.494697 (accessed 2023-04-07).

[71] P. H. Dannenberg et al., "Laser particle activated cell sorting in microfluidics," *Lab Chip*, vol. 22, no. 12, pp. 2343–2351, 2022.

[72] A. Kavčič et al., "Deep tissue localization and sensing using optical microcavity probes," *Nature Communications*, vol. 13, no. 1, p. 1269, 2022.

[73] X. Li et al., "In vivo tracking of individual stem cells labeled with nanowire lasers using multimodality imaging," *Biomed. Opt. Express*, vol. 13, no. 9, pp. 4706–4717, 2022.

[74] X. Li et al., "Optical coherence tomography and fluorescence microscopy dual-modality imaging for in vivo single-cell tracking with nanowire lasers," *Biomed. Opt. Express*, vol. 11, no. 7, pp. 3659–3672, 2020.

[75] Z. Gao et al., "Covert photonic barcodes based on light controlled acidichromism in organic dye doped whispering-gallery-mode microdisks," *Adv. Mater.*, vol. 29, no. 30, p. 1 701 558, 2017.

[76] Z. Gao, K. Wang, Y. Yan, J. Yao, and Y. S. Zhao, "Smart responsive organic microlasers with multiple emission states for high-security optical encryption," *Natl. Sci. Rev.*, vol. 8, no. 2, nwaa162, 2021.

[77] A. Capocefalo, E. Quintiero, C. Conti, N. Ghofraniha, and I. Viola, "Droplet lasers for smart photonic labels," *ACS Appl. Mater. Interfaces*, vol. 13, no. 43, pp. 51 485–51 494, 2021.

[78] M. Karl et al., "Flexible and ultra-lightweight polymer membrane lasers," *Nat. Commun.*, vol. 9, no. 1, p. 1525, 2018.

[79] D. Okada et al., "Optical microresonator arrays of fluorescence-switchable diarylethenes with unreplicable spectral fingerprints," *Mater. Horiz.*, vol. 7, no. 7, pp. 1801–1808, 2020.

[80] X. Zhan, Z. Zhou, W. Zhou, Y. Yan, J. Yao, and Y. S. Zhao, "Wavelength-tunable circularly polarized laser arrays for multidimensional information encryption," *Advanced Optical Materials*, vol. 11, no. 13, p. 2 200 872, 2023.

[81] K. Wang et al., "Geometry-programmable perovskite microlaser patterns for two-dimensional optical encryption," *Nano Lett.*, vol. 21, no. 16, pp. 6792–6799, 2021.

[82] Y. Ni et al., "Random lasing carbon dot fibers for multilevel anti-counterfeiting," *Nanoscale*, vol. 13, no. 40, pp. 16 872–16 878, 2021.

[83] A. Esidir et al., "Food-grade physically unclonable functions," *ACS Appl. Mater. Interfaces*, vol. 15, no. 35, pp. 41 373–41 384, 2023.

[84] J. W. Leem et al., "Edible matrix code with photogenic silk proteins," *ACS Cent. Sci.*, vol. 8, no. 5, pp. 513–526, 2022.

[85] Y.-W. Hu et al., "Flexible and biocompatible physical unclonable function anti-counterfeiting label," *Adv. Funct. Mater.*, vol. 31, no. 34, p. 2 102 108, 2021.

[86] J. Kim et al., "A water-soluble label for food products prevents packaging waste and counterfeiting," *Nat. Food*, pp. 1–8, 2024.

[87] J. W. Leem et al., "Edible unclonable functions," *Nat. Commun.*, vol. 11, no. 1, p. 328, 2020.

[88] H. Yousefi, H.-M. Su, S. M. Imani, K. Alkhaldi, C. D. M. Filipe, and T. F. Didar, "Intelligent food packaging: A review of smart sensing technologies for monitoring food quality," *ACS sensors*, vol. 4, no. 4, pp. 808–821, 2019.

[89] M. Weston, S. Geng, and R. Chandrawati, "Food sensors: Challenges and opportunities," *Advanced Materials Technologies*, vol. 6, no. 5, p. 2 001 242, 2021.

[90] I. Dudnyk, E.-R. Janeček, J. Vaucher-Joset, and F. Stellacci, "Edible sensors for meat and seafood freshness," *Sens. Actuators B: Chem.*, vol. 259, pp. 1108–1112, 2018.

[91] J. Siddiqui, M. Taheri, A. U. Alam, and M. J. Deen, "Nanomaterials in smart packaging applications: A review," *Small*, vol. 18, no. 1, p. 2 101 171, 2022.

[92] C. Rodrigues, V. G. L. Souza, I. Coelhoso, and A. L. Fernando, "Bio-based sensors for smart food packaging—current applications and future trends," *Sensors*, vol. 21, no. 6, p. 2148, 2021.

[93] M. K. Morsy et al., "Development and validation of a colorimetric sensor array for fish spoilage monitoring," *Food control*, vol. 60, pp. 346–352, 2016.

[94] H. Tao et al., "Silk-based conformal, adhesive, edible food sensors," *Adv. Mater.*, vol. 24, no. 8, pp. 1067–1072, 2012.

[95] A. S. Sharova, F. Melloni, G. Lanzani, C. J. Bettinger, and M. Caironi, "Edible electronics: The vision and the challenge," *Adv. Mater. Technol.*, vol. 6, no. 2, p. 2 000 757, 2021.

[96] G. M. Stojanović et al., "Temperature sensors manufactured from edible materials intended for oral cavity operation," *Int. J. Precis. Eng. Manuf. - Green Technol.*, vol. 11, no. 1, pp. 221–231, 2024.

[97] G. A. Salvatore et al., "Biodegradable and highly deformable temperature sensors for the internet of things," *Adv. Funct. Mater.*, vol. 27, no. 35, p. 1 702 390, 2017.

[98] Q. Chen, Y. Liu, K. Gu, J. Yao, Z. Shao, and X. Chen, "Silk-based electrochemical sensor for the detection of glucose in sweat," *Biomacromolecules*, vol. 23, no. 9, pp. 3928–3935, 2022.

[99] J. Kim, I. Jeerapan, B. Ciui, M. C. Hartel, A. Martin, and J. Wang, "Edible electrochemistry: Food materials based electrochemical sensors," *Adv. healthc. mater.*, vol. 6, no. 22, p. 1 700 770, 2017.

[100] I. K. Ilic, L. Lamanna, D. Cortecchia, P. Cataldi, A. Luzio, and M. Caironi, "Self-powered edible defrosting sensor," *ACS sensors*, vol. 7, no. 10, pp. 2995–3005, 2022.

[101] C. Vannahme, F. Maier-Flaig, U. Lemmer, and A. Kristensen, "Single-mode biological distributed feedback laser," *Lab Chip*, vol. 13, no. 14, pp. 2675–2678, 2013.

[102] Y. Choi, H. Jeon, and S. Kim, "A fully biocompatible single-mode distributed feedback laser," *Lab Chip*, vol. 15, no. 3, pp. 642–645, 2015.

[103] Y.-C. Chen, Q. Chen, and X. Fan, "Optofluidic chlorophyll lasers," *Lab Chip*, vol. 16, no. 12, pp. 2228–2235, 2016.

[104] W.-J. Lin et al., "All-marine based random lasers," *Org. Electron.*, vol. 62, pp. 209–215, 2018.

[105] T. Van Nguyen, H. H. Mai, T. Van Nguyen, D. C. Duong, et al., "Egg white based biological microlasers," *Journal of Physics D: Applied Physics*, vol. 53, no. 44, p. 445 104, 2020.

[106] D. Venkatakrishnarao, M. A. Mohiddon, and R. Chandrasekar, "The photonic side of curcumin: Microsphere resonators self-assembled from curcumin derivatives emitting visible/near-infrared light," *Adv. Opt. Mater.*, vol. 5, no. 2, p. 1 600 613, 2016.

[107] T. Van Nguyen et al., "Protein-based microsphere biolasers fabricated by dehydration," *Soft Matter*, vol. 15, no. 47, pp. 9721–9726, 2019.

[108] H. Mabuchi and A. Doherty, "Cavity quantum electrodynamics: Coherence in context," *Science*, vol. 298, no. 5597, pp. 1372–1377, 2002.

[109] V. Braginsky, M. Gorodetsky, and V. Ilchenko, "Quality-factor and nonlinear properties of optical whispering-gallery modes," *Physics letters A*, vol. 137, no. 7-8, pp. 393–397, 1989.

[110] Q.-F. Yang, X. Yi, K. Y. Yang, and K. Vahala, "Counter-propagating solitons in microresonators," *Nature Photonics*, vol. 11, no. 9, pp. 560–564, 2017.

[111] A. R. Anwar, M. Mur, G. Michailidou, D. N. Bikiaris, and M. Humar, "Microlasers made entirely from edible substances," *Advanced Optical Materials*, p. 2 500 497, 2025.

[112] A. Shitikov, I. Bilenko, N. Kondratiev, V. Lobanov, A. Markosyan, and M. Gorodetsky, "Billion q-factor in silicon wgm resonators," *Optica*, vol. 5, no. 12, pp. 1525–1528, 2018.

[113] D. Vernooy, V. S. Ilchenko, H. Mabuchi, E. Streed, and H. Kimble, "High-q measurements of fused-silica microspheres in the near infrared," *Optics letters*, vol. 23, no. 4, pp. 247–249, 1998.

[114] K. J. Vahala, "Optical microcavities," *nature*, vol. 424, no. 6950, pp. 839–846, 2003.

[115] M. L. Gorodetsky, A. A. Savchenkov, and V. S. Ilchenko, "Ultimate q of optical microsphere resonators," *Optics letters*, vol. 21, no. 7, pp. 453–455, 1996.

[116] C. Lam, P. T. Leung, and K. Young, "Explicit asymptotic formulas for the positions, widths, and strengths of resonances in mie scattering," *Journal of the Optical Society of America B*, vol. 9, no. 9, pp. 1585–1592, 1992.

[117] S. Schiller, "Asymptotic expansion of morphological resonance frequencies in mie scattering," *Applied optics*, vol. 32, no. 12, pp. 2181–2185, 1993.

[118] F. Vollmer, S. Arnold, and D. Keng, "Single virus detection from the reactive shift of a whispering-gallery mode," *Proceedings of the National Academy of Sciences*, vol. 105, no. 52, pp. 20 701–20 704, 2008.

[119] J. Zhu et al., "On-chip single nanoparticle detection and sizing by mode splitting in an ultrahigh-q microresonator," *Nature photonics*, vol. 4, no. 1, pp. 46–49, 2010.

[120] L. Shao et al., "Detection of single nanoparticles and lentiviruses using microcavity resonance broadening.," *Advanced materials (Deerfield Beach, Fla.)*, vol. 25, no. 39, pp. 5616–5620, 2013.

[121] J. Feng et al., "Random organic nanolaser arrays for cryptographic primitives," *Advanced Materials*, vol. 31, no. 36, p. 1 807 880, 2019.

[122] X. Wu et al., "Nanowire lasers as intracellular probes," *Nanoscale*, vol. 10, no. 20, pp. 9729–9735, 2018.

[123] D. Richter, M. Marinčič, and M. Humar, "Optical-resonance-assisted generation of super monodisperse microdroplets and microbeads with nanometer precision," *Lab on a Chip*, vol. 20, no. 4, pp. 734–740, 2020.

[124] P. Drössler, W. Holzer, A. Penzkofer, and P. Hegemann, "Ph dependence of the absorption and emission behaviour of riboflavin in aqueous solution," *Chemical Physics*, vol. 282, no. 3, pp. 429–439, 2002.

[125] L. Jinhua and Z. Guangyuan, "Polystyrene microbeads by dispersion polymerization: Effect of solvent on particle morphology," *International Journal of Polymer Science*, vol. 2014, no. 1, p. 703 205, 2014.

[126] Y. Gao, J. Zhang, J. Liang, D. Yuan, and W. Zhao, "Research progress of poly (methyl methacrylate) microspheres: Preparation, functionalization and application," *European Polymer Journal*, vol. 175, p. 111 379, 2022.

[127] E. P. on Food Additives et al., "Re-evaluation of silicon dioxide (E 551) as a food additive," *Efsa Journal*, vol. 16, no. 1, e05088, 2018.

[128] F. Vollmer and S. Arnold, "Whispering-gallery-mode biosensing: Label-free detection down to single molecules," *Nat. Methods*, vol. 5, no. 7, pp. 591–596, 2008.

[129] H. Lee and S. Michielsen, "Lotus effect: Superhydrophobicity," *J. Text. Inst.*, vol. 97, no. 5, pp. 455–462, 2006.

[130] C. Neinhuis and W. Barthlott, "Characterization and distribution of water-repellent, self-cleaning plant surfaces," *Annals of botany*, vol. 79, no. 6, pp. 667–677, 1997.

[131] W. Wang et al., "Superhydrophobic coatings with edible materials," *ACS Appl. Mater. Interfaces*, vol. 8, no. 29, pp. 18 664–18 668, 2016.

[132] Z. Korenjak and M. Humar, "Smectic and soap bubble optofluidic lasers," *Physical Review X*, vol. 14, no. 1, p. 011 002, 2024.

[133] A. R. Anwar, S. Kralj, and M. Humar, "Edible optical microcavities for optical barcoding, authentication, and sensing," *Scientific Reports*, 2026. DOI: 10.1038/s41598-026-51128-3.

[134] R. Waxier and G. Cleek, "Refractive indices of fused silica at low temperatures," *Journal of Research of the National Bureau of Standards. Section A, Physics and Chemistry*, vol. 75, no. 4, p. 279, 1971.

[135] J. D. Eversole et al., "High-precision identification of morphology-dependent resonances in optical processes in microdroplets," *JOSA B*, vol. 10, no. 10, pp. 1955–1968, 1993.

[136] N. A. Merabet, L. Cherbi, I. Haddouche, M. Benlacheheb, and J. Yu, "Glycosuria monitoring based on whispering gallery mode resonator biosensor," *Journal of Optics*, vol. 52, no. 3, pp. 1047–1055, 2023.

[137] G. Knothe and R. O. Dunn, "A comprehensive evaluation of the melting points of fatty acids and esters determined by differential scanning calorimetry," *J. Am. Oil Chem.' Soc.*, vol. 86, no. 9, pp. 843–856, 2009.

[138] J. Zhang, S. Liu, C. Xie, C. Wang, Y. Zhong, and K. Fan, "Recent advances in ph-sensitive indicator films based on natural colorants for smart monitoring of food freshness: A review," *Critical Reviews in Food Science and Nutrition*, vol. 64, no. 33, pp. 12 800–12 819, 2024.

[139] N. Bhattarai, J. Gunn, and M. Zhang, "Chitosan-based hydrogels for controlled, localized drug delivery," *Adv. Drug Deliv. Rev.*, vol. 62, no. 1, pp. 83–99, 2010.

[140] D. R. Rohindra, A. V. Nand, and J. R. Khurma, "Swelling properties of chitosan hydrogels," *South Pac J Nat Appl Sci*, vol. 22, no. 1, pp. 32–35, 2004.

[141] A. Poghossian, H. Geissler, and M. J. Schöning, "Rapid methods and sensors for milk quality monitoring and spoilage detection," *Biosens. Bioelectron.*, vol. 140, p. 111 272, 2019.

Bibliography

List of Publications Related to This Dissertation

Journal Articles

A. R. Anwar, M. Mur, and M. Humar, "Microcavity- and microlaser-based optical barcoding: A review of encoding techniques and applications," *ACS Photonics*, vol. 10, no. 5, pp. 1202–1224, 2023. DOI: 10.1021/acsphotonics.2c01611.

A. R. Anwar, M. Mur, G. Michailidou, D. N. Bikiaris, and M. Humar, "Microlasers made entirely from edible substances," *Advanced Optical Materials*, vol. 13, no. 22, p. 2 500 497, 2025. DOI: 10.1002/adom.202500497.

A. R. Anwar, S. Kralj, and M. Humar, "Edible optical microcavities for optical barcoding, authentication, and sensing," *Scientific Reports*, 2026. DOI: 10.1038/s41598-026-51128-3.

List of Patent Applications Related to This Dissertation

Matjaž Humar, Abdur Rehman Anwar, and Maruša Mur, *Edible microlasers, methods of their preparation and uses thereof* PCT/EP2024/057096.

Biography

Abdur Rehman Anwar received his Bachelor's degree in Physics from the Government College University in Faisalabad, Pakistan (2014-2018). He then completed his Master's degree in Applied Physics at the Ghulam Ishaq Khan Institute of Engineering Sciences and Technology, Pakistan (2018–2020), graduating with a Gold Medal for outstanding academic performance. His Master's research focused on III-nitride LEDs, with particular emphasis on efficiency enhancement through bandgap engineering.

In 2021, he began his PhD in Nanoscience and Nanotechnologies at the Jožef Stefan International Postgraduate School, Slovenia. His doctoral research focuses on the development of optical microcavities and microlasers, with an emphasis on fully edible barcodes and sensors for food tagging and tracing.

During his PhD, he gained international research experience as a Visiting Researcher at the University of St Andrews, United Kingdom (February to March 2025), where he worked on the development of distributed feedback (DFB) lasers based on edible materials. He also conducted research at the Aristotle University of Thessaloniki, Greece (November to December 2022), focusing on edible materials for sensing applications. Before his PhD, he worked as a Research Assistant at the Institute of High-Pressure Physics, Polish Academy of Sciences, Warsaw, Poland (November 2020 to March 2022), where he contributed to the optimization of III-nitride quantum well structures for topological insulator applications.

He has received several awards for his academic and research excellence, including Best Presentation Awards at the First LUCES Training School (RPTU Kaiserslautern-Landau, Germany, 2024), the 16th Jožef Stefan International Postgraduate School Students Conference (Slovenia, 2024), and the Summer School on Advanced Solutions in Food Production and Safety (CSIC-EEZA, Spain, 2023).

His research interests include the fabrication of whispering-gallery-mode (WGM) and Fabry–Pérot (FP) microcavities, development of edible photonic devices for sensing and barcoding, and modeling and simulation of optoelectronic devices.